

Electronic Thesis and Dissertation Repository

11-15-2018 2:30 PM

Empirical Characterization of Induced Seismicity in Alberta and Oklahoma

Mark Novakovic, *The University of Western Ontario*

Supervisor: Atkinson, Gail M., *The University of Western Ontario*

A thesis submitted in partial fulfillment of the requirements for the Doctor of Philosophy degree in Geophysics

© Mark Novakovic 2018

Follow this and additional works at: <https://ir.lib.uwo.ca/etd>



Part of the [Geophysics and Seismology Commons](#)

Recommended Citation

Novakovic, Mark, "Empirical Characterization of Induced Seismicity in Alberta and Oklahoma" (2018). *Electronic Thesis and Dissertation Repository*. 5961.
<https://ir.lib.uwo.ca/etd/5961>

This Dissertation/Thesis is brought to you for free and open access by Scholarship@Western. It has been accepted for inclusion in Electronic Thesis and Dissertation Repository by an authorized administrator of Scholarship@Western. For more information, please contact wlsadmin@uwo.ca.

Abstract

This thesis characterizes ground motions from induced seismic events in Alberta and Oklahoma, following an overall methodology that uses ground-motion recordings to calibrate the parameters of a seismological model. This body of work is carried out in three related studies.

In the first study, we perform a preliminary evaluation of ground motions in Alberta using thousands of observations of natural, induced and blast events of magnitude 1 to 4, recorded on a newly-deployed regional seismograph array. We evaluate the applicability of a moment magnitude (M) estimation algorithm for the events and compare the observed ground motions with expectations based on regional ground motion prediction equations (GMPEs). Ground motions for earthquakes are similar to those predicted by the small- M GMPE of Atkinson (2015), if one assumes that the predominant site condition in Alberta is a generic soft soil ($V_{s30} < 400$ m/s).

In the second study, ground motion observations from induced seismic events in Oklahoma are used to perform a generalized inversion to solve for regional source, attenuation and station site responses within the context of an equivalent point-source model following the method of Atkinson et al. (2015) and Yenier and Atkinson (2015b). The resolved parameters fully specify a regionally calibrated GMPE that can be used to describe median amplitudes from induced earthquakes in the central United States. Overall, the ground motions for soft rock (B/C) site conditions for induced events in Oklahoma are of similar amplitude to those predicted by the GMPEs of Yenier and Atkinson (2015b) and Atkinson et al. (2015) at close distances, for events of M 4 to 5. For larger events the Oklahoma motions are larger, especially at high frequencies. The Oklahoma motions follow a pronounced trilinear amplitude decay function at regional distances.

In the third study, we follow a similar procedure to develop a GMPE that fully specifies regional source, attenuation and station site responses for induced seismic events in Alberta. Ground motions in Alberta follow a pronounced trilinear amplitude decay function at regional distances. We account for observations of lower amplitude ground motions at high

frequencies in Alberta when compared to those observed in Oklahoma by adapting the near surface attenuation kappa effect (κ) model from Hassani and Atkinson (2018). Overall ground motions in Alberta are consistent with those expected for very shallow (depth < 10 km) natural events in central and eastern North America.

Keywords

Ground motion prediction equation, induced seismicity, moment magnitude, attenuation, stress parameter, engineering seismology.

Co-Authorship Statement

This integrated-article format thesis includes the following manuscripts written by Mark Novakovic and the co-authors. Mark is the first author on studies investigating the applicability of moment magnitude estimation algorithm for induced seismic events in Alberta, and the development of ground motion prediction equations for induced seismicity in Alberta and Oklahoma. Chapters 2, 3, and 4 have been previously published or submitted for publication to the peer reviewed journals *Seismological Research Letters* and the *Bulletin of the Seismological Society of America*. This thesis contains only the original results of research conducted by the candidate under the supervision of Dr. Gail M. Atkinson. Mark performed the analyses described in this thesis and authored these reports with assistance from Dr. Gail M. Atkinson. Ground motion data (Pseudo Spectral Accelerations and Peak Ground Motions) were computed and tabulated by Dr. Karen Assatourians. Continuous waveform data were provided from the Canadian Rockies and Alberta Network (CRANE) by Dr. Jeff Gu.

1) Novakovic M., Atkinson G. M. (2015). Preliminary Evaluation of Ground Motions from Earthquakes in Alberta. *Seismol. Res. Lett.*, 86(4): 1086-1095.

2) Novakovic M., Atkinson G. M., Assatourians K. (2018). Empirically Calibrated Ground-Motion Prediction Equation for Oklahoma. *Bull. Seismol. Soc. Am.* DOI: 10.1785/0120170331

3) Novakovic M., Atkinson G. M., Assatourians K., Gu Y. (2018). Empirically Calibrated Ground-Motion Prediction Equation for Alberta. *Bull. Seismol. Soc. Am.* DOI: (Submitted to the *Bulletin of the Seismological Society of America*, 31/08/2018)

The composed articles and thesis were completed under the supervision of Dr. Gail M. Atkinson.

Acknowledgements

To my supervisor Dr. Gail Marie Atkinson, I would like to express my sincerest gratitude for all of the guidance, support, patience, encouragement and opportunity you have provided throughout my time at Western. I have been incredibly fortunate to have had a mentor with such expansive knowledge and deep roots in the engineering seismology field and community, for which I will be eternally grateful.

I would like to thank Karen Assatourians for his friendship, support and tireless effort to provide high quality ground motion data sets for our analysis.

I would like to thank Justin Rubinstein, Thomas Pratt and our other anonymous paper reviewers for their constructive feedback which strengthened the manuscripts presented here.

I would like to thank my PhD committee members, Dr. Robert Scherbakov and Dr. Sheri Molnar; and my thesis examiners, Dr. Chris Cramer, Dr. Hadi Ghofrani, Dr. Katsu Goda, and Dr. Hesham El Naggar.

I would like to thank Behzad Hassani, Emrah Yenier, and Joseph Farrugia for our discussions of seismological principles and practices, which always concluded with a better understanding of the topic at hand.

I would like to kindly thank Andrew Reynen and Andrew Law from Nanometrics for providing earthquake meta-data tables for the TransAlta Network.

I would like to thank Tegan, Carson, Micah, Krista, Joanna, Sam, Azedeh, Sheri, Bernie, Arpit, Sebastian, Mingzhou, Freddie, Shaun, Sjors, Derek, Emma, Soushyant, Joelle, Sid, Surej, and the 3rd Rocks for your friendship and support.

I would like to thank my parents, Ray and Donna, for all they have done to help me get where I am today. I would like to thank my brothers Robi and Stefan for their love and support. Finally, I would like to thank Holly Mussell, my rock, for your unwavering love, support, encouragement and understanding throughout the completion of my studies.

Table of Contents

Abstract	i
Co-Authorship Statement.....	iii
Acknowledgements.....	iv
Table of Contents	v
List of Tables	viii
List of Figures	ix
List of Electronic Supplements.....	xvii
Chapter 1	1
1 Introduction	1
1.1 Organization of Thesis	1
1.2 Motivation.....	1
1.3 Response Spectra	3
1.4 Moment Magnitude Estimation	4
1.5 Ground Motion Prediction Equations	7
1.6 References.....	9
Chapter 2.....	15
2 Preliminary Evaluation of Ground Motions from Earthquakes in Alberta.....	15
2.1 Introduction.....	15
2.2 Magnitude Evaluations	18
2.3 Evaluation of Ground Motions	21
2.4 Conclusions.....	32
2.5 Acknowledgements.....	32
2.6 References.....	32
Chapter 3.....	35

3	Empirically Calibrated Ground Motion Prediction Equation for Oklahoma	35
3.1	Introduction.....	35
3.2	Database	36
3.3	Estimation of Moment Magnitude	39
3.4	Ground-Motion Model.....	41
3.5	Application to Induced Events in Oklahoma	47
3.6	Conclusions.....	63
3.7	Data and Resources.....	64
3.8	Acknowledgements.....	64
3.9	References.....	65
	Chapter 4.....	68
4	Empirically-Calibrated Ground Motion Prediction Equation for Alberta	68
4.1	Introduction.....	68
4.2	Database	69
4.3	Estimation of Moment Magnitude	72
4.4	Ground Motion Model	74
4.5	Application to Induced Events in Alberta.....	81
4.6	Conclusion	99
4.7	Data and Resources.....	100
4.8	Acknowledgements.....	100
4.9	References.....	100
	Chapter 5.....	105
5	Conclusions and Future Studies.....	105
5.1	Summary, Discussion and Conclusions.....	105
5.2	Recommendations for Future Studies.....	107
5.3	References.....	108

Appendices.....	110
Curriculum Vitae	115

List of Tables

Table 2.1: WNA anelastic attenuation and empirical calibration terms for 1.00 Hz and 3.33 Hz frequencies	19
Table A3.1: Tabulation of magnitude estimation model parameters. Where MC_F is the calibration factor for each frequency that aims to match the level that has been modified from Novakovic and Atkinson (2015) for Oklahoma. $\gamma_{F, low}$ (Eastern), $\gamma_{F, mod}$ (moderate), and $\gamma_{F, high}$ (Western) are the anelastic attenuation coefficients designed to remove distance dependent trends.....	110
Table A3.2: Summary table of stress parameter values from inversion for events of $M \geq 4.2$ in Oklahoma.....	110
Table A3.3: Summary of Oklahoma model coefficients and the anelastic attenuation function γ_{OK} , calibration factor C_{OK} , within event variability η , and in-between event variability ϵ as determined by the inversion.....	102
Table A4.1: Tabulation of magnitude estimation model parameters. MC_F is the magnitude calibration factor for each frequency. $\gamma_{F, low}$ (Eastern), $\gamma_{F, mod}$ (moderate), and $\gamma_{F, high}$ (Western) are the anelastic attenuation coefficients.....	113
Table A4.2: Summary of Alberta model coefficients, the anelastic attenuation function γ_{AB} , calibration factor C_{AB} , within event variability η , and in-between event variability ϵ as determined by the inversion.....	113
Table A4.3: Table of stress parameter values from inversion for all events in Alberta.....	114

List of Figures

Figure 1.1: Fourier displacement source spectrum where the solid line shows stress-drop values of 100 bars and dashed line show stress-drop values of 500 bars. Corner frequencies are shown as circles, and black vertical lines highlight the 1.00 Hz and 3.33 Hz frequencies. Reprinted from “Estimation of Moment Magnitude (M) for Small Events ($M < 4$) on Local Networks”, G. M. Atkinson (2014), *Seismological Research Letters*, 85(5): 1116-1124.....6

Figure 2.1: Map of stations and study events in Alberta. Events which are considered to be blasts are designated by an x. The deformation front that marks the boundary of the Rocky Mountains is distinguishable by topography. 16

Figure 2.2: Estimated M versus M_L (excluding events designated as blasts). Standard error of M estimates are also shown (horizontal bars, with verticals to denote edges)..... 20

Figure 2.3: Distribution of events (blasts excluded) in M and distance. 21

Figure 2.4: PSA amplitudes (all components) at 1.00 Hz for events of $M = 3.0 \pm 0.3$, as a function of hypocentral distance, compared to the relations of AGY14 (vertical component) and A15 (horizontal component, B/C conditions). 22

Figure 2.5: PSA amplitudes (all components) at 3.33 Hz for events of $M = 3.0 \pm 0.3$, as a function of hypocentral distance, compared to the relations of AGY14 (vertical component) and A15 (horizontal component, B/C conditions). 23

Figure 2.6: PSA residuals for $M \geq 2.6$ for PSA at 1.00 Hz (top), 3.33 Hz (middle) and 10.0 Hz (lower), for horizontal (left) and vertical (right) components (blasts removed). 25

Figure 2.7 Mean and standard error of PSA residuals for $M \geq 2.6$ at 1.00 Hz (top), 3.33 Hz (middle) and 10.0 Hz (lower), binned by log distance, for horizontal and vertical components (no error bar plotted if the number of observations in the bin is < 3). Slight offset from bin center used for plotting clarity (to distinguish horizontal from vertical). 26

Figure 2.8: Scaling of source terms with magnitude, in comparison to empirical (A15) and simulation-based (Yenier and Atkinson, 2015a) models 28

Figure 2.9: Average PSA residuals versus frequency in distance ranges 10-120 km, 120-250 km, 250-400 km (left=vertical, right=horizontal). Average including all distances is also shown (heavy line). Dashed line on right panel shows the average horizontal residual minus the average vertical residual, which is similar to an average site response function..... 29

Figure 2.10: Average station residuals for vertical and horizontal components of selected frequencies, for events with $M > 2.6$ (blasts excluded)..... 31

Figure 3.1: Study earthquakes (circles) and recording stations (light triangles). Stations chosen as B/C reference sites are highlighted (dark triangles). 37

Figure 3.2: The magnitude distance distribution of the database, containing 7278 records from 194 earthquakes (M 3.5 – 5.8) recorded at 101 seismograph stations. We consider records within logarithmically spaced bins with a cut-off distance that increases from 120 km for $M = 3.5$ to 500 km for $M \geq 4.0$ events. The moment magnitude values (M_{NA15}) are determined as described in Figure 3.3. 38

Figure 3.3: The logic tree used to decide which frequency is used to estimate moment magnitude (M) of the event. We compute M based on PSA at 0.30 Hz, 1.00 Hz and 3.33 Hz. The M estimate from 3.33 Hz PSA is used for events of $M < 3$, 1.00 Hz estimate for M 3 - 4, and 0.30 Hz for $M \geq 4$. For each event, the anelastic attenuation coefficient that minimizes the residuals is chosen, where three values are considered: low (CENA value), high (California value) or moderate (average of the two). 40

Figure 3.4: Comparison of M_{NA15} magnitude estimates with USGS/OGS reported M as obtained from regional or global moment tensors. Squares show average estimated M for events in 0.1 magnitude unit bins, along with standard deviation (dashed lines). Mean deviation from other estimates is about -0.1 units. 41

Figure 3.5: Observed normalized amplitudes (circles) after correction for magnitude dependence (F_M , Eqn 3.4) and CENA anelastic attenuation (Eqn 3.8); squares show median normalized amplitudes in distance bins. Solid lines show the adopted trilinear geometric spreading function (which has magnitude dependence as in YA15), for a range of magnitudes, assuming a 100-bar stress parameter; only the shape is important, as the level is

determined by inversion. A constant is added to all ground motions to adjust the level of the geometric spreading function for better visualization.. 45

Figure 3.6: Regional anelastic attenuation term for Oklahoma with standard deviation, in comparison to previous results of Yenier and Atkinson (2015b) for California and CENA.. 48

Figure 3.7: Site amplification (ln units) for the assigned reference B/C stations, resulting from the inversion OK005 sits on shale with V_{S30} of 613 m/s, OK029 sits on sandstone, while both OK030 and OK031 sit on shale. V_{S30} for OK029, OK030 and OK031 is believed to be close to B/C based on horizontal-to-vertical component ratios. 49

Figure 3.8: Typical site amplifications (ln units) for stations resulting from the inversion. WHAR is a sandstone station with V_{S30} of 1403 m/s. WMOK is a station sitting on granite with V_{S30} of 1859 m/s. OK009 is a station sitting on a conglomerate with V_{S30} of 322 m/s. No V_{S30} information is available for WLAR, OK032, KAN10 and HHAR; however according to surficial lithology maps, these stations sit on sandstone, alluvium, gravel and limestone respectively..... 50

Figure 3.9: All station terms. The lines depict the site response relative to B/C condition for all stations used in the study in natural log units. Squares depict the mean site term for each frequency, with their standard deviations in dashed lines.. 51

Figure 3.10: Determination of stress parameter, for M5.8 Pawnee event. Left) ΔLF (low-frequency offset) is determined as the offset of the average of observed spectral displacement (SD) on the seismic moment end of the spectrum (1.00 Hz) relative to predicted SD from YA15 (corrected for site and attenuation effects to a reference distance of 20 km). Right) ΔHF (high-frequency offset) is determined from the level of the 10.0 Hz PSA, after shifting spectrum by ΔLF . Note that the spectra in this figure have been converted from units of g to cm/s^2 52

Figure 3.11: Stress parameters for individual events (circles), compared with a with simple bilinear fit to the stress parameter versus magnitude (upper as a dashed line) and a simple fit to the stress parameter with respect to focal depth (lower as a solid line)..... 53

Figure 3.12: Stress parameters determined by inversion for each event (Figure 3.8) (circles) as a function of moment magnitude (M_{NA15}) and depth (larger circles denote greater depth). Solid lines show models that capture the observed trends in the Oklahoma data, in comparison to YA15 CENA model (dashed lines) for several values of focal depth. 54

Figure 3.13: Calibration factor (C_{OK}) obtained from inversion (squares) and its standard deviation (jagged lines). The solid line shows suggested model function for C_{OK} , the Yenier and Atkinson (2015b) calibration factor for CENA is shown as a dot-dashed line, and its modeled form is shown as a dashed line. 56

Figure 3.14: The Oklahoma calibration factor (gray line) and its inverse (black line), in comparison to the site amplification functions of Seyhan and Stewart (2014; SS14) for California, for a range of V_{S30} values (lines with symbols). It should be noted that the site amplification function is at a constant level for V_{S30} greater than 1500 m/s..... 58

Figure 3.15: Between-event residuals η , where dark (pink) circles show $M < 4$, light circles (green) show $M \geq 4$, and squares show the depth bin mean $\pm \sigma$59

Figure 3.16: Within event residuals with respect to the final GMPE for PSA at 1.01 Hz. Black squares depict the mean residual and its standard deviation in logarithmically spaced distance bins..... 60

Figure 3.17: Within event residuals with respect to the final GMPE for PSA at 5.12 Hz. Black squares depict the mean residual and its standard deviation in logarithmically spaced distance bins..... 61

Figure 3.18: : Within event residuals with respect to the final GMPE for PSA at 10.2 Hz. Black squares depict the mean residual and its standard deviation in logarithmically spaced distance bins..... 61

Figure 3.19: Within event residuals with respect to the final GMPE for PGA. Black squares depict the mean residual and its standard deviation in logarithmically spaced distance bins. 62

Figure 3.20: Final GMPE overlaying site corrected observations at 5.12 Hz. Lines depict the GMPE evaluated every 0.2 magnitude units from $M = 4.1$ to $M = 5.9$ at linearly-increasing

depths ranging from 3 to 8 km, respectively. Circles vary in diameter where larger circles represent larger magnitude observations and smaller circles denote smaller magnitude event observations. 62

Figure 3.21: GMPE for Oklahoma as determined in this study (solid lines) in comparison to the YA15 GMPE for CENA (dashed lines); both GMPEs are evaluated for focal depths of 5, 6 and 8 km for $M = 4, 5,$ and 6 respectively. The GMPE of Atkinson (2015), as determined from moderate California earthquakes with mean depth of 9 km, is also indicated (dotted lines), for distances < 50 km. All models are for NEHERP B/C reference site conditions... 63

Figure 4.1: Earthquakes (circles) and stations (inverted triangles) used in this study. Stations chosen as B/C reference sites are highlighted (diamonds). 69

Figure 4.2: The magnitude-distance distribution of the database, containing 884 records from 37 earthquakes ($M 3 - 4.3$) recorded at 75 seismograph stations. We consider records within logarithmically spaced bins with a cut-off distance that increases from 200 km for $M = 3$ to 600 km for $M \geq 4$ events. The moment magnitude values (M) are determined as described in Figure 4.3..... 70

Figure 4.3: A logic tree to decide which frequency is used to estimate moment magnitude (M) of the event. We compute M based on PSA at 1.00 Hz and 3.33 Hz. The M estimate from 3.33 Hz PSA is used for events of $M < 3$, 1.00 Hz estimate for $M \geq 3$, and the mean of the two values for $M \sim 3$. For each event, the anelastic attenuation coefficient that minimizes the residuals is chosen, where three values are considered: low (CENA value), high (California value) or moderate (average of the two). 73

Figure 4.4: Comparison of moment magnitude estimates based on PSA with the local magnitudes as reported by the Alberta Geological Survey. The two scales agree quite well for $M > 2.6$; ground motion response amplitudes scale weakly with ML at lower magnitudes. 74

Figure 4.5: Observed normalized amplitudes (circles) after correction for magnitude dependence (FM, Eqn 4.4), Oklahoma stress parameter model and anelastic attenuation (Eqn 4.5 & 4.13); squares show median normalized amplitudes in distance bins. Solid lines show the adopted trilinear geometric spreading function (which has magnitude dependence as in

YA15), for a range of magnitudes, assuming a 100-bar stress parameter; only the shape is important, as the level is determined by inversion. A constant is added to all ground motions to adjust the level of the geometric spreading function for better visualization. Large scatter at near distances reflects variability in source amplitudes.....**Error! Bookmark not defined.**

Figure 4.6: Regional anelastic attenuation function obtained from the inversion (Alberta) in comparison to previous results of Novakovic et al. (2018) for Oklahoma, Yenier and Atkinson (2015b) for California and Central and Eastern North America. 82

Figure 4.7: Site amplification (ln units) for the assigned reference B/C stations as obtained from the inversion. The average over the five reference stations is 0 ln units by definition. The selected reference stations are all post-hole seismometers that provide well behaved horizontal-to-vertical component ratios and B/C like responses. 83

Figure 4.8: Typical site amplification (ln units) for stations resulting from the inversion. Pronounced peaked amplification is observed at many stations suggesting that site conditions are on average softer across the province than those chosen as B/C-like reference stations.. 84

Figure 4.9: All station terms. The lines depict the site response relative to B/C condition for all stations used in the study in natural log units. Squares depict the mean site term for each frequency with their standard deviation in dashed lines. 84

Figure 4.10: (Left) stress parameters determined by inversion for each event as a function of M (triangles). Solid lines show the stress parameter model for Oklahoma evaluated over a range of depths. Lines with symbols depict YA15 stress parameter models for CENA over a range of depths. (Right) Composition of stress parameter computations in this study with suspected induced events in Oklahoma from other studies.. 87

Figure 4.11: (Left) the dashed line shows the event source term; thin solid lines show the evaluated source term for linearly spaced κ values and best fit stress parameter value pair; thick solid line depicts best spectral matched κ for an events modeled stress parameter value. (Right) shows goodness of κ - $\Delta\sigma$ pair fits in the 90th, 95th and 97.5th percentiles. 89

Figure 4.12: (Left) the dashed line shows the event source term; thin solid lines show the evaluated source term for linearly spaced κ values and best fit stress parameter value pair;

thick solid line depicts best spectral matched κ for an events modeled stress parameter value.
 (Right) shows goodness of κ - $\Delta\sigma$ pair fits in the 90th, 95th and 97.5th percentiles..... 90

Figure 4.13: (Left) the dashed line shows the event source term; thin solid lines show the evaluated source term for linearly spaced κ values and best fit stress parameter value pair; thick solid line depicts best spectral matched κ for an events modeled stress parameter value.
 (Right) shows goodness of κ - $\Delta\sigma$ pair fits in the 90th, 95th and 97.5th percentiles. 90

Figure 4.14: Kappa value that minimizes the residuals between the observed event term and predicted source term when the stress parameter is assigned based on Eqn (4.16). 91

Figure 4.15: Calibration factor (C_{AB}) obtained from inversion (squares) and its standard deviation (error bars). Heavy line shows suggested model function for C_{AB} . Corresponding calibration factors for other regions are shown for comparison (lines with symbols; circles=Oklahoma; triangle=CENA; diamond=California)..... 93

Figure 4.16: The Alberta calibration factor (light line) and its inverse (black line), in comparison to the site amplification functions of Seyhan and Stewart (2014; SS14) for California, for a range of V_{S30} values (lines with symbols)..... 94

Figure 4.17: Within event residuals with respect to the final GMPE for PSA at 1.01 Hz. Black squares and error bars depict the mean residual and its standard deviation in logarithmically spaced distance bins 95

Figure 4.18: Within event residuals with respect to the final GMPE for PSA at 10.17 Hz. Black squares and error bars depict the mean residual and its standard deviation in logarithmically spaced distance bins. 96

Figure 4.19: Between-event residuals as a function of moment magnitude at 0.5 Hz, 1.0 Hz, 5.1 Hz and 10.2 Hz. 96

Figure 4.20: Between-event residuals as a function of stress parameter (bar) at 0.5 Hz, 1.00 Hz, 5.0 Hz and 10.0 Hz..... 97

Figure 4.21: 20 Final GMPE overlaying site corrected observations at 1.0 Hz. Lines depict the GMPE evaluated every 0.2 magnitude units from $M = 2.9$ to $M = 4.5$. Circles vary in

diameter where larger circles represent higher magnitude observations and smaller circles denote lower magnitude event observations..... 98

Figure 4.22: . The GMPE for Alberta as determined in this study (solid lines) in comparison to the NAA18 GMPE for Oklahoma (circles) is evaluated at the typical focal depth for events in Oklahoma of 5 km. YA15 GMPE for CENA (dashed lines) is evaluated for focal depths of 6 and 8 km for **M4** and **M6** respectively. The GMPE of Atkinson (2015), as determined from moderate California earthquakes with mean depth of 9 km, is also indicated (dotted lines), for distances < 50 km. All models are for NEHRP B/C reference site conditions..... **Error! Bookmark not defined.**

List of Electronic Supplements

Table S3.1: Site Amplification Functions. Site amplification functions for all stations used in the Oklahoma study. Records are relative to the B/C site condition and are reported in natural logarithmic units.

Table S3.2: Event Specific Information and Stress Parameter. Event by event determined stress parameter, magnitude M , date, time, location and reported depth (km).

Table S3.3: Model Parameters. Coefficients at 30 logarithmically spaced frequencies, PGA and PGV for all models used in the study as well as inversion resulting anelastic attenuation coefficient (γ_{OK}), regional calibration factor for Oklahoma (C_{OK}), within event variability (η), and inter event variability (ϵ).

Table S4.1: Model Parameters. Coefficients at 30 logarithmically spaced frequencies, PGA and PGV for all models used in the study as well as inversion resulting anelastic attenuation coefficient (γ_{OK}), regional calibration factor for Oklahoma (C_{OK}), within event variability (η), and inter event variability (ϵ). This table includes an evaluated form of the GMPE for Alberta derived in this paper, as well as the Novakovic et al. Oklahoma GMPE (2018).

Table S4.2: Site Amplification Functions. Site amplification functions for all stations used in the Alberta study. Records are relative to the B/C site condition and are reported in natural logarithmic units.

Chapter 1

1 Introduction

1.1 Organization of Thesis

This thesis is presented in 5 chapters. Chapter 1 introduces the motivation of the study as well as background materials relevant to response spectra, the estimation of moment magnitude from commonly used ground motion parameters and ground motion prediction equations. Chapter 2 presents an adopted moment magnitude estimation equation (Atkinson et al., 2014) and its applicability to induced seismic events in Alberta. In Chapter 3, a regionally adjustable ground motion prediction equation framework (Yenier and Atkinson, 2015b) is empirically calibrated for use with induced seismic events in Oklahoma. Chapter 4 explores the empirical calibration of the regionally adjustable ground motion prediction equation (Yenier and Atkinson, 2015b) for induced seismicity observed in Alberta as well as the adaptation of a near surface attenuation correction term (Hassani and Atkinson, 2018) that accounts for region specific differences between observed ground motions and simulations. Chapter 5 contains a summary, concluding remarks, and recommendations for future studies.

1.2 Motivation

Induced seismic activity attributed to hydraulic fracturing and waste water injection operations has become more prevalent over the last decade (Ellsworth, 2013; Keranen et al., 2014; Schultz et al., 2015; Atkinson et al., 2016; Petersen et al., 2016). A pressing issue is the potential hazard to infrastructure due to ground motions from induced earthquakes (Atkinson, 2017). Thus, it is important to characterize ground motions from such events. Recent monitoring programs launched by Universities (Western University, University of Alberta, and University of Calgary, in partnership with Nanometrics, Inc.), and by the Alberta Geological Survey, as well as the Geological Survey of Canada (with GeoScience British Columbia) have resulted in densification of the seismographic network, and improved the availability of ground-motion datasets for induced events in the Western Canada Sedimentary Basin (WCSB, in western Alberta and eastern B.C.).

Nevertheless, the ground-motion data in the WCSB is sparse in comparison to those available in other regions, such as California and Oklahoma. Therefore, we can extend our understanding of motions in the WCSB by comparing them to those in more data-rich regions. Understanding of ground motions is fundamental to hazard assessment.

Seismic hazard for ordinary structures is considered in provisions of the National Building Code of Canada (NBCC). Generally, seismic hazard is evaluated using a probabilistic approach for engineering design practice such that structures are designed to withstand potential ground shaking that could occur (Cornell, 1968; McGuire, 1977; Basham et al., 1982, 1985). Seismic hazard analysis is composed of four main components: definition of seismic source zones, magnitude-recurrence relationships for each source, selection of ground motion prediction equations (GMPE), and the computation of ground shaking intensity versus probability of exceedance (the hazard curve). Seismic source zones are defined by grouping associated seismicity which is in close proximity to a known fault system or simply by a geographic area. Magnitude-recurrence relationships express by the frequency of occurrence versus the magnitude as developed by the Gutenberg and Richter (1944) recurrence law. Applicable ground motion prediction equations are selected to define each event type in each source zone, typically expressed as a suite of weighted GMPEs. The hazard contributions are integrated over all distances and magnitudes for all source zones according to the total probability theorem (Adams and Atkinson, 2003). The probability of exceeding a specified intensity of ground shaking, at various frequencies over a given period of time expresses the hazard. The reliability of the input GMPEs to specify the expected median or peak ground motion amplitude as a function of distance, magnitude and other variables, as well as the rate of occurrence of events, are particularly important to the reliability of the final hazard model (Adams and Atkinson, 2003; Atkinson and Adams 2013).

The NBCC is periodically updated with regional seismic hazard maps that reflect evolving seismic hazard models. Currently the NBCC national seismic hazard maps do not consider the contributions of induced seismicity to hazard. In the United States induced seismicity is not considered directly in the hazard maps either, however, yearly

seismic hazard forecasts for the Central and Eastern United States were generated by Petersen et al. (2016, 2017, and 2018). Areas located within the stable craton that are distant from zones with tectonically-active structures are generally associated with relatively low hazard. An issue arises when regions with historically low seismicity rates and low probabilities of exceeding damaging ground motions become exposed to induced seismicity.

Introducing induced seismicity to previously low-rate seismic zones may completely change the hazard assessment of the region. This becomes increasingly important as operations are conducted in close proximity to critical infrastructure. Mitigation strategies, such as traffic light protocols, have been introduced to reduce the probability of increased exposure to strong ground motions after an initial induced event occurs (e.g. UKOOG, 2013). Such protocols may provide procedures for shut-down and flow back of hydraulic fracture treatments based on the magnitude and location of an induced event, and the ground motion level (e.g. AER, 2015, BCOGC, 2017). The rapid and reliable determination of local (M_L) and moment magnitude (M) after a seismic event occurs is important for operators of wells and nearby critical infrastructure, in order to initiate response plans and mitigation strategies to reduce the exposure and impact of an induced event. M_L is a common scale used in catalogs because it is relatively simple to compute, whilst M is the measure preferred for many seismological applications because it is a better measure of earthquake size and energy release (Hanks and Kanamori, 1982). The results of this thesis aim to improve our knowledge of ground-motion effects of induced seismic events, reduce their impact on surrounding stakeholders, and help facilitate the inclusion of such hazards into future building code editions.

1.3 Response Spectra

Ground shaking should be specified in a format that is relevant for engineered structures. Building design is based on a spectrum that specifies the level of displacement (or seismic design force) as a function of the natural period of vibration of that structure with some level of damping (Consortium of Universities for Research in Earthquake Engineering (CUREE), 1997); the spectrum is specified for a target probability of exceedance, typically 2% in 50 years for building-code applications. It is useful to

represent peak values of seismic response (displacement, velocity, or acceleration) of a single degree of freedom system, versus the natural period of vibration, for a given viscous critical damping ratio of 5% (Trifunac, 1971). Earthquake input ground-motions may then be modelled as a response spectrum which specifies the maximum or median shaking response of several oscillators with varying natural frequencies; a common response spectral measure is the pseudo-spectral accelerations (PSA) with 5% damping. By the superposition of different modes of response, spectrum techniques can be applied to the design and analysis of complex structures such as buildings or dams. Response spectra were first introduced by Biot (1941) and Housner (1941), using a direct mechanical analog, and later by Housner and McCann (1949) using electric analog techniques. The growing number of strong-motion instrumentation in seismically active regions of the world facilitated the need for a rapid and automated spectrum calculation procedures. Nigam and Jennings (1969) introduced a numerical method for the calculation of response spectra from strong-motion earthquake accelerograms. The methodology to calculate spectra is based on obtaining the exact solution to the governing differential equation for the successive linear segments of the excitation, then using this solution to compute the response at discrete time intervals in a purely arithmetical way (Hudson, 1962; Iwan, 1960). To construct the response spectra, one calculates the displacement for that period. The pseudo-velocity and pseudo-acceleration values are determined by multiplying the spectral displacement by the factor of ω or ω^2 , respectively, where ω is the angular frequency. For earthquake design, the horizontal component is generally of most interest as it is more damaging because structures have a greater inherent capacity to resist vertical loads.

1.4 Moment Magnitude Estimation

For moderate to large events ($M > 4.5$), M is routinely obtained by exercising standard seismological methods (e.g. seismic moment tensor solutions) with regional or global data. The robust determination of M for small events using conventional techniques is particularly challenging however, as the signal may only be recorded above the noise floor at close distances. This becomes an important problem when developing magnitude-recurrence relations for regions that merge small-event and large-event

seismicity catalogs together. This is also important for induced seismicity applications in which a reliable assessment of moment magnitude is necessary for traffic light protocols and triggering of mitigation strategies in response to events that may exceed damaging ground-motion thresholds. Reliable estimation of \mathbf{M} for moderate events in North America (\mathbf{M} 3-5) was developed by Atkinson and Babaie Mahani (2013), utilizing regional recordings of PSA at 1.00 Hz, a standard ShakeMap parameter that is commonly used in engineering seismology (Wald et al., 1999). This ground-motion parameter closely correlates with seismic moment and allows for a regional calibration of \mathbf{M} using moderate events with known moment magnitudes. Due to the lack of events with known moment for $\mathbf{M} < 3$, and an insufficient signal to noise ratio at 1.00 Hz at regional distances, this technique is not directly useful for induced-seismicity applications.

Atkinson et al. (2014) tackled the problem by developing a method of estimating \mathbf{M} from PSA at 1.00 Hz or 3.33 Hz from local network data that focuses on short-to-regional distances, utilizing a stochastic point-source model to provide a physically-based scaling of the relationship down to small magnitudes. The source spectrum in this model is represented by a Brune model of the shear radiation.

The Brune (1970, 1971) model represents the spectral shape of earthquake ground motions at the source, which scales with the corner frequency and seismic moment expressed as

$$\Omega(\omega) = \frac{M_o}{1 + \left(\frac{\omega}{\omega_o}\right)^2} \quad (1.1)$$

where Ω is the Fourier displacement spectrum amplitude, M_o is the seismic moment, ω is the angular frequency, and ω_o is the angular corner frequency (Madariaga, 2006). The flat low-frequency end of a standard Brune (1970, 1971) model displacement spectrum, in which the amplitude is directly proportional to seismic moment, will scale practically independently of stress drop. PSA at 1.00 Hz and PSA at 3.33 Hz fall on the low-frequency end of the spectrum over a wide range of stress-drop values for sufficiently-small events ($\mathbf{M} < 3$) and are less susceptible to noise contamination at these magnitudes

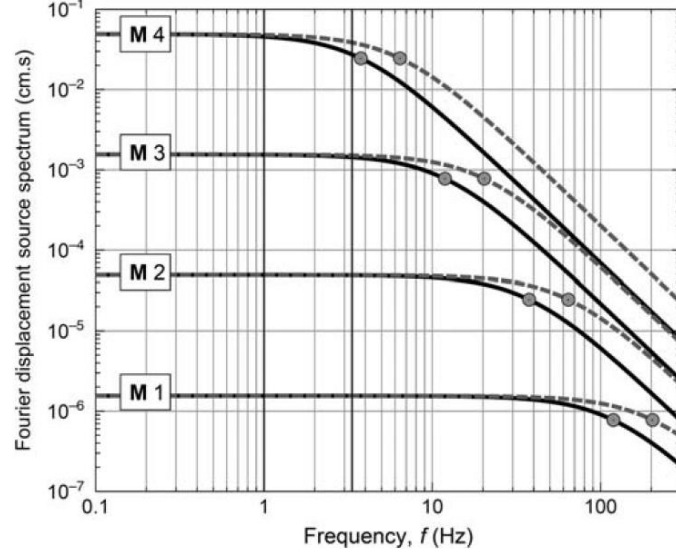


Figure 1.1: Fourier displacement source spectrum where the solid line shows stress-drop values of 100 bars and dashed line show stress-drop values of 500 bars. Corner frequencies are shown as circles, and black vertical lines highlight the 1.00 Hz and 3.33 Hz frequencies. Reprinted from “Estimation of Moment Magnitude (M) for Small Events ($M < 4$) on Local Networks”, Atkinson et al. (2014), *Seismological Research Letters*, 85(5): 1116-1124.

than PSA at 1.00 Hz. Figure 1.1 shows source spectrum evaluated at 100 bars and 500 bars at $R_{Hypo} = 1$ km for M 1, 2, 3 and 4 (Atkinson et al., 2014) to demonstrate the frequency selection that represents the moment end of the spectrum for small magnitude events. By simulating time series for events of M 0-4 using the stochastic point-source algorithm Stochastic-Method SIM-ulation (SMSIM; Boore, 2000), the authors ensure that the equation will scale correctly to small magnitudes. Finally, seismologically informed regressions produce a relationship between hypocentral distance (R_{hypo}), moment magnitude (M) and the vertically oriented PSA at 1.00 Hz and 3.33 Hz as equation (1.2):

$$M = \frac{\log_{10} PSA_F - MC_F + \log_{10} Z(R) + \gamma_F R_{Hypo}}{1.45} \quad (1.2)$$

where PSA_F is the vertical channel PSA at frequency F , MC_F is the magnitude calibration factor, $Z(R)$ is the geometric spreading term and γ_F is an anelastic attenuation term. The vertical component is selected because in general the PSA will be similar to an unamplified horizontal-component PSA which will minimize the influence of site

response and is applicable to a range of sites (Lermo and Chavez Garcia 1993; Siddiqi and Atkinson, 2002; Atkinson and Boore, 2006). The formulation of this model is particularly useful as its derivation method is transparent, robust, and based on simple and well-known seismological scaling principles. As more detailed empirical information on the overall amplitude level and attenuation is acquired, the model can be refined on a regional basis. The method produced unbiased estimates of moment magnitudes in both Eastern and Western North America for records within 120 km for $M \leq 2.6$, 300 km for $2.6 < M \leq 4.0$, and up to 500 km for $M > 4.0$.

1.5 Ground Motion Prediction Equations

Observed ground motion attributes are often expressed for hazard assessment and ShakeMap applications using empirical ground-motion prediction equations (GMPEs). In data-rich regions (e.g. Western North America, WNA) these can be directly derived using regression techniques (e.g., NGA-WEST, Boore and Atkinson 2008, Boore et al., 2013). Deriving a GMPE in data-poor regions can be achieved using several approaches. Based on a seismological model, a GMPE may be developed by generating synthetic ground motions over a wide magnitude and distance range. The seismological model describes the source, path and site effects and relies upon available empirical data in the region to calibrate model parameters.

The stochastic method is a simple and powerful method for simulating ground motions. The widely adopted method is based on the work of Hanks and McGuire who combined the notion that high-frequency motions are basically random with seismological models of the spectral amplitude of ground motion (Hanks, 1979, McGuire and Hanks, 1980, Hanks and McGuire, 1981). It is assumed that ground motions can be expressed as band-limited, finite-duration, Gaussian noise. The source spectra is described by a single corner-frequency model whose corner frequency depends on the earthquake size according to the Brune (1970, 1971) model; the source spectrum is attenuated with distance based on an empirical function. Their work has been generalized to allow for arbitrarily complex models, the extension to the simulation of time series and the consideration of many measures of ground motions (Boore, 1983). Commonly, parametric or functional descriptions of the ground motion's amplitude spectrum are

combined with a random phase spectrum that is modified such that the motion is distributed over a duration related to the earthquake magnitude and to the distance from the source (Boore 2003). Simple stochastic point-source methods or more sophisticated finite-source broadband techniques may be used to perform simulations (e.g., Atkinson and Boore, 1995, 2006; Silva et al., 2002; Somerville et al., 2001, 2009; Frankel, 2009; Toro et al., 1997).

The hybrid empirical method is another common approach to deriving GMPEs (Campbell, 2002, 2003). Data-rich host regions are used to calibrate an empirically well constrained GMPE by determining adjustment factors obtained from response-spectral ratios of stochastic simulations in the host and target regions (e.g., Campbell, 2002, 2003; Scherbaum et al., 2005; Pezeshk et al., 2011). Atkinson (2008) describes a referenced empirical approach. This method is similar to the hybrid empirical method; however, adjustment factors are determined empirically using ratios of observed ground motions in the target region to predictions of an empirical GMPE in the host region (e.g., Atkinson, 2008, 2010; Atkinson and Boore, 2011; Atkinson and Motazedian, 2013; Hassani and Atkinson, 2015). Key concepts from both the hybrid empirical and referenced empirical approaches are utilized of by Yenier and Atkinson (2015a) to develop a robust simulation-based generic GMPE. The overarching philosophy behind the generic GMPE methodology is that the magnitude-scaling terms are fixed by previous detailed simulation studies, while a select few parameters, specifically the anelastic attenuation and calibration constant, are fine-tuned for the region of interest. Calibration of a well-behaved and validated generic model for a specific region of interest can be achieved using limited amplitude and attenuation data. The source, path, and site models in the generic GMPE framework are decoupled allowing for flexibility and adjustments when necessary to capture the characteristics of ground motions in a region.

First a well-calibrated simulation based GMPE for active tectonic regions using the NGA-West2 database (Ancheta et al., 2014) is developed. Basic source and attenuation parameter effects, including magnitude, distance, stress parameter, geometrical spreading rates and anelastic attenuation coefficients on peak ground motions and response spectra are isolated and parameterized. Minimal regional data are then required to calibrate the

predictive model. An empirical calibration factor that accounts for residual effects that are missing in simulations when compared to empirical data is also considered. Atkinson et al. (2015) describe the adjustment approach of this generic GMPE to the Southern Ontario Seismic Network. Chapters 3 and 4 describe the approach in detail and we apply this method to ground motion observations from Oklahoma and Alberta respectively.

1.6 References

- Adams, J., and Atkinson, G. M. (2003). Development of seismic hazard maps for the proposed 2005 edition of the National Building Code of Canada, *Canadian Journal of Civil Engineering*, 30, 255-271.
- Alberta Energy Regulator (2015). Subsurface Order No. 2, <https://aer.ca/documents/orders/subsurface-orders/SO2.pdf> (last accessed August 22, 2018).
- Ancheta, T., Darragh, R., Stewart, J., Seyhan, E., Silva, W., Chiou, B., Wooddel, K., Graves, R., Kottke, A., Boore, D., et al. (2014). PEER NGAWest2 Database, *Earthquake Spectra* 30, 989-1006.
- Atkinson, G. M. (2008). Ground motion prediction equations for Eastern North America from a referenced empirical approach: Implications for epistemic uncertainty. *Bull. Seismol. Soc. Am.* 98, 1304-1318.
- Atkinson, G. M. (2010). Ground-motion prediction equations for Hawaii from a referenced empirical approach. *Bull. Seismol. Soc. Am.* 100 (2), 751-761.
- Atkinson, G. M. (2015). Ground-motion prediction equation for small to-moderate events at short hypocentral distances, with application to induced seismicity hazards, *Bull. Seismol. Soc. Am.* 105, 2A, doi: 10.1785/0120140142
- Atkinson, G. M. (2017). Strategies to prevent damage to critical infrastructure from induced seismicity. FACETS, Science Application Forum, doi: 10.1139/facets-2017-0013
- Atkinson, G. M., and Adams, J. (2013). Ground motion prediction equations for application to the 2015 Canadian national seismic hazard maps, *Canadian Journal of Civil Engineering*, 40, 988-998.
- Atkinson, G. M., and Boore, D. M. (1995). Ground-motion relations for eastern North America. *Bull. Seismol. Soc. Am.* 85, 17-30.
- Atkinson, G. M., and Boore, D. M. (2006). Ground motion prediction equations for earthquakes in Eastern North America. *Bull. Seismol. Soc. Am.* 103, 107-116.

- Atkinson, G. M., and Boore, D. M. (2011). Modifications to existing ground-motion prediction equations in light of new data. *Bull. Seismol. Soc. Am.*, 101: 1121-1135.
- Atkinson, G., Eaton, D., Ghofrani, H., Walker, D., Cheadle, B., Schultz, R., Shcherbakov, R., Tiampo, K., Gu, J., Harrington, R., Liu, Y., van der Baan, M., and Kao, H. (2016). Hydraulic fracturing and seismicity in the Western Canada Sedimentary Basin, *Seismological Research Letters* 87, no. 3, doi: 10.1785/0220150263.
- Atkinson, G. M., Greig, W., and Yenier, E. (2014). Estimation of Moment Magnitude (M) for Small Events ($M < 4$) on Local Networks. *Seismological Research Letters*, 85 (5): 1116-1124.
- Atkinson, G. M., Hassani, B., Singh, A., Yenier, E., Assatourians, K. (2015). Estimation of Moment Magnitude and Stress Parameter from ShakeMap Ground-Motion Parameters. *Bull. Seismol. Soc. Am.* DOI: 10.1785/0120150119.
- Atkinson, G. M. and Mahani A. B. (2013). Estimation of moment magnitude from ground motions at regional distances. *Bull. Seismol. Soc. Am.* 103, 2604–2620.
- Atkinson, G. M., and Motazedian, D. (2013). Ground-motion amplitudes for earthquakes in Puerto Rico. *Bull. Seismol. Soc. Am.* 103, 1846-1859.
- Basham, P., Weichert, D., Anglin, F., and Berry, M. (1982). New probabilistic strong seismic ground motion maps of Canada – a compilation of earthquake source zones, methods and results, Energy, Mines and Resources Canada, Earth Physics Branch, Open-file Report 82-33.
- BC Oil and Gas Commission (BCOGC). (2017). Guidance for Ground Motion Monitoring and Submission, <https://www.bco.gc.ca/node/13256/download> (last accessed August 22, 2018).
- Biot, M. A. (1941). A mechanical analyzer for the prediction of earthquake stresses, *Bull. Seismol. Soc. Am.* 31, 151-171.
- Boore, D. M. (1983). Stochastic Simulation of High Frequency Ground Motions Based on Seismological models of the Radiated Spectra, *Bull. Seismol. Soc. Am.* 83, 1064-1080.
- Boore, D. M. (2000). SMSIM – Fortran programs for simulating ground motions from earthquakes: Version 2.0. – A revision of OFR 96-80-A. USGS OFR 2000-509. doi: 10.3133/ofr00509.
- Boore, D. M. (2003). Simulation of Ground Motion Using the Stochastic Method. *Pure Appl. Geophys.* 160, 635-676

- Boore, M. D., and Atkinson, G. M. (2006). Earthquake Ground-Motion Prediction Equations for Eastern North America. *Bull. Seismol. Soc. Am.* 96 (6): 2181-2205.
- Boore, M. D., and Atkinson, G. M. (2008). Ground-Motion Prediction Equations for the Average Horizontal Component of PGA, PGV, and 5%-Damped PSA at Spectral Periods between 0.01 s and 10.0 s, *Earthquake Spectra*, 24(1): 99-138.
- Boore, D. M., Stewart, J. P., Seyhan, E., Atkinson, G. M. (2013). NGA-West2 Equations for Predicting Response Spectral Accelerations for Shallow Crustal Earthquakes
- Brune, J. N. (1970). Tectonic stress and the spectra of seismic shear waves from earthquakes. *J. Geophys. Res.* 75, 26, 4997-5009.
- Brune, J. N. (1971). Correction: Tectonic stress and the spectra of seismic shear waves, *J. Geophys. Res.* 76, 20, 5002.
- Campbell, K. W. (2002). Development of semi-empirical attenuation relationships for the CEUS, Report to U.S. Geological Survey, NEHRP Award No.01HQGR0011.
- Campbell, K. W. (2003). Prediction of strong ground motion using the hybrid empirical method and its use in the development of ground-motion (attenuation) relations in eastern North America, *Bull. Seismol. Soc. Am.* 93, 1012–1033.
- Consortium of Universities for Research in Earthquake Engineering (1997). *Historic Developments in the Evolution of Earthquake Engineering.*
- Cornell, C. (1968). Engineering Seismic Risk Analysis. *Bull. Seismol. Soc. Am.* 58, 1583-1606.
- Ellsworth, W. (2013). Injection-Induced Earthquakes, *Science* 341, 1225942.
- Frankel, A. (2009). A constant stress-drop model for producing broadband synthetic seismograms: Comparison with the Next Generation Attenuation relations, *Bull. Seismol. Soc. Am.* 99, 664-681.
- Gutenberg, R. and Richter, C.F. (1944). Frequency of earthquakes in California, *Bulletin of the Seismological Society of America*, 34, 185-188.
- Hanks, T. C. (1979). b Values and $\omega^{-\gamma}$ Seismic Source Models: Implications for Tectonic Stress Variations Along Active Crustal Fault Zones and the Estimation of High-Frequency Strong Ground Motion, *J. Geophys. Res.* 84, 2235-2242.
- Hanks, T. C., McGuire, R. K. (1981). The Character of High-Frequency Strong Ground Motion, *Bull. Seismol. Soc. Am.* 71, 2071-2095.

- Hanks, T. C., and Kanamori, H. (1979). A moment magnitude scale. *Journal of Geophysics Research*. 84, 2348-2350.
- Hassani, B., and Atkinson, G. M. (2015). Referenced empirical ground-motion model for Eastern North America, *Seismol. Res. Lett.* 86(2A), 477-491.
- Hassani B., and Atkinson G. M. (2018). Adjustable Generic Ground-Motion Prediction Equation Based on Equivalent Point-Source Simulations: Accounting for Kappa Effects. *Bull. Seismol. Soc. Am.* 108(2), 913-928.
- Housner, G. W. (1941). Calculation of the response of an oscillator to arbitrary ground motion. *Bull. Seismol. Soc. Am.* 31, 143-149.
- Housner, G. W., and McCann (1949). The analysis of strong-motion earthquake records with electric analog computer, *Bull. Seismol. Soc. Of Am.* 39, 47-56.
- Hudson, D. E. (1962). Some problems in the application of spectrum techniques to strong-motion earthquake analysis. *Bull. Seismol. Soc. Am.* 39, 47-56.
- Iwan, W. D. (1960). Digital Calculation of Response Spectra and Fourier Spectra, Unpublished Note, Calif. Inst. Of Tech., Pasadena.
- Keranen, K., Weingarten, M., Abers, G., Bekins, B., and Ge, S. (2014). Sharp Increase in Central Oklahoma Seismicity Since 2008 Induced by Massive Wastewater Injection, *Science* 345, 448-451.
- Lermo, J. and Chavez Garcia, F. (1993). Site effect evaluation using spectral ratios with only one station. *Bull. Seismol. Soc. Am.* 83, 1574-1594.
- Madariaga, R. (2006). Seismic source theory, chapter 2 in volume 4 *Earthquake Seismology, Treatise on Geophysics* (H. Kanamori ed.).
- McGuire, R. (1977). Seismic design spectra and mapping procedures using hazard analysis based directly on oscillator response, *International Journal of Earthquake Engineering and Structural Dynamics*, 5, 211-234.
- McGuire, R. K. and Hanks, T. C. (1980). RMS Accelerations and Spectral Amplitudes of Strong Ground Motion During the San Fernando, California, Earthquake, *Bull. Seismol. Soc. Am.* 70, 1907-1919.
- Nigam & Jennings (1969), Calculation of Response Spectra from Strong-Motion Earthquake Records, *Bulletin of the Seismological Society of America* 59(2), 909-922.
- Petersen, et al. (2016). USGS Open-File Report 2016-1035, <https://pubs.er.usgs.gov/publication/70182572> (Last accessed November 2016).

- Petersen, et al. (2017). 2017 One-Year Seismic-Hazard Forecast for the Central and Eastern United States from Induced and Natural Earthquakes. *Seismological Research Letters*. 83 (3): 772-783.
- Petersen, et al. (2018). 2018 One-Year Seismic Hazard Forecast for the Central and Eastern United States from Induced and Natural Earthquakes. *Seismological Research Letters*. 89 (3): 1049-1061.
- Pezeshk, S., Zandieh, A., and Tavakoli, B. (2011). Hybrid empirical ground-motion prediction equations for eastern North America using NGA models and updated seismological parameters, *Bull. Seismol. Soc. Am.* 101, 1859–1870.
- Scherbaum, F., Bommer, J. J., Bungum, H., Cotton, F., and Abrahamson, N. A. (2005). Composite ground motion models and logic trees: Methodology, sensitivities, and uncertainties, *Bull. Seismol. Soc. Am.* 95, 1575–1593.
- Schultz, R., Stern, V., Novakovic, M., Atkinson, G. M., Gu, Y. (2015). Hydraulic Fracturing and the Crooked Lake Sequences: Insights Gleaned from Regional Seismic Networks. *Geophysical Research Letters*.
Doi:10.1002/2015GL063455.
- Siddiqi J., and Atkinson G. M. (2002). Ground motion amplification at rock sites across Canada, as determined from the horizontal-to-vertical component ratio. *Bull. Seismol. Soc. Am.* 89, 888-902.
- Silva, W. J., Gregor, N.J., and Darragh, R. (2002). Development of Regional Hard Rock Attenuation Relations for Central and Eastern North America, Technical Report, Pacific Engineering and Analysis, El Cerrito, CA.
www.pacificengineering.org.
- Somerville, P., Collins, N., Abrahamson, N., Graves, R., Saikia, C. (2001). Ground motion attenuation relations for the central and eastern united states, Report to U.S. Geological Survey, NEHRP Award Number 99HQGR0098, 38 pp.
- Somerville, P., Graves, R., Collins, N., Song, S. G., Ni, S., and Cummings, P. (2009). Source and ground motion models of Australian Earthquakes, Proc. Of the 2009 Annual Conference of the Australian Earthquake Engineering Society, Newcastle, Australia, December 2009.
- Toro, G. R., Abrahamson, N. A., Schneider, J. F. (1997). A model for strong Ground Motions from Earthquakes in Central and Eastern North America: Best Estimates and Uncertainties. *Seismological Research Letters*, 68 (1), 41-57.
- Trifunac, M. D. (1971). Response envelope spectrum and interpretation of strong earthquake ground motion. *Bull. Seismol. Soc. Am.* 61 (2), 343-356.

- United Kingdom Onshore Oil and Gas (UKOOG) (2013).
<http://www.ukoog.org.uk/knowledge-base/seismicity-kb/what-is-the-industry-doing-to-mitigate-induced-seismicity>. (last accessed November 24, 2014).
- Yenier, E., and Atkinson, G. M. (2015a). An Equivalent Point-Source Model for Stochastic Simulation of Earthquake Ground Motions in California. *Bull. Seismol. Soc. Am.* 105(3), 1435-1455.
- Yenier, E., and Atkinson, G. M. (2015b). Regionally-Adjustable Generic Ground-Motion Prediction Equation based on Equivalent Point-Source Simulations: Application to Central and Eastern North America. *Bull. Seismol. Soc. Am.* 105(4), 1989-2009.
- Wald, D.J., V. Quitoriano, T.H. Heaton, H. Kanamori, C.W. Scrivner, and C.B. Worden (1999). TriNet "ShakeMaps": Rapid Generation of Peak Ground-motion and Intensity Maps for Earthquakes in Southern California, *Earthquake Spectra* 15(3), 537-556.

Chapter 2

2 Preliminary Evaluation of Ground Motions from Earthquakes in Alberta

2.1 Introduction

Between September 9, 2013 and January 22, 2015 more than 900 seismic events in the local magnitude (ML) range from 1 to 4 were detected and located in near-real-time by the new TransAlta/Nanometrics network in Western Alberta, which commenced operation in the fall of 2013. The network is comprised of 27 three-component broadband seismograph stations, located as shown in Figure 2.1, which act in cooperation with other real-time seismograph stations operated by the Alberta Geological Survey (AGS) (Stern et al., 2011) and the Geological Survey of Canada (GSC). There are additional campaign-mode stations in the Canadian Rockies and Alberta Network (CRANE) operated by the University of Alberta (Gu et al., 2011).

In this study, we compile and analyze a ground-motion database of 5%-damped pseudo-acceleration response spectra (PSA) from the signals recorded on the TransAlta/Nanometrics stations, to gain an initial understanding of overall ground-motion source, attenuation and site characteristics in the region. A catalog of events is provided on www.inducedseismicity.ca; the locations and initial magnitudes of events were obtained from the Athena website operated by Nanometrics on behalf of the project. We processed the recorded time series as described in Assatourians and Atkinson (2010). Briefly, the velocity time series are corrected for glitches and trends, then filtered and corrected for instrument response in the frequency domain. Differentiation to generate acceleration time series is done in the frequency domain before conversion back to the time domain. Horizontal and vertical peak ground velocity (PGV) and peak ground acceleration (PGA) values are computed from peak amplitudes of instrument-corrected time series, and 5% damped pseudo spectral accelerations are calculated from the corrected acceleration time series following the Nigam and Jennings (1969) formulation for the computation of response spectra. The results of the processing procedures were

validated against other standard processing software, as described in Assatourians and Atkinson (2010).

The TransAlta/Nanometrics data will be supplemented in the future with recordings from the AGS, GSC and CRANE networks, but these networks require significant additional compilation and processing effort to obtain reliable ground-motion amplitudes. In particular, we have encountered quality-control issues in the instrument response information in some cases, which has made it difficult to utilize all stations from all networks. Therefore, in our initial evaluation, we focus on the high-quality standard for the exchange of earthquake data (SEED) datafiles provided by the TransAlta (operated by

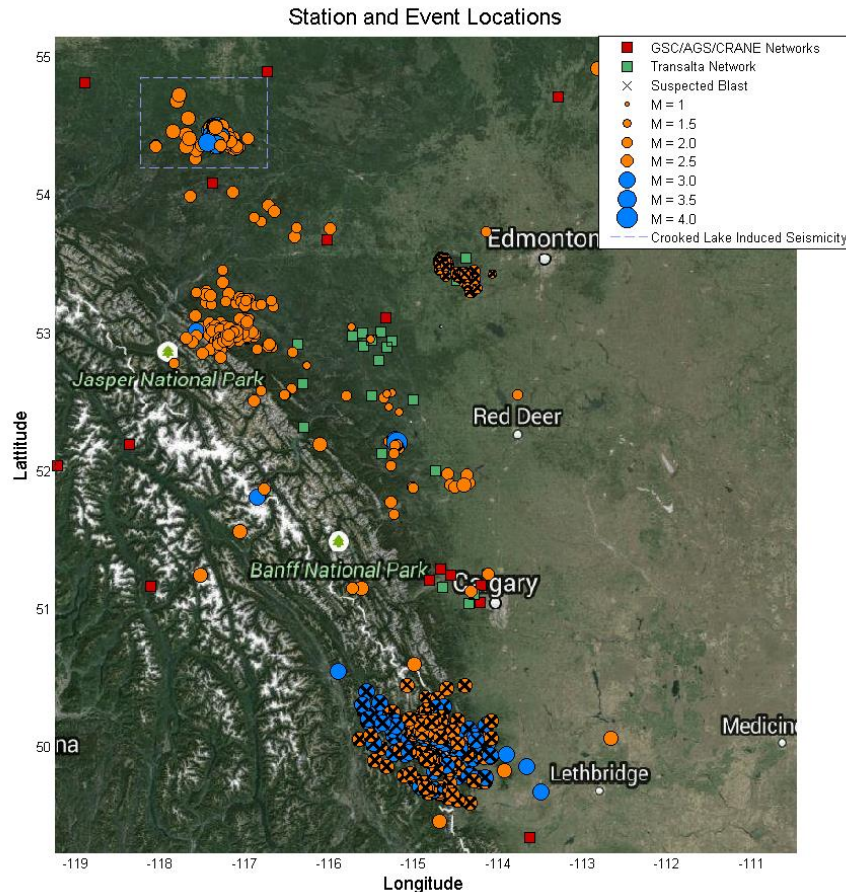


Figure 2.1 Map of stations and study events in Alberta. Events which are considered to be blasts are designated by an x. Note that the deformation front that marks the boundary of the Rocky Mountains is distinguishable by topography.

Nanometrics) network, which can be most readily analyzed.

An issue encountered in the database compilation is that many of the seismic events listed in the catalog are suspected to be blasts from mining or quarry operations, which are difficult to distinguish automatically from earthquakes (either natural or induced) in near-real-time operations. A manual review of waveforms from all events across the province is beyond the scope or resources of the analysis team (such reviews are conducted only for events in areas of particular interest to the client). For this study we are relying on a blast discrimination technique developed by Fereidouni et al. (2015), which is based on the ratio of the vertical component PSA over the horizontal component PSA at a frequency of 10.0 Hz ($PSAH(10.0)/PSAV(10.0)$). Fereidouni et al. (2015) have shown that $PSAH(10.0)/PSAV(10.0)$ is much greater for blasts than for earthquakes, for observations recorded within 100 km of the event. This technique is only applicable for some of the areas of our database, since it requires the existence of stations within 100 km. Our discrimination of blasts, as shown in Figure 2.1, is thus preliminary. For example, we suspect that many of the events in the area near Jasper National Park are also blasts, but we are not yet able to automatically distinguish blasts from earthquakes in this region. Therefore, we have retained the earthquake designation for these events at present.

Another important issue in the database evaluation that is not yet resolved is the discrimination of natural events from those that suspected to be induced. Approximately 80% of the events in our database occur in distinct clusters in time and space that are characteristics of induced events. The locations of most of these clusters coincide with areas suspected to be induced-seismicity sources, on the basis on other studies. For example, events in the Crooked Lake region are strongly related in temporally and spatially to hydraulic fracturing in horizontal wells in the Duvernay formation (Schultz et al., 2015). Events in the Brazeau River region (south of Crooked Lake and west of Edmonton) are strongly correlated with activities at a disposal well in the area (Shultz et al., 2014), while events in the Rocky Mountain House area (west of Red Deer) have been related to gas extraction activities (Baranova et al., 1999). In this study, we do not attempt to distinguish natural from induced seismicity on an event-by-event basis, as this

would be beyond the present scope. However, as noted above, due to the location and timing of events we believe that the great majority of them (~80%) are potentially induced.

2.2 Magnitude Evaluations

For each event in the database, we have estimated the moment magnitude (\mathbf{M}) using the PSA-based algorithm of Atkinson, Greig and Yenier (2014, denoted AGY14):

$$\mathbf{M} = \frac{(\log_{10}(PSA_F) - MC_F + Z(R_{Hypo}) + \gamma F)}{1.45} \quad (2.1)$$

where R_{Hypo} is hypocentral distance and $Z(R_{Hypo})$ is a geometric spreading model:

$$Z(R) = 1.3 \log_{10}(R_{Hypo}) \quad \text{for } R_{Hypo} \leq 50 \text{ km} \quad (2.2a)$$

$$Z(R_{Hypo}) = 1.3 \log_{10}(50) + 0.5 \log_{10}(R_{Hypo} / 50) \quad \text{for } R > 50 \text{ km} \quad (2.2b)$$

PSA_F is the PSA value of the vertical component at frequency F , MC_F is an empirical calibration term, γ_F is the anelastic attenuation term at frequency F . As recommended by AGY14, we set the focal depth (h) to 5 km to enable a rapid and robust determination of R , even if the depth is not well known. It is noted that the computed value of R is not sensitive to h , with the exception of the rare observations that are made very close to the source. Our preliminary evaluation of attenuation (as shown later in this paper) suggests that the Western North American (WNA) crustal attenuation model is appropriate for the study events in this region, regardless of whether the events are east or west of the deformation front that marks the edge of the Rocky Mountains (visible in Figure 2.1). For WNA, AGY14 gives recommended values for γ_F and MC_F as noted in Table 2.1, which we adopt for use in magnitude determination. We use Equation 2.1 to calculate \mathbf{M} for each observation, based on the observed vertical PSA (PSA_v) and R_{Hypo} . AGY14 suggest that \mathbf{M} be calculated from at least three records from the 1.00 Hz PSA_v in general, but that for events of $\mathbf{M} < 3$ it is preferable to use the 3.33 Hz PSA_v due to noise issues that inflate the 1.00-Hz amplitudes. The question then arises as to which ground-motion measure to use for events that are close to $\mathbf{M} 3$, as slightly different values will

result based upon this choice. Moreover, the estimated value will also depend somewhat on the distance constraints applied, as noise issues become more prevalent at more distant

Table 2.1: WNA anelastic attenuation and empirical calibration terms for 1.00 Hz and 3.33 Hz frequencies

	<u>1.00 Hz</u>	<u>3.33 Hz</u>
MC_F	-4.25	-3.15
γ_F	0.0035	0.004

stations. Based on our preliminary evaluation of the ground-motion data and its attenuation and noise behavior with distance, we have restricted the distance range of stations used in magnitude determination as follows: we use all stations with $R < 150$ km for events of $M \leq 2.6$, and all stations with $R < 300$ km for events with $M > 2.6$. We exclude any station whose value of M exceeds $\pm 2\sigma$ of the event average, where σ is the standard deviation, as a quality-control measure. The average M for each event is recalculated after this initial screening, using both the 1.00 Hz and 3.33 Hz definitions (denoted $M(1.00 \text{ Hz})$ and $M(3.33 \text{ Hz})$). The final M assigned to an event is determined based on the following criteria:

- (i) if $M(1.00 \text{ Hz}) < 3$ and $M(3.33 \text{ Hz}) < 3$, then $M = M(3.33 \text{ Hz})$; or
- (ii) if $M(1.00 \text{ Hz}) \geq 3$ and $M(3.33 \text{ Hz}) \geq 3$, then $M = M(1.00 \text{ Hz})$; otherwise
- (iii) $M = (M(1.00 \text{ Hz}) + M(3.33 \text{ Hz})) / 2$

In other words, we use the 3.33Hz measure when M is clearly below 3, the 1.00 Hz measure when M is clearly above 3, or an average of the two when the measures are ambiguous. The estimated value of M is plotted against the local magnitude (M_L) values, as computed by Nanometrics, in Figure 2.2. In general, the calculated value of M tracks the 1:1 line against M_L well for events of $M > 2.6$; for such events, the average value of

$M - M_L = -0.17 \pm 0.06$. We note there is a cluster of events of high M_L relative to the overall trend. The M_L of these events may tend to be overestimated because they occurred in the Fox Creek area (outlined by the dashed box in figure 2.1) where the network coverage of the TransAlta/Nanometrics network is poor. The inclusion of distant noisy stations may have biased the magnitude estimates for these events. The low-magnitude range on Figure 2.2 is also affected by noise issues, as indicated by the departure of the M_L versus M trend from the 1:1 line. For very weak motions, the response of an oscillator is driven by low-frequency noise, even at higher frequencies. The ideal solution would be to have quieter sites, but this would require expensive borehole installations. A more practical short-term alternative is to devise an appropriate correction for the noise to reduce the bias in the determined values of M . By inspection of Figure 2.2, we suggest that such a correction for the stations of the TransAlta/Nanometrics network in Western Alberta is given by the line:

$$M_{\text{corr}} = 2M - 2.6 \quad \text{for } M < 2.6 \quad (2.3)$$

where M_{corr} is the noise-corrected estimate of the moment magnitude, based on the

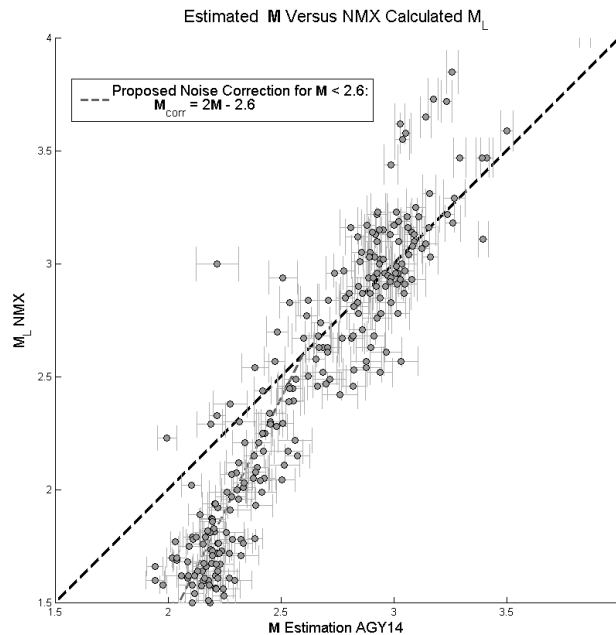


Figure 2.2: Estimated M versus M_L (excluding events designated as blasts). Standard error of M estimates are also shown (horizontal bars, with verticals to denote edges).

computed value of M .

2.3 Evaluation of Ground Motions

Figure 2.3 shows the distribution of events in magnitude and distance space, after correction of the M value for noise as indicated in Equation 2.3. Ground motions have been compiled into a database. PSA values from the vertical and horizontal components, for sample frequencies between 0.2 Hz and 50.0 Hz, are compiled along with metadata. The metadata include the date, time, event location, station location, hypocentral distance, estimated M_{corr} , other computed magnitudes, such as M_L (where available) and focal depth (where known).

In Figures 2.4 and 2.5, we provide an initial overview of the motions and their attenuation, at 1.00 Hz and 3.33 Hz, for events of $M \sim 3$. We compare the observed amplitudes to the WNA equation of AGY14 used to define M , and to the ground-motion prediction equation (GMPE) of Atkinson (2015) developed for small-to-moderate events. The Atkinson (2015) GMPE was developed from PSA data in a similar magnitude range in California. Note that the AGY14 equation is for the vertical component (assumed to

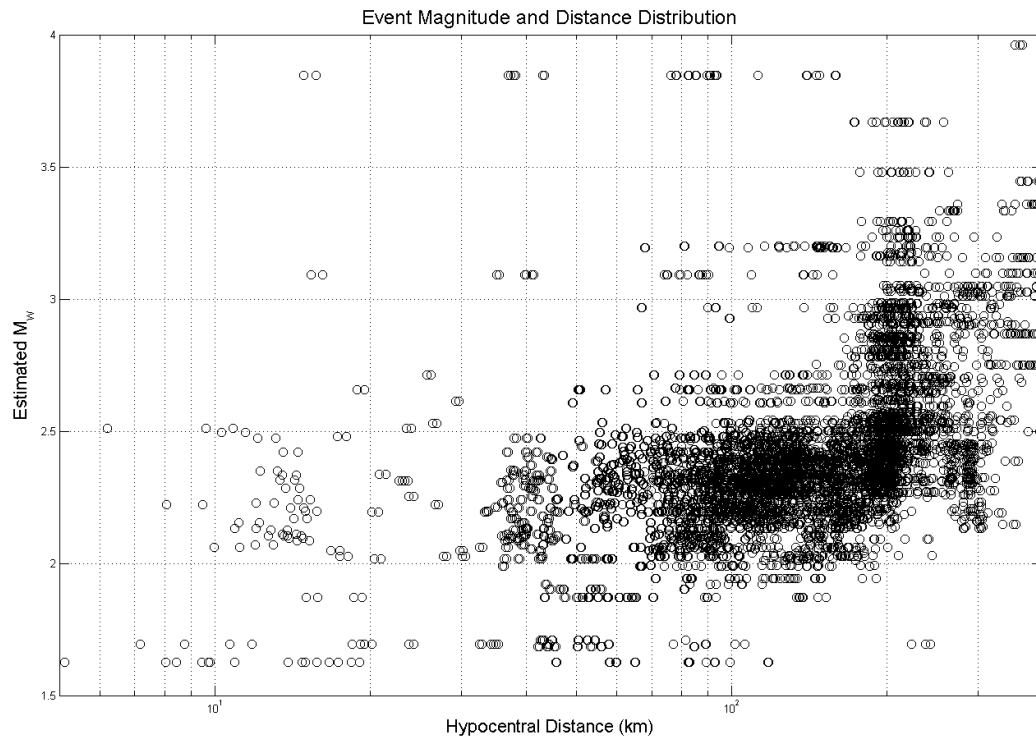


Figure 2.3: Distribution of events (blasts excluded) in M and distance.

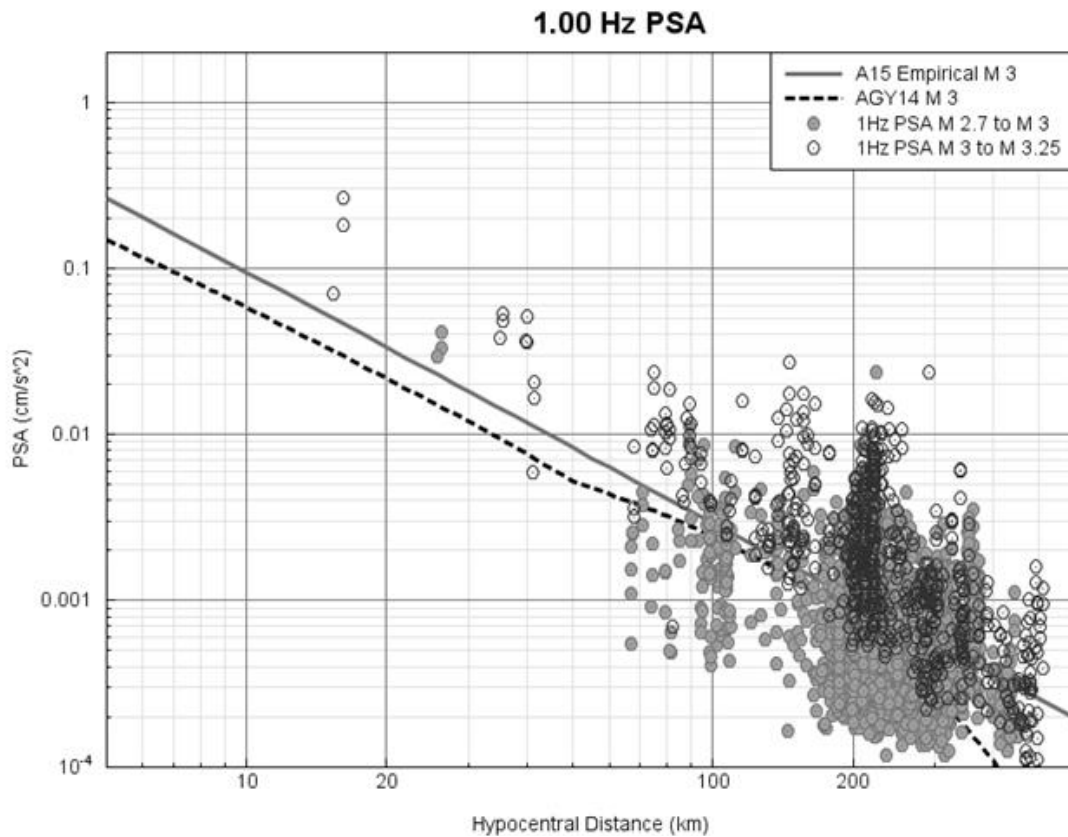


Figure 2.4: PSA amplitudes (all components) at 1.00 Hz for events of $M = 3.0 \pm 0.3$, as a function of hypocentral distance, compared to the relations of AGY14 (vertical component) and A15 (horizontal component, B/C conditions).

have negligible site response), while A15 is for the geometric mean of the horizontal components, for B/C site conditions (near-surface shear-wave velocity of 760 m/s); all three observed components are plotted. Overall, the motions are in qualitative agreement with the expected amplitude and attenuation trends suggesting that overall the western attenuation model is a reasonable first approximation. This is perhaps surprising, as we might have expected a mixture of eastern and western attenuation types in this region, as it is close to the deformation front. It could be that crustal complexity extends several hundred kilometers east of the deformation front, such that the entire region is more western than eastern in tectonic setting. We examine our first impressions in more detail in the following.

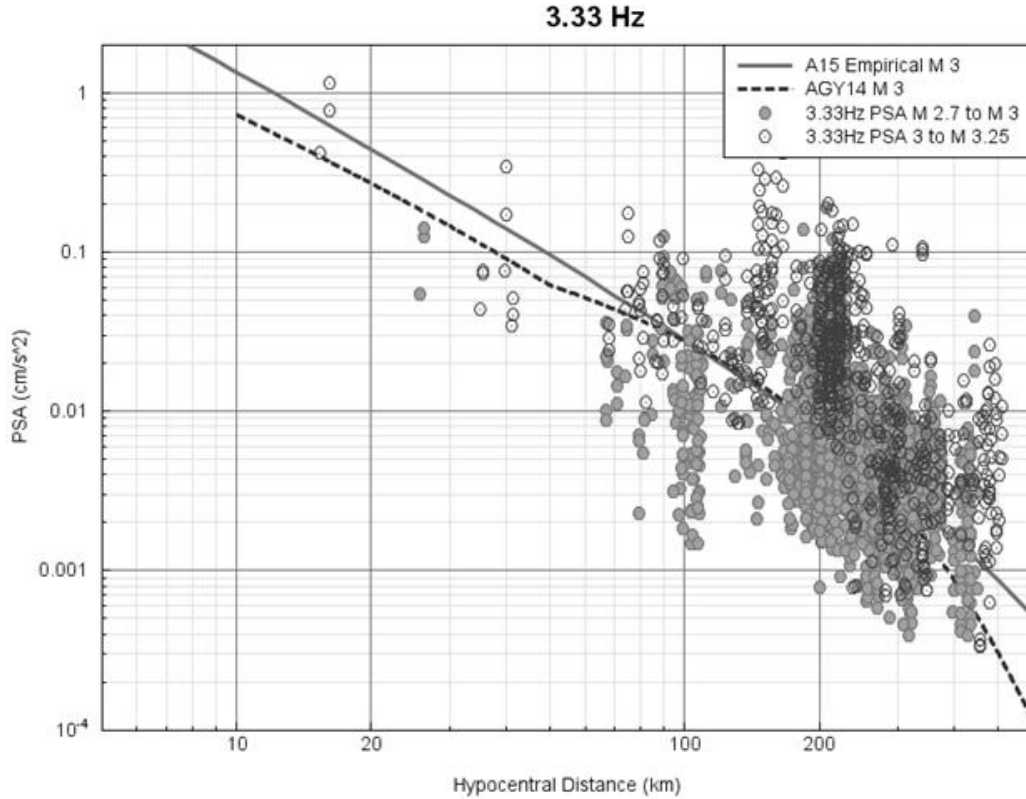


Figure 2.5: PSA amplitudes (all components) at 3.33 Hz for events of $M = 3.0 \pm 0.3$, as a function of hypocentral distance, compared to the relations of AGY14 (vertical component) and A15 (horizontal component, B/C conditions).

To gain insight into the attenuation and magnitude-scaling features of the ground-motion data, it is useful to evaluate the residuals relative to a reference prediction equation (where the residual for an observation is defined as $\log_{10}(\text{PSA}_{\text{obs}}) - \log_{10}(\text{PSA}_{\text{pred}})$). Trends in the differences between observations and predictions plotted versus distance allow us to refine our model of attenuation with distance, whereas trends in magnitude are informative for source scaling. A constant offset may reflect a combination of effects including differences in source level (i.e., stress parameter) and site amplification. For the predicted values, we use the A15 small- M empirical GMPE developed for California, including the recommended additional c_4 term to extend the GMPE to regional distances. Thus, the reference prediction GMPE is given by (Atkinson, 2015):

$$\log(\text{PSA}) = c_0 + c_1 M + c_2 M^2 + c_3 \log(R_{\text{eff}}) + c_4 R_{\text{eff}} \quad (2.4)$$

where R_{eff} is an effective point-source distance that includes near-source distance-saturation effects using an effective depth parameter (Yenier and Atkinson, 2014):

$$R_{\text{eff}} = \sqrt{R_{\text{Hypo}}^2 + h_{\text{eff}}^2} \quad (2.5)$$

R is hypocentral distance and:

$$h_{\text{eff}} = \max(1, 10^{-1.72+0.43M}) \quad (2.6)$$

Note that a minimum value of $h_{\text{eff}}=1$ km is specified; this is the value taken by Equation (2.6) when $M=4$. This ensures the scaling of ground motions near the source approaches a constant as the hypocenter (or fault plane) is approached. Figure 2.6 plots the PSA residuals with respect to the A15 model, where the event magnitude is as calculated by the AGY14 M estimation model described in the foregoing. To focus on higher-quality data, we consider only events of $M \geq 2.6$. The site conditions are not well known and are currently under investigation. However, all sites have posthole seismometers driven into the surficial soil layer. The instruments are thus founded at the level of resistance for a posthole auger. It is possible that this results in a relatively common site condition among the stations, if the regional near-surface geology is not highly variable in nature. If so, this would be a significant benefit to this installation method. In this study, we do not attempt to subtract site effects from the observations, as they are so poorly known. Rather, we use the comparisons between observations and prediction equations to infer what site response terms might account for the observed residuals and evaluate whether these are reasonable. For example, residuals for the vertical-component observations with respect to A15 might be expected to be minimal, under the assumption that the vertical component is a proxy for the unamplified horizontal-component motions (e.g., Lermo and Chavez Garcia, 1993; Ghofrani and Atkinson, 2014). By contrast, we might expect significant positive residuals for the horizontal components as the instruments are located within the soil layer (not on firmer B/C site conditions). What we see in Figure 2.6 is generally consistent with those expectations, with some exceptions. Overall, there is no compelling evidence for significant deviations of the attenuation model from the trends given in the A15 model. However, there are some deviations from a flat trend in

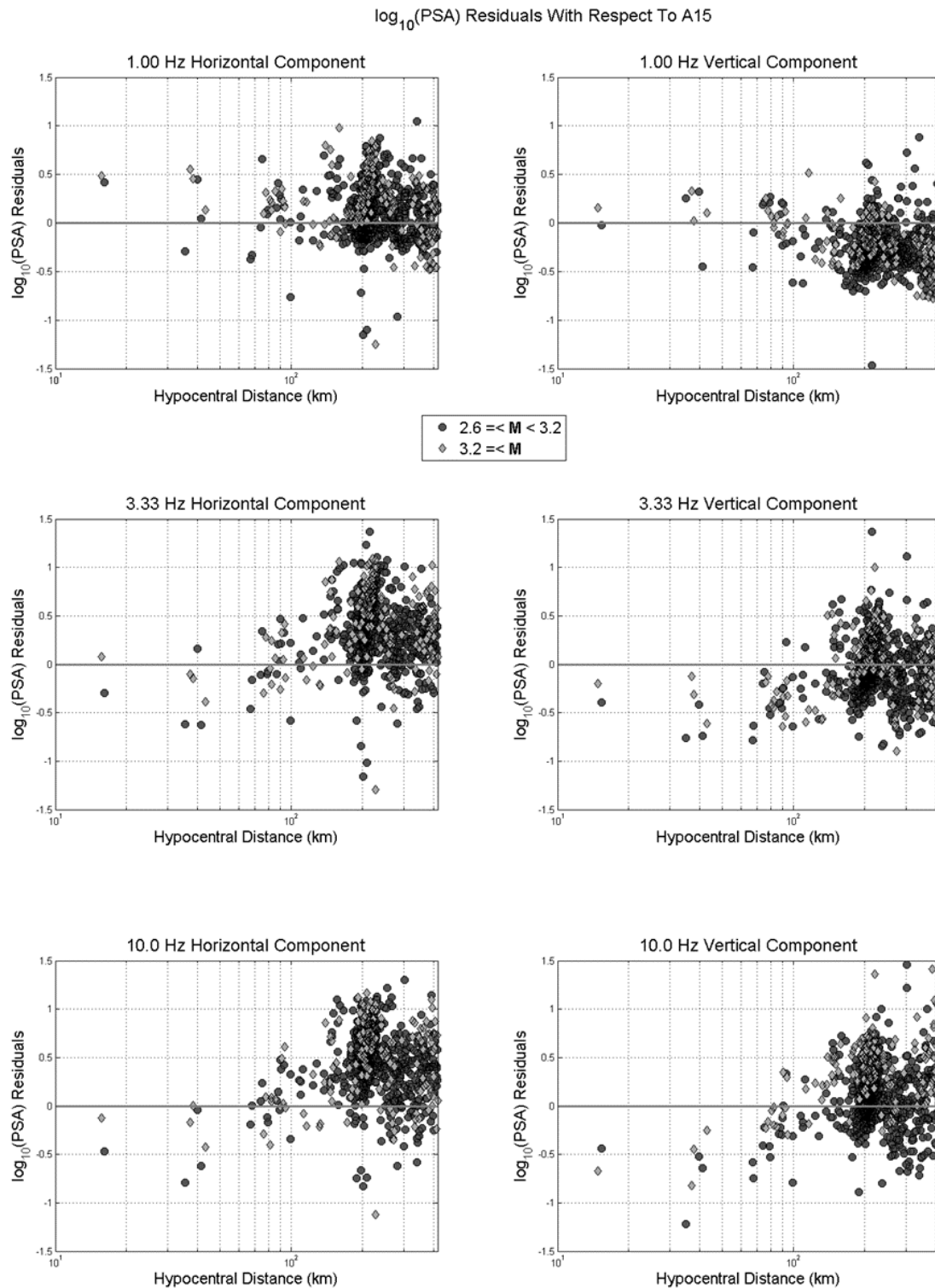


Figure 2.6: PSA Residuals for $M \geq 2.6$ for PSA at 1.00 Hz (top), 3.33 Hz (middle) and 10.0 Hz (lower), for horizontal (left) and vertical (right) components (blasts removed).

near-zero average residuals with respect to A15 at $R > 150$ km but have negative residuals at closer distances. By contrast, at 1.00 Hz the vertical-component residuals are near-zero at $R < 150$ km, but negative at larger distances. The 1.00 Hz horizontal PSA residuals are generally positive, suggesting significant site amplification; the 3.33 Hz horizontal PSA residuals are also largely positive, but more ambiguous at closer distances. At 10.0 Hz, the residuals are negative at $R < 150$ km on both components, but positive on both components at $R > 150$ km. This suggests that there may be significant effects of noise on the spectral response and/or that a more complex attenuation model may be warranted (perhaps a bilinear model with a change in geometric spreading at $R < 100$ km). These overall trends are shown more clearly in Figure 2.7, which plots the mean and standard error of the residual data of Figure 2.6 binned by distance at 0.2 log₁₀ units in width. Due to the paucity of near-distance data, the only truly compelling trends

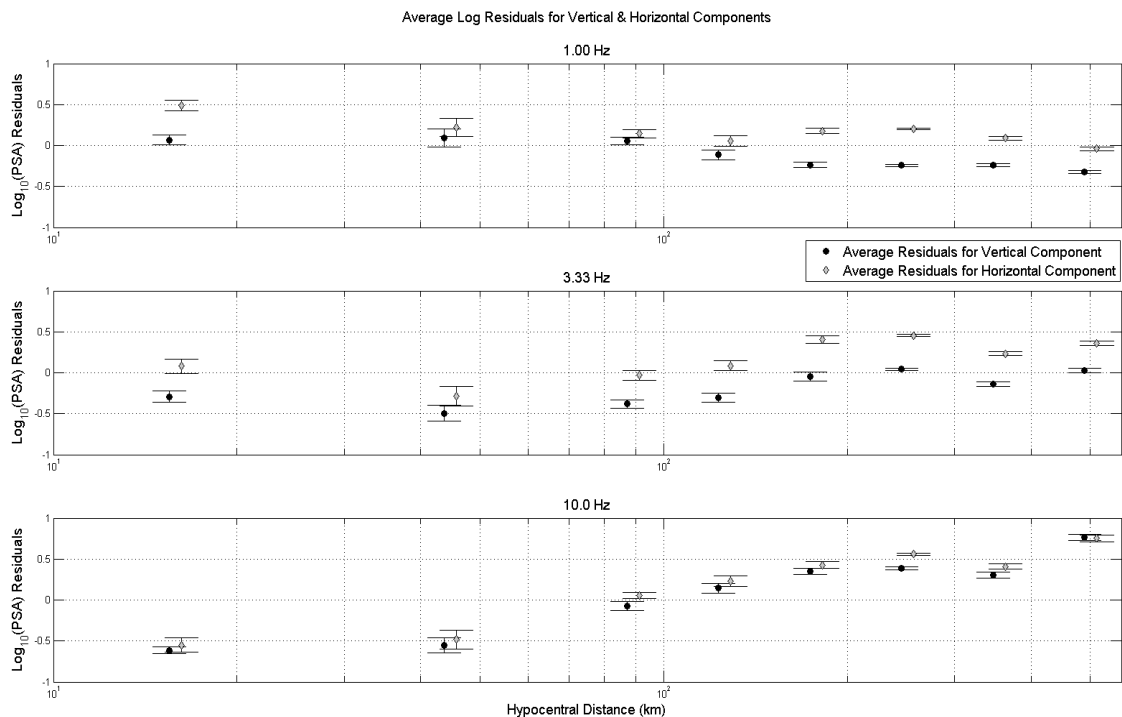


Figure 2.7 Mean and standard error of PSA residuals for $M \geq 2.6$ at 1.00 Hz (top), 3.33 Hz (middle) and 10.0 Hz (lower), binned by log distance, for horizontal and vertical components (no error bar plotted if the number of observations in the bin is < 3). Slight offset from bin center used for plotting clarity (to distinguish horizontal from vertical).

are the positive residuals at $R > 150$ km on the horizontal component at 3.33 Hz, and on both components at 10.0 Hz. The attenuation model will be refined as more observations at close distances are obtained, enabling the trends to be more accurately defined.

If we subtract the terms in c_3 and c_4 of Equation 2.4 from the observed PSA for each station, we can determine average source terms for each event; these are the amplitudes that would be observed at near-source distances. Figure 2.8 plots these source terms relative to the empirical A15 model. The expected magnitude scaling based on the point-source simulation model of Yenier and Atkinson (2015a) for California is also shown (shifted by the appropriate calibration constant so that it matches the level of A15 in the M_3 to 6 range where both are applicable); this model provides the expected scaling for a Brune source model with a stress parameter of 100 bars. It is important to recognize that both the Yenier and Atkinson (2015a) and A15 scaling were defined for events of $M > 3$, and thus both represent significant extrapolations to lower magnitudes on Figure 2.8. At $M > 3$, the empirical and point-source scaling are very close to each other, while the extrapolated scaling at lower magnitudes shows some deviation between the two models. Overall, the magnitude scaling of the source terms is very similar to that expected for a 100-bar point-source model. It should be acknowledged that for the 1.00 Hz scaling, it is expected that it follows the point-source scaling of Yenier and Atkinson (2015a) for events of $M > 3$, as the event magnitudes have been determined from a similar point-source model and thus there is some circularity. However, the scaling in the A15 model is entirely empirical as derived from a different database (the NGA-West2 database). Moreover, as frequency increases, the scaling will not be controlled by the estimated moment magnitude but becomes more dependent on the stress parameter. At 3.33 Hz we observe larger PSA in the horizontal channels than in the vertical channels suggesting a common site response amongst the stations. At 10.0 Hz, the attenuation-corrected ground motions are significantly higher than predicted equivalently in the horizontal and vertical components. However, because of the attenuation trends noted at $R < 150$ km (Figures 2.6 and 2.7), it would be premature to draw conclusions regarding the overall stress parameter from this observation. The scaling behavior with magnitude requires further investigation after sufficient data is obtained to define the attenuation at closer distances, allowing more robust source characterization.

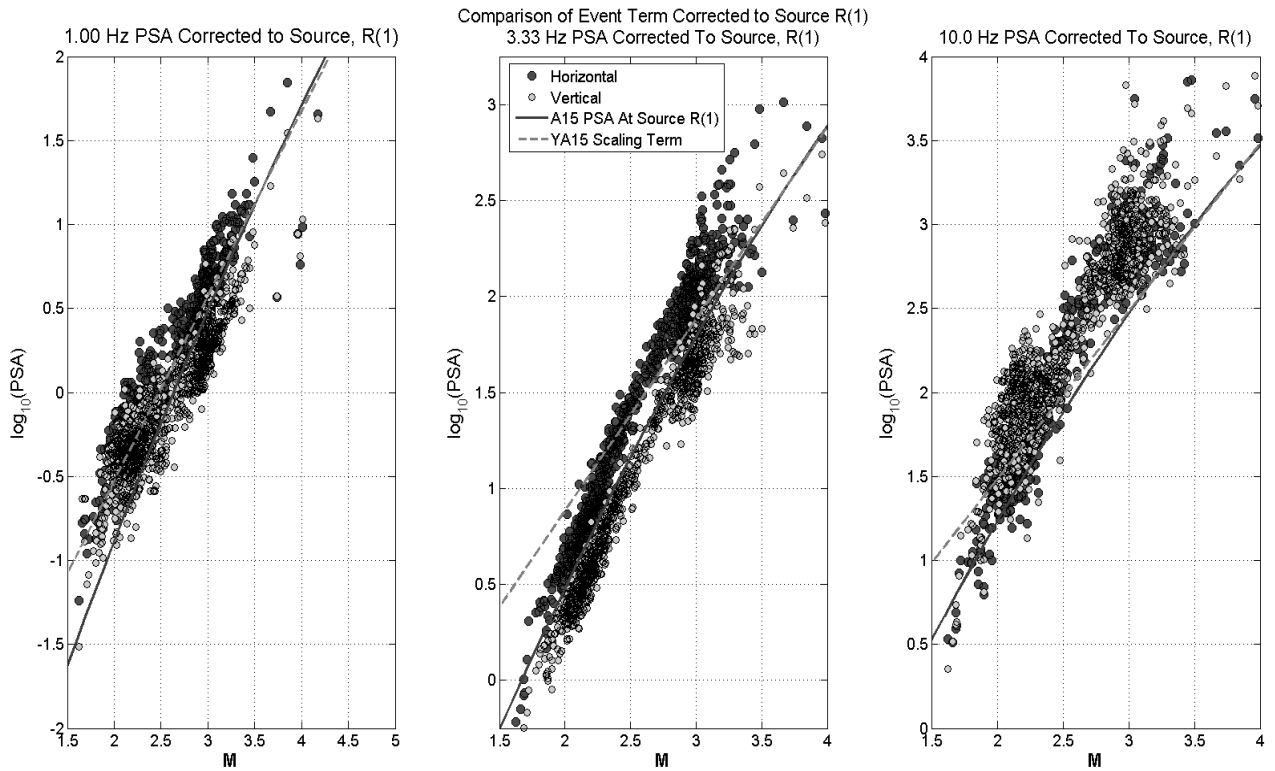


Figure 2.8: Scaling of source terms with magnitude, in comparison to empirical (A15) and simulation-based (Yenier and Atkinson, 2015a) models

In considering the source characteristics of the events, it should be noted that at frequencies of 1.00 Hz and lower, PSA amplitudes are insensitive to stress parameter in the magnitude range covered in this study. However, stress parameter becomes important with increasing frequency, which is at least part of the reason why the scatter is broader at 10.0 Hz in Figure 2.8 than at 1.00 Hz. It has been suggested that stress parameter may be smaller for induced events than for natural events, leading to weaker ground motions (Hough, 2014). This may be primarily a focal depth effect, as Yenier and Atkinson (2015a, b) have shown that stress parameter increases with focal depth in both WNA and Central and Eastern North America (CENA). Specifically, Yenier and Atkinson (2015a,b) have found that average stress parameters for shallow events (<5 km) of M 3 to 5 are about 10 bars on average for WNA, and about 30 bars on average for CENA, although there is much inter-event variability (factor>2). For events with depths of 10 km or greater, the average stress parameters are about 10 times higher than those for very shallow events, in both regions. Thus, the focal depth effect on stress parameter may

overwhelm any differences due to an eastern or western tectonic setting. Furthermore, it may be difficult to distinguish between focal depth effects and event type effects (natural vs. induced) on stress parameter. Further studies with events covering a broader distance range will be required to determine the average stress parameters in this region and to resolve the influence that competing factors such as faulting mechanism, depth effects, and near surface attenuation effects (κ_0) may have upon the stress parameter of events.

In Figure 2.9, we examine the average residual versus frequency in selected distance ranges, for frequencies of 0.50 Hz and greater (noise issues are too severe at lower frequencies). We can interpret Figure 2.9 as an average site response curve for the stations, relative to the reference B/C condition of A15. However, it should be

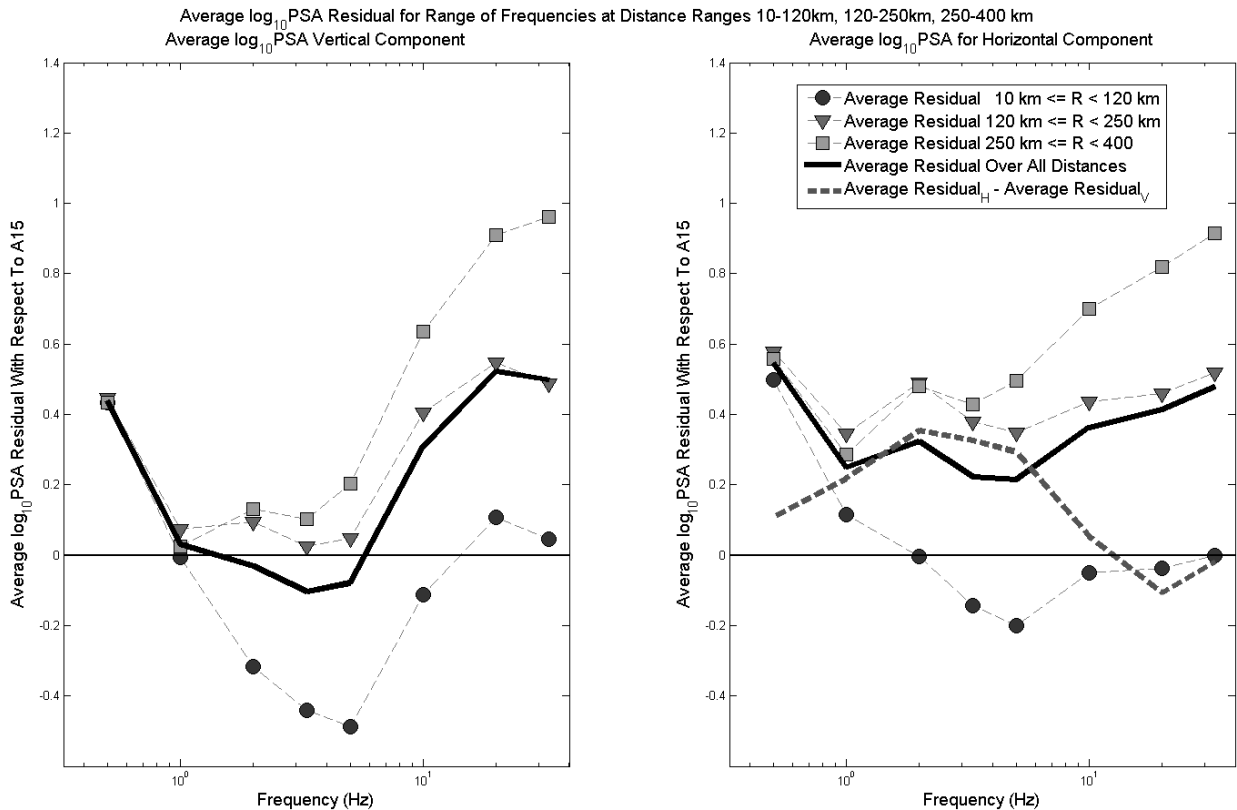


Figure 2.9: Average PSA residuals versus frequency in distance ranges 10-120km, 120-250km, 250-400 km (left=vertical, right=horizontal). Average including all distances is also shown (heavy line). Dashed line on right panel shows the average horizontal residual minus the average vertical residual, which is similar to an average site response function.

acknowledged that this term also includes any net bias, whether or not it is attributable to site conditions or other factors, such as overall source effects, noise issues, etc. Specifically, it is likely that the large positive term at frequencies < 1.00 Hz and frequencies > 10.0 Hz is largely driven by noise. Specifically, the PSA at frequencies $f < 1.00$ Hz is largely attributable to the oscillator response at the prominent 0.30 Hz microseismic noise peak. Noise may also be responsible for the distance-dependence of the average residual term, as it has a relatively larger contribution to amplitudes for the weak motions observed on distant stations. Overall, it appears that the site response is about 0.2 \log_{10} units greater on the horizontal than the vertical component (factor of 1.6). Moreover, there is a noticeable peak in the horizontal response curve at a frequency near 2 Hz that is not present on the vertical component. Finally, the trend to larger amplitudes at high frequencies, relative to the predictions of A15, could reflect a combination of noise and/or lesser near-surface attenuation (e.g. smaller value of the kappa parameter of Anderson and Hough, 1984) relative to California sites.

To remove the influence of noise on the overall site response term in Figure 2.9, which should be common on the vertical and horizontal components, we subtract the average vertical-component response curve from the average horizontal-component response curve. The resulting line (plotted in the right panel of Figure 2.9) is similar to an average H/V ratio plot over all records. It suggests that the dominant feature of the response of these sites is a peak in the frequency range from 2.00-5.00 Hz. This is in agreement with preliminary results of H/V studies for sites in the region (Farrugia et al., 2015). The H/V ratio is a well-known method for estimating the total amount of amplification a site will experience during a seismic event, and in particular for determining the fundamental frequency at that site (Lermo and Chavez Garcia, 1993; Ghofrani and Atkinson, 2014). Preliminary H/V studies (Farrugia et al, 2015) suggest that the TransAlta network stations all have very similar site responses, with a pronounced amplification in the 2 – 5 Hz frequency band on most stations that is consistent with expectations for relatively shallow soft soil sites underlain by hard rock.

If we interpret the differences of residuals as site-response terms, we can infer the amplification relative to the A15 reference condition of B/C by computing the average

residual at each station. As shown in Figure 2.10, the inferred site terms are relatively consistent from one station to the next (consistent with the results of Farrugia et al. 2015). This suggests that an overall typical site amplification curve, as given in Figure 2.9 (dashed line), may be a reasonable way to model site effects at the stations.

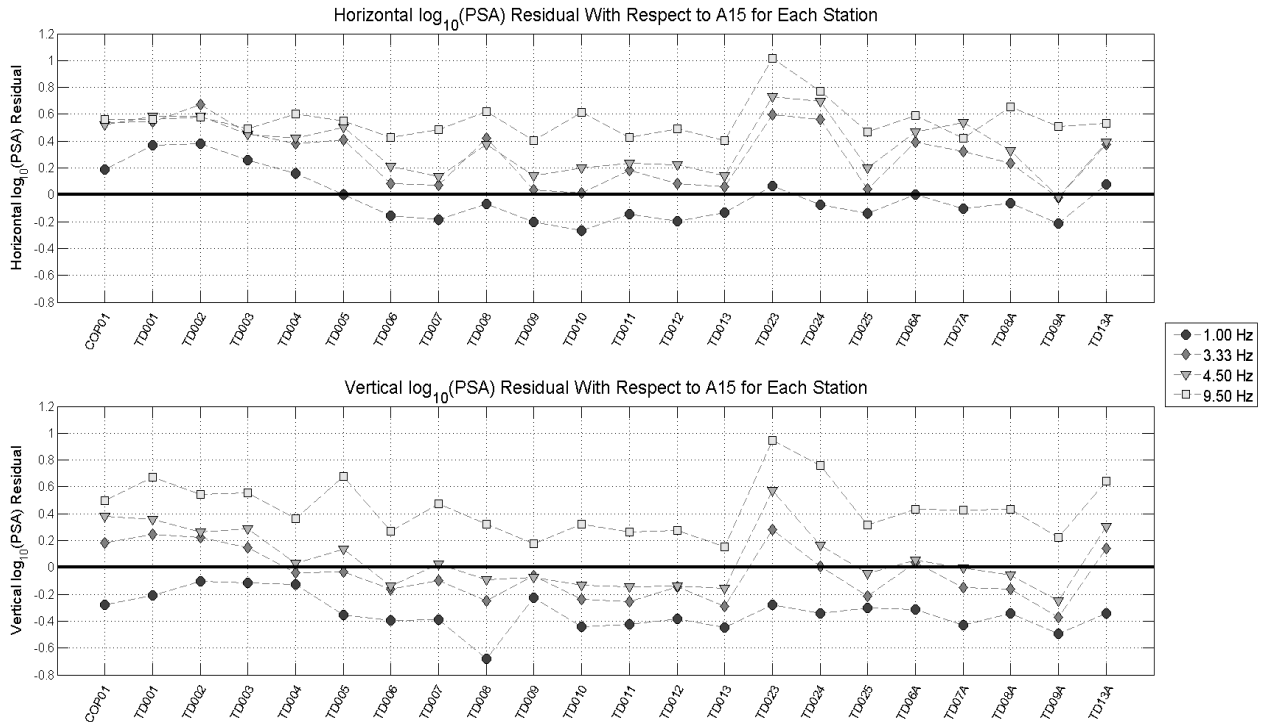


Figure 2.10: Average station residuals for vertical and horizontal components of selected frequencies, for events with $M > 2.6$ (blasts excluded).

As more ground-motion observations are collected, we will be able to further resolve the competing influences of source, attenuation and site factors on the observed ground motions in this region. Ground motions observations at close distances, $R < 50$ km, will be particularly valuable, as will a larger number of events. A larger number of events would facilitate the distinction between natural and induced events, and illuminate any geographical effects related to the tectonic setting (location relative to the deformation front). This will provide a baseline for evaluating whether the ground-motion attributes of induced events differ significantly from those of natural earthquakes, and whether these differences can be entirely attributed to focal depth effects.

2.4 Conclusions

This preliminary evaluation of ground motions in Alberta has determined that:

- (i) The ground motions for small events in Alberta are generally consistent with those for similar-sized events in California (as characterized by the AGY14 and A15 GMPEs) in terms of overall amplitude level and attenuation, but there are region-specific features in the residuals that require further investigation with additional ground-motion data;
- (ii) The scaling characteristics of the Alberta events are generally consistent with expectations based on both empirical (A15) and point-source simulation models (Yenier and Atkinson, 2015a);
- (iii) There appears to be significant site response on the horizontal component in the 2.00 to 5.00 Hz frequency range, which is relatively consistent among stations, suggesting a common site response model for stations in Western Alberta.

2.5 Acknowledgements

This study was financially supported by the Natural Sciences and Engineering Research Council of Canada and TransAlta. The constructive comments of Justin Rubinstein and two anonymous referees are gratefully acknowledged.

2.6 References

- Anderson, J. G., and Hough S. E. (1984). A model for the shape of the Fourier amplitude spectrum of acceleration at high frequencies, *Bull. Seismol. Soc. Am.* 74, 1969 – 1993.
- Assatourians, K., and Atkinson, G. M. (2010). Database of processed time series and response spectra for Canada: An example application to study of the 2005 MN 5.4 Riviere du Loup, Quebec earthquake, *Seismol. Res. Lett.* 81, no. 6, 1013–1031.
- Atkinson G. M., (2015). Ground-motion prediction equation for small-to-moderate events at short hypocentral distances, with application to induced seismicity hazards. *Bull. Seism. Soc. Am.*, **105**(2A), 981-992. DOI: 10.1785/0120140142.

- Atkinson, G. M., Greig, W., and Yenier, E. (2014). Estimation of Moment Magnitude (M) for Small Events ($M < 4$) on Local Networks. *Seismol. Res. Lett.*, **85**, 1116-1124.
- Baranova, V., Mustaqeem, A., and Bell, S. (1999). A model for induced seismicity caused by hydrocarbon production in the western Canada sedimentary basin. *Can. J. Earth Sci.*, **36**, 47-64.
- Farrugia J. and G. M. Atkinson (2015). A Preliminary Evaluation of Site Amplification in Alberta. Undergraduate Thesis, Western University, London Ontario, Canada.
- Fereidoni, A. and G. M. Atkinson (2015). Identifying quarry blast events in seismicity catalogs based on ground motion parameters. Canadian Geophysical Union (CGU) Annual Meeting, Montreal, Canada, 3-7 May 2015.
- Ghofrani, H. and G. M. Atkinson (2014). Site condition evaluation using horizontal-to-vertical spectral ratios of earthquakes in the NGA-West2 and Japanese databases. *J. Soil Dyn. And Earthq. Eng.*, **67**, 30-43.
- Lermo J. and F. Chavez-Garcia (1993). Site effect evaluation using spectral ratios with only one station. *Bull. Seism. Soc. Am.*, **84**, 1350-1364.
- Gu, Y., A. Okeler, L. Shen and S. Contenti (2011). The Canadian Rockies and Alberta Network (CRANE): New constraints on the Rockies and western Canada sedimentary basin. *Seism. Res. L.*, **82**, 575-588.
- Hough, S. (2014). Shaking from injection-induced earthquakes in the central and eastern United States. *Bull. Seism. Soc. Am.*, 104(5): 2619–2626
Doi:10.1785/0120140099.
- Nigam & Jennings (1969), Calculation of Response Spectra from Strong-Motion Earthquake Records, *Bulletin of the Seismological Society of America* 59(2), 909-922.
- Schultz, R., V. Stern and Y. Gu (2014). An investigation of seismicity clustered near the Cordel Field, west central Alberta, and its relation to a nearby disposal well. *J. Geophys. Res., Solid Earth*, **119**, 3410-3423.
- Schultz, R., V. Stern, M. Novakovic, G. M. Atkinson and Y. Gu (2015). Hydraulic fracturing and the Crooked Lake sequences: Insights gleaned from regional seismic networks. *Geophys. Res. L.*, doi 10.1002/2015GL063455.
- Stern, V., R. Schultz and G. Jean (2011). Alberta microseismicity project, Phase 1: Site assessments for the ATSN semipermanent stations and the PSEIP Strachan temporary seismic array. Energy Resources Conservation Board, ERCB/AGS Open File Rpt. 2011-15, 75pp.

- Yenier, E. and G. M. Atkinson (2015a). An Equivalent Point-Source Model for Stochastic Simulation of Earthquake Ground Motions in California. *Bull. Seism. Soc. Am.*, **105**(3), 1435-1455.
- Yenier, E. and G. M. Atkinson (2015b). Regionally-adjustable generic Ground-Motion Prediction Equation based on stochastic point-source simulations: Application to Central and Eastern North America. *Bull. Seism. Soc. Am.*, **105** (4): 1989-2009. DOI: 10.1785/0120140332

Chapter 3

3 Empirically Calibrated Ground Motion Prediction Equation for Oklahoma

3.1 Introduction

More than 13,000 seismic events in the moment magnitude (M) range from 1 to 5.8 were detected and located across the state of Oklahoma from January 1, 2010 to December 1, 2016. Prior to 2009, an annual average of 21 earthquakes of $M \geq 3$ was observed. Annual seismicity rates of such events increased to ~ 100 /year from 2009 to 2013, and by 2015 the annual rate had risen to ~ 1000 $M \geq 3$ (Peterson et al, 2016; see Data and Resources). Most events are considered to have been induced by waste water injection, but it is not within the scope of this study to attempt an event-by-event classification. Hundreds of the events have been strongly felt, whilst the largest two earthquakes, the $M5.7$ Prague and $M5.8$ Pawnee events, had reports of damage to infrastructure in nearby cities (e.g. Ellsworth, 2013). A pre-requisite for assessing and mitigating the hazard posed by induced earthquakes in Oklahoma is an understanding of the ground motions that they produce. Ground-motion prediction equations (GMPEs), expressing peak ground motion and response spectral amplitudes as functions of magnitude, distance and site condition, are a valuable tool for characterizing ground motion in a format that is useful for seismic hazard analysis (e.g. McGuire, 2004) and near-real-time ShakeMaps (e.g. Wald et al., 1999).

In this study, a region-specific GMPE for Oklahoma (median horizontal component) is developed using a compiled database of ~ 7278 ground motion observations, including 188 events of magnitude 3.5 to 5.8, over the hypocentral distance range from 2 km to 500 km. A generalized inversion is used to solve for regional source and attenuation parameters and station site responses, within the context of an equivalent point-source model, following the method of Atkinson et al. (2015) and Yenier and Atkinson (2015a,b). The resolved parameters include the regional geometric spreading and anelastic attenuation, source parameters for each event (e.g. moment magnitude and stress parameter for a Brune point-source model), and site response terms for each station

relative to a reference site condition of NEHRP (Natural Earthquake Hazards Reduction Program) B/C site class boundary (time-averaged shear-wave velocity in the upper 30 m, V_{S30} , of 760 m/s). The parameters fully specify a regionally-calibrated GMPE that can be used to describe median horizontal-component amplitudes across the region for hazard and ShakeMap applications, and to aid in the development of traffic light protocols and other risk-mitigation tools. This GMPE is based on more ground-motion data than any previous GMPEs for induced events in North America, and utilizes a methodology designed to ensure appropriate scaling of motions over a wide range of magnitudes and distances.

3.2 Database

Digital ground-motion records from thousands of events recorded on ~1200 regional three-component broadband seismograph and accelerometer stations were obtained from IRIS (Incorporated Research Institutes for Seismology), from publicly accessible networks across Oklahoma, Texas, Arkansas, Colorado, Missouri and New Mexico (see Data and Resources). The downloaded records were processed and compiled to produce a ground-motion database of peak ground acceleration (PGA), peak ground velocity (PGV), and 5%-damped pseudo-acceleration response spectra (PSA); PSA are sampled at 30 log-spaced frequencies from 0.20 to 50.0 Hz. For this study, we analyzed events of $M \geq 3.5$ at hypocentral distances (R_{hypo}) from 2 km to 500 km; Figure 3.1 is a map of the selected events and stations. The GMPE is based on the geometric mean of the horizontal component ground-motion amplitudes, consistent with previous studies (e.g. Yenier and Atkinson, 2015b). We note that the geometric mean is very similar to the orientation-independent horizontal-component measure used in the Next Generation Attenuation database (Boore, 2010), but more practical to calculate when doing batch processing of large numbers of records.

The compilation and processing of the database from which the records were drawn follows standard time-series analysis procedures. In brief, the records were windowed, glitches and trends were removed, the time series were filtered from 0.10 to 50.0 Hz (4th order Butterworth filter) and corrected for instrument response; the processing was done using an updated version of the ICORRECT algorithm of Assatourians and Atkinson

(2010). The signal window of 300 seconds, from which response spectra are computed, includes the P-wave, S-waves and strongest portions of the coda. This window length is typical of that used to compute response spectra for earthquakes in the range of M 3.5 to 6 at regional distances (e.g. Assatourians and Atkinson, 2010). The length of the window ensures that the entire signal is captured at all stations with automated batch processing. Moreover, we verified that the response spectral amplitudes are not sensitive to the selected window length, provided that the entire signal is captured. Acceleration time series are generated from broadband seismograph records by differentiation in the frequency domain prior to conversion back to the time domain. For the accelerometer records, the digital time series are already correctly scaled in acceleration and can be integrated to calculate velocity. The window length is long enough that it is possible that more than one event may be captured during processing. This becomes increasingly problematic when a large event is contained within the same ground motion window as a smaller event. We filter our catalog by discarding smaller events that occur within 5 minutes of a large event. Due to the large number of records processed (~6,000,000 in

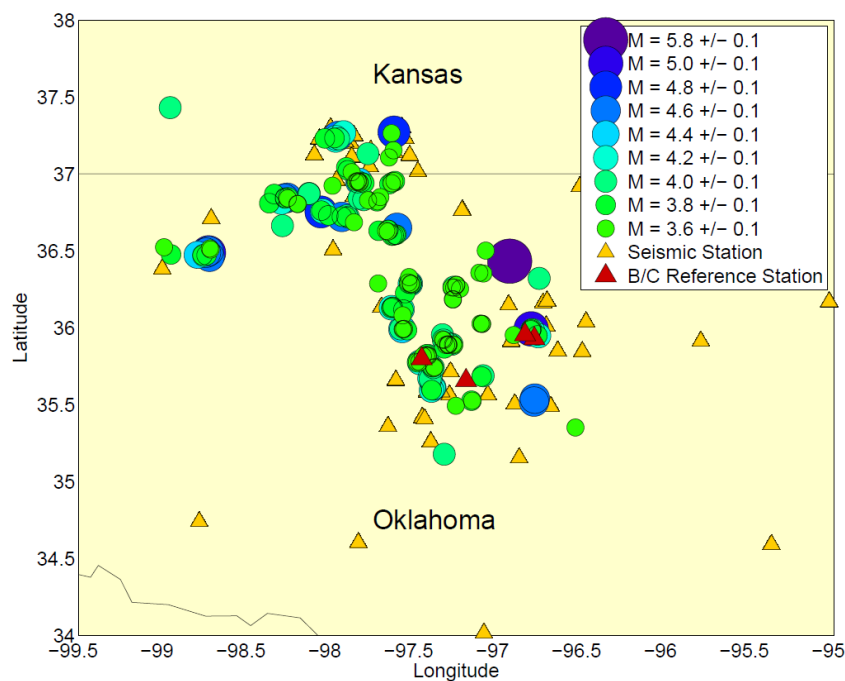


Figure 3.1 Study earthquakes (circles) and recording stations (light triangles). Stations chosen as B/C reference sites are highlighted (dark triangles).

total), there was no visual inspection of records. Thus, it is inherent that contributions from low-frequency microseismic noise within the selected passband will contribute to some degree to the spectral amplitudes, especially for small magnitudes at larger distances. However, as this ambient vibration is a real component of the signal, the PSA amplitudes accurately reflect the corresponding oscillator response to the motions. Moreover, we have limited the impact of such noise contributions through our record selection criteria. Specifically, for events of M 3.5 we impose a cut-off distance of 150 km, with this cut-off distance growing steadily to 500 km for $M \geq 4$. Figure 3.2 shows the distribution of the selected database in magnitude and distance. PGA and PGV values are computed from the absolute maximum amplitude of the corresponding time

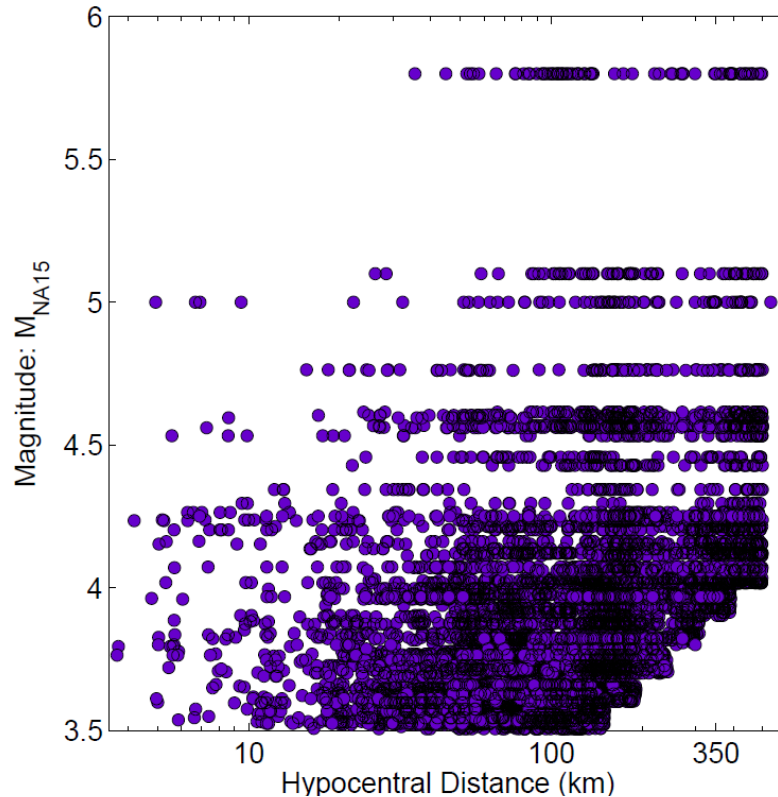


Figure 3.2 The magnitude distance distribution of the database, containing 7278 records from 194 earthquakes (M 3-5.8) recorded on 101 seismograph stations. We consider records within logarithmically spaced bins with a cut-off distance that increases from 150 km for $M = 3.5$ to 500 km for $M \geq 4.0$ events. The moment magnitude values (M_{NA15}) are determined as described in Figure 3.3.

series, whilst PSA amplitudes for the selected 30 frequencies from 0.20 Hz to 50.0 Hz are calculated from the corrected acceleration time series using the Nigam and Jennings (1969) algorithm. The selected database for analysis includes 188 events at 101 stations, for a total of 7278 records.

3.3 Estimation of Moment Magnitude

We estimate moment magnitude for each event using a slight modification of the method outlined in Novakovic and Atkinson (2015), which is based on spectral amplitude for the low-frequency end of the spectrum:

$$\mathbf{M} = \frac{\log_{10}(\text{PSA}_F) + \text{MC}_F + 1.3 \log_{10}(\text{R}_{hypo}) + \gamma_F \text{R}_{hypo}}{1.45} \quad (3.1)$$

where Equation (3.1) is evaluated using PSA_F at three frequencies: 0.3, 1.00, and 3.33 Hz. The calibration factor MC_F levels the equation whilst the anelastic attenuation coefficient γ_F removes regional attenuation trends with distance. These parameters and their values are adjusted for the Oklahoma region and are as listed in Table A3.1. Density of network coverage in Oklahoma allows for the magnitude estimate to be reliably computed from the recorded PSA at the five closest stations (distances < 50 km in Oklahoma). The algorithm is based on the amplitudes recorded by the vertical-component to minimize the effects of site response (Novakovic and Atkinson, 2015).

There are two modifications to the Novakovic and Atkinson (2015) algorithm. The first is that we use an event-adjusted attenuation model to ensure that there will be no significant distance dependence in the residuals, testing three alternative values for γ_F to consider: low (e.g. Central and Eastern North America (CENA)), high (e.g. California) or intermediate anelastic attenuation rates. The CENA and California values of the attenuation coefficient are as given in Novakovic and Atkinson (2015), whilst the intermediate model is the geometric mean of the two values. The attenuation rate that minimizes the standard deviation of the residuals is selected for each event. C_F is a fixed frequency-dependent constant that matches the level of amplitudes and is not influenced by the choice of attenuation rate. The second modification is that we calculate \mathbf{M} at each

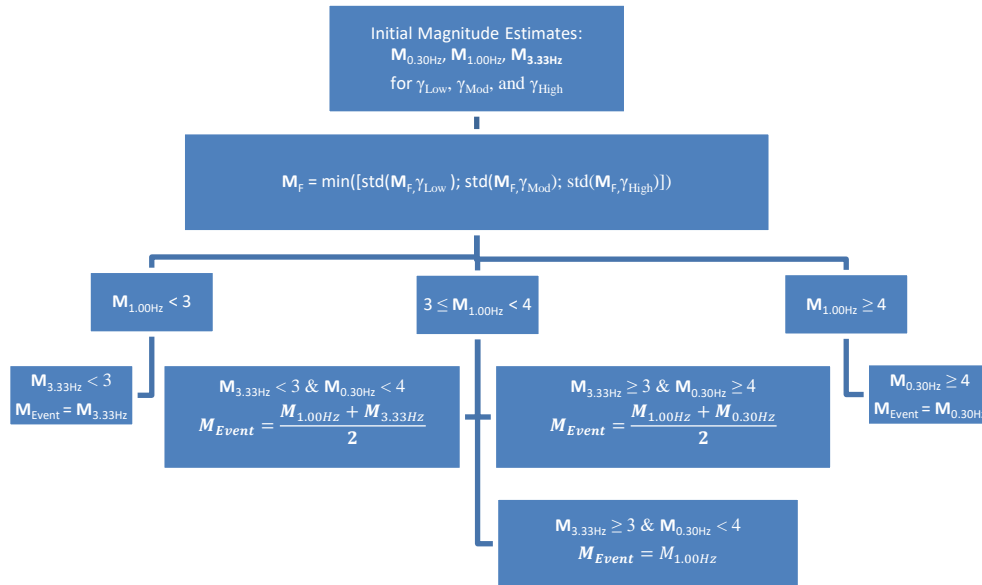


Figure 3.3: The decision tree used to decide which frequency is used to estimate moment magnitude (M) of the event. We compute M_F based on PSA at 0.30 Hz, 1.00 Hz and 3.33 Hz. The M estimate from 3.33 Hz PSA is used for events of $M < 3$, 1.00 Hz estimate for M 3 - 4, and 0.30 Hz for $M \geq 4$. For each event, the anelastic attenuation coefficient that minimizes the residuals is chosen, where three values are considered: low (CENA value), high (California value) or moderate (average of the two).

of three frequencies (0.30 Hz, 1.00 Hz, and 3.33 Hz), allowing improved accuracy of estimation according to the magnitude of the event. This is a matter of balancing the opposing considerations of noise and corner frequency. Specifically, we need to use a frequency that is low enough to be below the corner frequency for the event magnitude, so that we are measuring the low-frequency end of the spectrum. On the other hand, low frequencies are increasingly contaminated by microseismic noise, which is an important consideration for small events.

Considering these factors, PSA at 0.30 Hz provides the best estimate for larger events ($M > 4$), whilst PSA at 3.33 Hz is a good choice for small events ($M < 3$). For events of intermediate magnitude, PSA at 1.00 Hz is the optimal choice. We take the estimated magnitude from 3.33 Hz, 1.00 Hz, and 0.30 Hz PSA observations and use these values to determine the best magnitude estimate according to magnitude range, as illustrated in

Figure 3.4 (see also Novakovic and Atkinson, 2015). For example, if both $M_{3.33 \text{ Hz}} < 3$ and $M_{1.00 \text{ Hz}} < 3$, then this is a small event and we accept $M_{3.33 \text{ Hz}}$ as the event magnitude. If not, we proceed sequentially to consider the lower-frequency estimates of magnitude. If $M_{3.33 \text{ Hz}} < 3$ and $M_{1.00 \text{ Hz}} \geq 3$, we take the mean of these two calculations as the event magnitude. If not, we check if $M_{3.33 \text{ Hz}} \geq 3$, $M_{1.00 \text{ Hz}} \geq 3$, and $M_{0.30 \text{ Hz}} < 4$, and so on as shown in the decision tree of Figure 3.3. The resulting values of M are in close agreement, being on average about 0.1 magnitude units less than those determined using regional moment tensor solutions, as illustrated in Figure 3.4. We do not think this discrepancy is significant, but readers should make note that the GMPE is based on M_{NA15} .

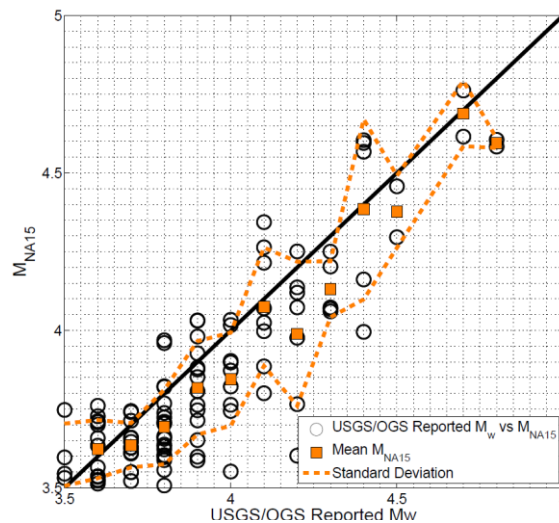


Figure 3.4: Comparison of M_{NA15} magnitude estimates with USGS/OGS reported M as obtained from regional or global moment tensors. Squares show average estimated M for events in 0.1 magnitude unit bins, along with standard deviation (dashed lines). Mean deviation from other estimates is about -0.1 units.

3.4 Ground-Motion Model

The descriptive variables for the GMPE are moment magnitude, hypocentral distance (R_{hypo}), and station-specific site response. Following the approach of Atkinson et al. (2015) we use a generalized inversion (Andrews, 1986) to solve for site response, regional source and attenuation parameters of the generic form:

$$\ln(Y) = F_E + F_Z + F_S + F_\gamma + C \quad (3.2)$$

where $\ln(Y)$ is the natural logarithm of PSA at a selected frequency. F_E , F_Z , F_S , and F_γ are the earthquake source term, geometric spreading function, site response term, and the anelastic attenuation term, respectively. Residual differences between simulations and empirical data are accounted for by the empirical calibration factor, C . The terms are each based on the generic GMPE of Yenier and Atkinson (2015b) and express the components of a stochastic equivalent point-source model (e.g. Boore, 2003). The idea of this formulation is that the basic scaling of the model in magnitude, distance and frequency content is constrained to follow seismological scaling principles, but the parameter values representing the Brune (1970, 1971) stress, attenuation and site response are calibrated by regional observations. The components are summarized in the following; see Yenier and Atkinson (2015b) for more details.

The effects of magnitude and stress parameter on ground-motion amplitudes are described by the earthquake source function F_E , adopted from the reference model developed by Yenier and Atkinson (2015a), which was based on equivalent point-source simulations calibrated to the Next Generation Attenuation (NGA)-East and NGA-West 2 databases. The implicit assumption is that the general magnitude-scaling characteristics of ground motions are not region specific (e.g. Ambraseys & Douglas, 2004; Atkinson and Morrison, 2009); this is a benefit to using this GMPE approach, as it ensures that a model calibrated using data from moderate magnitudes will scale appropriately to larger magnitudes. The source function is given as:

$$F_E = F_{\Delta\sigma} + F_M \quad (3.3)$$

For a specified reference stress ($\Delta\sigma=100$ bar), near-surface attenuation ($\kappa_0=0.025$), and site condition (B/C), F_M represents the magnitude effect on ground motion amplitudes that would be observed at the source if there were no near-distance saturation effects.

The F_M term is a hinged quadratic function of moment magnitude

$$F_M = \begin{cases} e_0 + e_1(M - M_H) + e_2(M - M_H)^2 & M \leq M_H \\ e_0 + e_3(M - M_H) & M > M_H \end{cases} \quad (3.4)$$

where frequency dependent coefficients, e_0 to e_3 , and the hinge magnitude \mathbf{M}_H were determined by Yenier and Atkinson (2015b) using stochastic equivalent point-source simulations. The stress adjustment term $F_{\Delta\sigma}$ is needed when $\Delta\sigma$ is different than 100 bars and is defined as

$$F_{\Delta\sigma} = e_{\Delta\sigma} \ln(\Delta\sigma/100) \quad (3.5)$$

where the rate of ground motion scaling with $\Delta\sigma$ is described by $e_{\Delta\sigma}$. Equation 3.5 provides the relationship between stress parameter and response spectral amplitudes allowing the determination of $\Delta\sigma$ from PSA observations. Its form is given by:

$$e_{\Delta\sigma} = \begin{cases} s_0 + s_1 \mathbf{M} + s_2 \mathbf{M}^2 + s_3 \mathbf{M}^3 + s_4 \mathbf{M}^4 & \Delta\sigma \leq 100 \text{ bar} \\ s_5 + s_6 \mathbf{M} + s_7 \mathbf{M}^2 + s_8 \mathbf{M}^3 + s_9 \mathbf{M}^4 & \Delta\sigma < 100 \text{ bar} \end{cases} \quad (3.6)$$

where s_0 to s_9 are frequency dependent coefficients.

We use a trilinear geometric spreading function F_Z . This is a modification to the bilinear form used by Yenier and Atkinson (2015a,b) and Yenier et al. (2017). The modification is made to accommodate a flat transition zone from direct-wave to surface-wave spreading. The trilinear function better reflects the strong influence of the Moho (Mohorivicic) bounce effects (Burger et al., 1987) that are observed in the region. The Mohorivicic discontinuity varies in depth from 32 to 42 km in the northeastern and central parts of Oklahoma and is as deep as 50 km towards the southwest (Taves, 2013). Spatial variations of Moho depth in the region can explain the broad range over which these bounce effects are observed; this will be seen clearly in the subsequent analyses and figures. F_Z is a function of R_{hypo} , \mathbf{M} , and transition distances R_t :

$$F_Z = \ln(Z) + (b_3 + b_4 * \mathbf{M}) \ln\left(\frac{R}{R_{\text{ref}}}\right) \quad (3.7)$$

$$R = \sqrt{R_{hypo}^2 + h_{eff}^2},$$

$$h_{eff} = 10^{(-0.405+0.235M)},$$

$$R_{ref} = \sqrt{1^2 + h_{eff}^2}$$

$$\mathbf{Z} = \begin{cases} R^{-1.3} & \text{for } R \leq R_{t_1} \\ R_{t_1}^{-1.3} \left(\frac{R}{R_{t_1}}\right)^{-0.05} & \text{for } R_{t_1} < R \leq R_{t_2} \\ R_{t_1}^{-1.3} \left(\frac{R_{t_2}}{R_{t_1}}\right)^{-0.05} \left(\frac{R}{R_{t_2}}\right)^{-0.5} & \text{for } R_{t_2} < R \end{cases}$$

We assume R_{hypo} is equal to the closest distance to the fault rupture for the small to moderate events of this study. The coefficient h_{eff} is the magnitude-dependent pseudo-depth term introduced to account for close-distance saturation effects due to finite-fault effects. An implicit assumption is that finite-fault effects in all regions will influence near-distance saturation effects in a similar way (Yenier and Atkinson, 2014). The finite-source model is employed to allow predictions from point-source models to mimic finite-fault effects by placing the point at an equivalent overall distance, such that the closest distance motions saturate appropriately (Atkinson and Silva, 2000; Boore, 2009; Yenier and Atkinson, 2014). The saturation effect is a function of magnitude ensuring the appropriate scaling of moderate to larger earthquakes (M3-7.5) near the source (Yenier and Atkinson 2015). The coefficients b_3 and b_4 account for the change in apparent attenuation that occurs when ground motions are modeled in the response spectral domain rather than the Fourier domain (Yenier and Atkinson, 2015a).

To define the shape of the trilinear form, we first removed the estimated anelastic attenuation coefficients for CENA, and the magnitude scaling assuming a stress parameter of 100 bars, all as given in Yenier and Atkinson (2015b). At each frequency

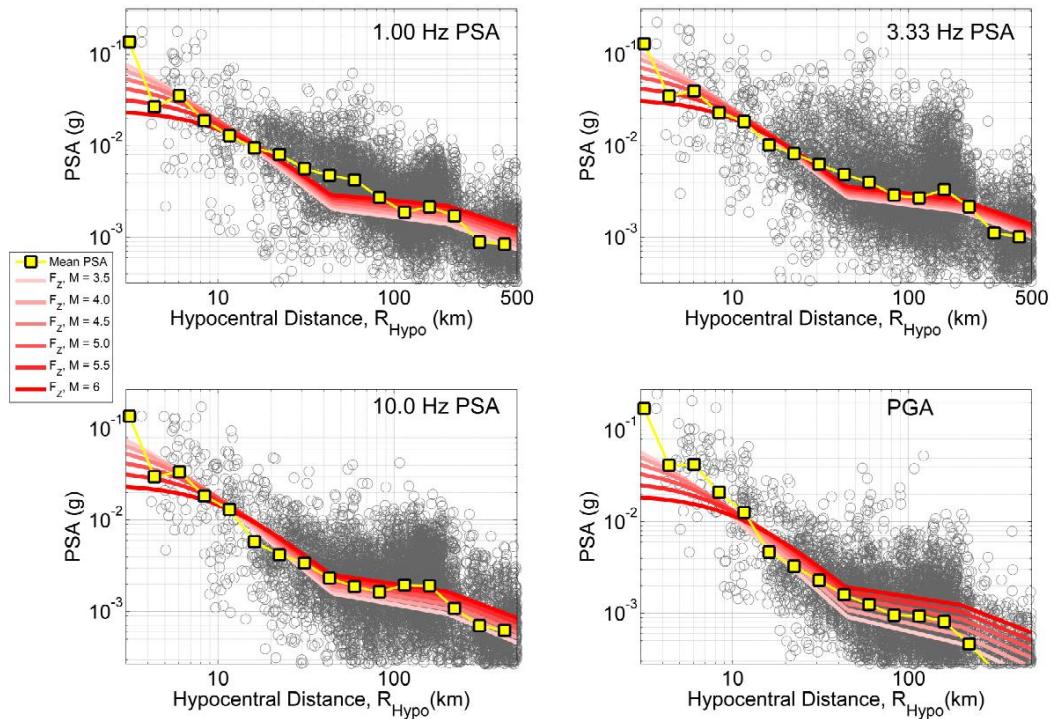


Figure 3.5: Observed normalized amplitudes (circles) after correction for magnitude dependence (F_M , Eqn 3.4) and CENA anelastic attenuation (Eqn 3.8); squares show median normalized amplitudes in distance bins. Solid lines show the adopted trilinear geometric spreading function (which has magnitude dependence as in YA15), for a range of magnitudes, assuming a 100-bar stress parameter; only the shape is important, as the level is determined by inversion. A constant is added to all ground motions to adjust the level of the geometric spreading function for better visualization.

we plotted the residual ground motion trends against hypocentral distance. We then chose the model parameters that broadly match the shape across all frequencies. This suggested that a trilinear geometric spreading function was required, with slopes -1.3, -0.05 and -0.5, and transition distances of 45 km and 200 km for R_{t1} and R_{t2} , respectively. Figure 3.5 depicts the adopted trilinear model shape in comparison to normalized PSA values, where the PSA values are normalized by removing the magnitude scaling and anelastic attenuation terms (e.g. Eqns 3.4 and 3.8). A value of 100 bars is assumed in calculation of the magnitude-scaling term for the normalization. We have adopted a frequency-independent geometric spreading model, with all frequency-dependent effects

being carried by the anelastic attenuation coefficients. This modeling choice is consistent with nearly all previous stochastic models of ground motion (e.g. see Yenier and Atkinson, 2015a/b; Boore, 2003; Atkinson and Boore, 2006). We acknowledge that this conceptually-simple model may not be entirely accurate, but it strikes a reasonable balance between modeling the most important effects whilst maintaining simplicity and appears to allow a reasonable approximation to the observed shapes of the amplitude decay function as seen on Figure 3.5.

With the geometric spreading model constrained, all remaining coefficients can be determined by inversion, as in Atkinson et al. (2015). We determine the regional anelastic attenuation function F_γ in the inversion process:

$$F_\gamma = \gamma R_{\text{hypo}} \quad (3.8)$$

where γ is a frequency-dependent anelastic attenuation coefficient. Yenier and Atkinson (2015b) determined γ values for CENA and for California using the NGA-East and NGA-West 2 databases, respectively. In this study, we determine the anelastic coefficient for each frequency from the Oklahoma database in the inversion.

The station terms F_S are expressed relative to a reference NEHRP site condition. Stations location on B/C sites with time-averaged shear-wave velocity in the top 30 m (V_{s30}) of ~ 760 m/s are chosen as the reference sites, with respect to which all other site responses will be determined. Four stations on sandstone or shale with $V_{s30} \sim 760$ m/s are selected as reference sites: OK029, OK030, OK031, and OK005 (highlighted on Figure 3.1). Their selection was guided by a combination of surficial geology information (USGS National Geologic Map Database) and V_{s30} studies (EPRI, 2013a, see Data and Resources). The reference sites have well-behaved horizontal-to-vertical component ratios that are broadly similar to each other and consistent with those expected for B/C sites based on other studies (e.g. Ghofrani and Atkinson, 2014). We assume that the average site amplification over these stations at each frequency is zero. This constraint, when applied in the inversion, calibrates the GMPE for an average B/C site condition, provided these are typical B/C sites. Thus, all site terms will be relative to the average

site amplification for the six reference sites. Note that any differences between the actual amplification of the six sites (on average) and that assumed for B/C sites in the underlying generic GMPE of Yenier and Atkinson (2015b), will be cast into the calibration constant (C) by the inversion.

3.5 Application to Induced Events in Oklahoma

The database for the inversion to Equation (3.2) contains 7278 records from 188 $M \geq 3.5$ events at 101 stations, as shown in Figure 3.2. The record set was further filtered to ensure that each analyzed event is recorded on at least five stations, and that each station records at least 15 events. This allows robust determination of source, site and event terms. We take the geometric mean of the two horizontal-component PSA values in units of g, for 30 logarithmically spaced frequencies from 0.20 Hz to 50.0 Hz, PGA, and PGV.

To facilitate inversion, the fixed geometric spreading function and magnitude scaling terms from Equation (3.2) are subtracted from the observed ground motion values:

$$\ln(Y_{ij}) - F_{M,i} - F_{Z,i j} = E_i + F_{S,j} + \gamma R_{\text{hypo } ij} \quad (3.9)$$

where Y_{ij} is the ground-motion parameter for event i and station j . $F_{M,i}$, $F_{Z,i j}$, are the magnitude scaling term and geometric spreading term for event i and station j , as calculated given the known M and distance $R_{\text{hypo } ij}$. Note that the stress parameter function ($F_{\Delta\sigma}$) and the empirical calibration factor (C) are implicitly included in the event term, E_i . $F_{S,j}$ is the site amplification term relative to the reference B/C site condition at station j . γ is the regional anelastic attenuation term.

The unknown terms in Equation (3.9) are obtained, for PSA values at 30 equally logarithmically spaced frequencies from 0.20 Hz to 50.0 Hz, PGA, and PGV, using the generalized inversion scheme of Andrews (1986). Figure 3.6 shows the resulting anelastic attenuation term as a function of frequency. These values indicate weaker attenuation in comparison to previous studies for CENA at frequencies greater than 2.00

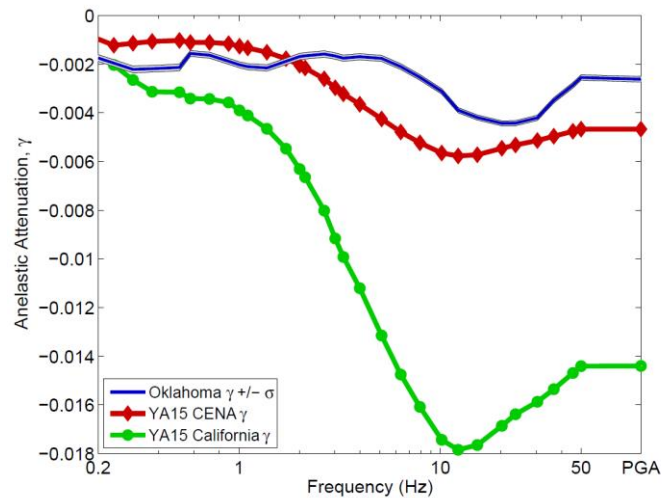


Figure 3.6: Regional anelastic attenuation term for Oklahoma with standard deviation, in comparison to previous results of Yenier and Atkinson (2015b) for California and CENA.

Hz; at lower frequencies the attenuation in Oklahoma appears to be stronger than what is typically observed in CENA, but less than that observed in California.

The site amplification term ($F_{s,j}$) is obtained for each of the 101 stations, relative to the assumed reference site condition of B/C, as represented by the average over the six selected reference sites. These site amplification terms can be subtracted from the observations to level all records to the same reference site condition. The site amplification terms for all stations are given in Table S3.1, available in the electronic supplement. Figure 3.7 shows the site amplification functions for the reference stations. Note that by definition the average of these six functions is zero (in ln units) as a condition applied as an inversion constraint. Figure 3.8 plots a sample of typical site response functions for non-reference stations, most of which are softer than B/C. As expected, the peak amplifications for softer sites are significantly larger than those for the reference sites, often exceeding a factor of four at some frequencies. Figure 3.9 plots all site response functions retrieved from the inversion along with their mean and standard deviation. It is interesting that the average over all sites is near zero, as this is not necessarily expected. The regression is constrained such that the mean amplification of the reference B/C stations should be zero, but there is no such constraint on the average

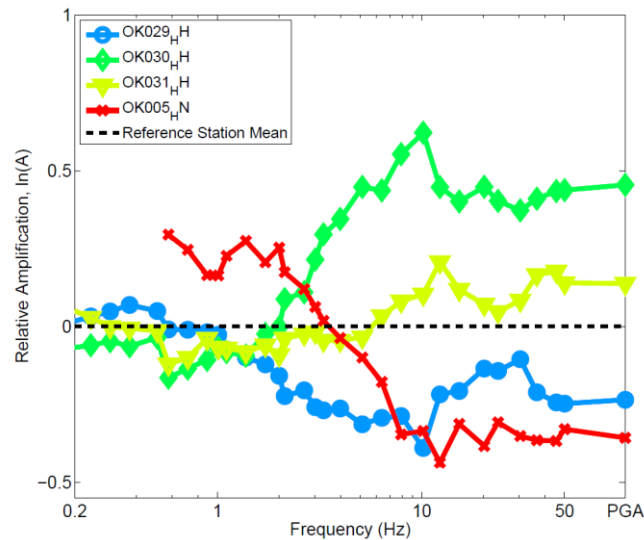


Figure 3.1: Site amplification (ln units) for the assigned reference B/C stations, resulting from the inversion. OK005 sits on shale with V_{s30} of 613 m/s. OK029 sits on sandstone, OK030 and OK031 both sit on shale. V_{s30} for OK029, OK030 and OK031 believed to be close to B/C based on horizontal-to-vertical component ratios.

of the other stations relative to the reference level. This near-zero average relative to B/C results from some sites having pronounced amplifications (Class C, D, & E) and others having pronounced de-amplification (Class A & B), relative to B/C. Moreover, individual sites often have strong amplification at a specific peak frequency (Hassani and Atkinson, 2016), and these effects average out over many sites. Thus, the near-zero average of site effects relative to B/C should not be taken to mean that site amplifications are not important; specifically, it can be seen in Figure 3.9 that peak site amplifications of >0.7 ln units (a factor of 2) are fairly common in the frequency range from 2.00 to 8.00 Hz.

The event term (E_i) determined by the inversion includes the event-specific stress adjustment factor for each event, as well as the regional calibration factor. Boore et al (2010) showed that a common approach of determining the stress parameter by matching amplitudes at high frequencies for the known moment magnitude can lead to non-uniqueness in $\Delta\sigma$ values, due to the tradeoff between the earthquake source and attenuation parameters. Yenier and Atkinson (2015b) chose to solve this problem by

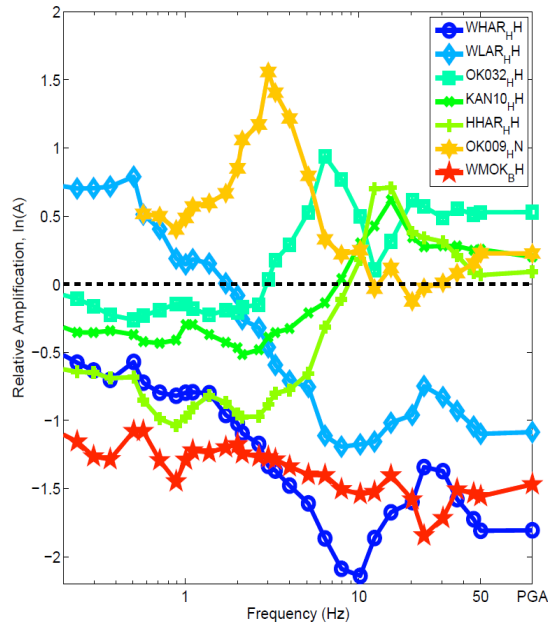


Figure 3.2: Typical site amplifications (ln units) for stations resulting from the inversion. WHAR is a sandstone station with V_{s30} of 1403 m/s. WMOK is a station sitting on granite with V_{s30} 1859 m/s. OK009 is a station sitting on conglomerate with V_{s30} of 322 m/s. No V_{s30} information is available for WLAR, OK032, KAN10 and HHAR; however according to surficial lithology maps, these stations sit on sandstone, alluvium, gravel and limestone respectively

basing the stress parameter value on the corner frequency (spectral shape), and by using a calibration constant to reconcile the overall spectral amplitude levels. In this study, we took an approach that is similar to that of Yenier and Atkinson (2015b), but results in a more stable determination of the stress parameter for cases where the source spectrum does not nicely follow the ideal Brune-model spectral shape. We base the determination of the stress parameter on the event's average high-frequency spectral level, as represented by PSA at 10.0 Hz, relative to that expected based on the seismic moment (implicitly including any offset in amplitude level at the moment-end of the spectrum). To avoid complications of near-distance saturation effects, the event spectrum for this purpose is evaluated at a reference distance of 20 km, using the attenuation function from the inversion to correct observations to the reference distance of 20 km (and then averaging over all stations for each event). Figure 3.10 is a graphical illustration of the

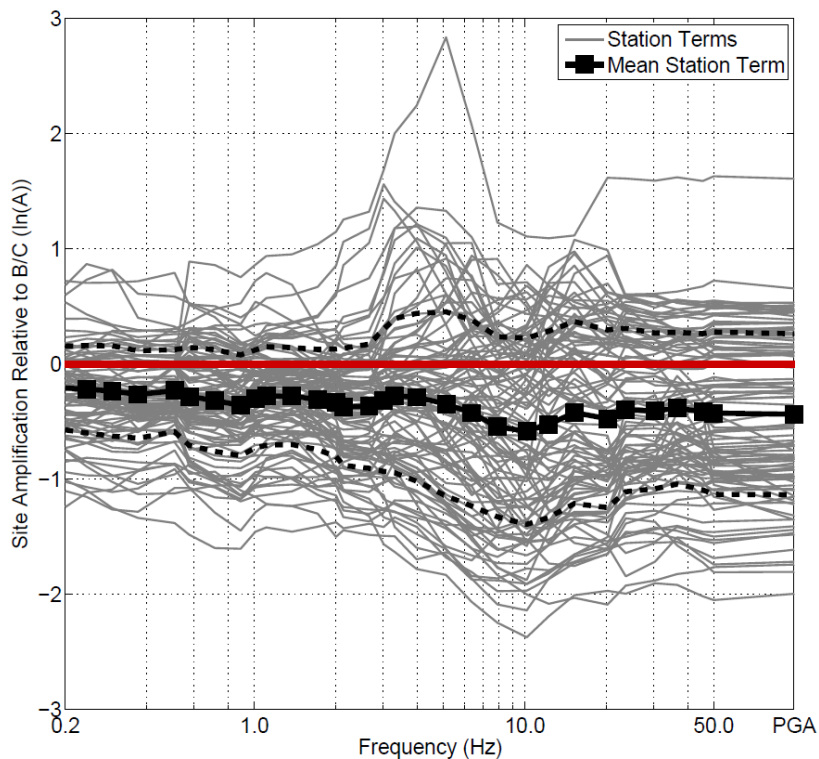


Figure 3.3 All station terms. The lines depict the site response relative to B/C condition for all stations used in the study in natural log units. Squares depict the mean site term for each frequency, with their standard deviations in dashed lines.

approach taken. We use the average event spectrum at 20 km to first find the offset of the long-period SD (spectral displacement) level at 1.00 Hz from that expected for the given seismic moment for the event, in ln units (ΔLF), for an ideal 100-bar Brune model spectrum, as defined by Yenier and Atkinson (2015b). We remove the ΔLF offset from the average event spectrum, so that it now matches the level for an ideal Brune spectrum of that moment magnitude, at low frequencies. The amount by which the 10.0 Hz-PSA value of this amplitude-corrected spectrum differs from that expected for a 100-bar Brune-model spectrum is taken as a measure of the stress parameter. Higher values of stress result in larger values of 10.0 Hz-PSA, relative to the 100-bar model, whereas lower stress results in lower 10.0 Hz-PSA values. Note this is similar to the shape-based approach of Yenier and Atkinson (2015b) but focuses on the high-frequency spectral level relative to the low-frequency level, instead of focusing on the corner frequency.

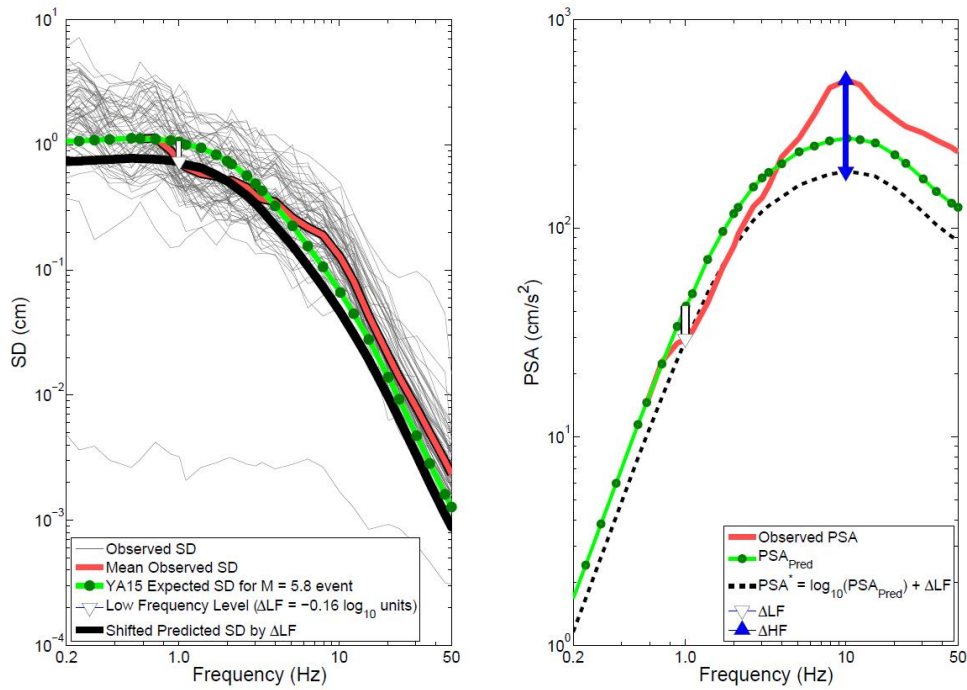


Figure 3.4: Determination of stress parameter, for M5.8 Pawnee event. Left) ΔLF (low-frequency offset) is determined as the offset of the average of observed spectral displacement (SD) on the seismic moment end of the spectrum (1.00 Hz) relative to predicted SD from YA15 (corrected for site and attenuation effects to a reference distance of 20 km). Right) ΔHF (high-frequency offset) is determined from the level of the 10.0 Hz PSA, after shifting spectrum by ΔLF . Note that the spectra in this figure have been converted from units of g to cm/s^2 .

For ease of application in implementing this approach, the generic GMPE of Yenier and Atkinson (2015b) was evaluated at 20 km for multiple combinations of magnitude and stress parameter, and used to define the relationship between 10.0 Hz PSA and stress parameter:

$$\log_{10}(\Delta\sigma) = 2.024 + 1.52(\log_{10}(PSA_{10\text{ Hz,event}}) - (\log_{10}(PSA_{10\text{ Hz,100bar}}) + \Delta LF)) * \max(1, 1.3 \left(\frac{3.5}{M}\right)) \quad (3.10)$$

where $PSA_{10\text{ Hz,event}}$ is the average 10.0 Hz PSA value for the event, adjusting for site and path effects to the reference distance of 20 km, and $PSA_{10\text{ Hz},100\text{ bar}}$ is the corresponding 10.0 Hz PSA that is predicted for a Brune stress parameter of 100 bar at 20 km. This parameterization makes it easy to back-calculate the stress parameter from the 10 Hz value of the event spectrum at 20 km. The basic idea is that we are using the high-frequency spectral level to infer the corner frequency, instead of using the corner frequency to infer the high frequency level (as was done in Yenier and Atkinson 2015b). We took this approach because we determined it was more stable, leading to a lower standard deviation of determined stress parameters.

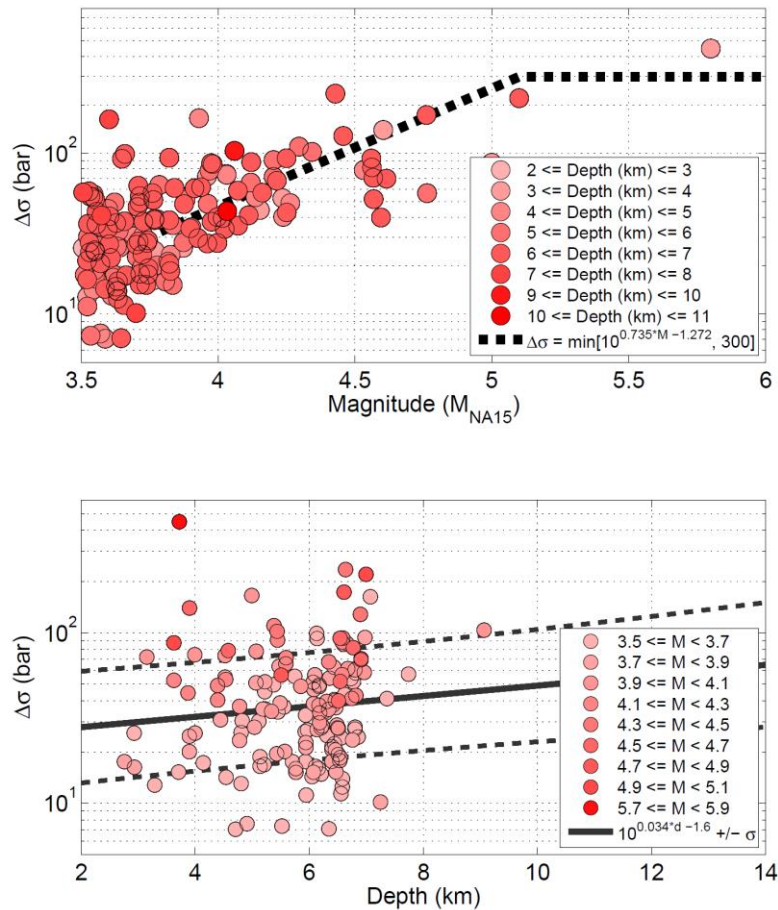


Figure 3.5: Stress parameters for individual events (circles), compared with a with simple bilinear fit to the stress parameter versus magnitude (upper as a dashed line) and a simple fit to the stress parameter with respect to focal depth (lower as a solid line).

Stress parameter values for all events are given in Table S3.2 of the electronic supplement; a summary of stress parameters for events of $M > 4.2$ is provided in Table A3.2. The stress parameter increases with magnitude for small shallow events, as observed in previous studies for CENA events, and their values fall within the expected range (Yenier and Atkinson 2015b). Stress parameter values typically range from 40 to 500 bars and are observed for events of $M > 4$. We note that the catalog depths for the events (Table S3.2) are predominantly in the range from 3 to 8 km; this table reflects updated location and depth estimates from the double-difference relocation results from Schoenball and Ellsworth (2017) where available. More than 140 events in this study had depths that were double difference relocated and have uncertainties from 0.3 to 1 km in the vertical direction (Schoenball and Ellsworth, 2017). We plot stress parameter as a function of magnitude and depth in Figure 3.11; it is apparent that trends in both variables are present, though the trends in depth are not well-resolved due to the

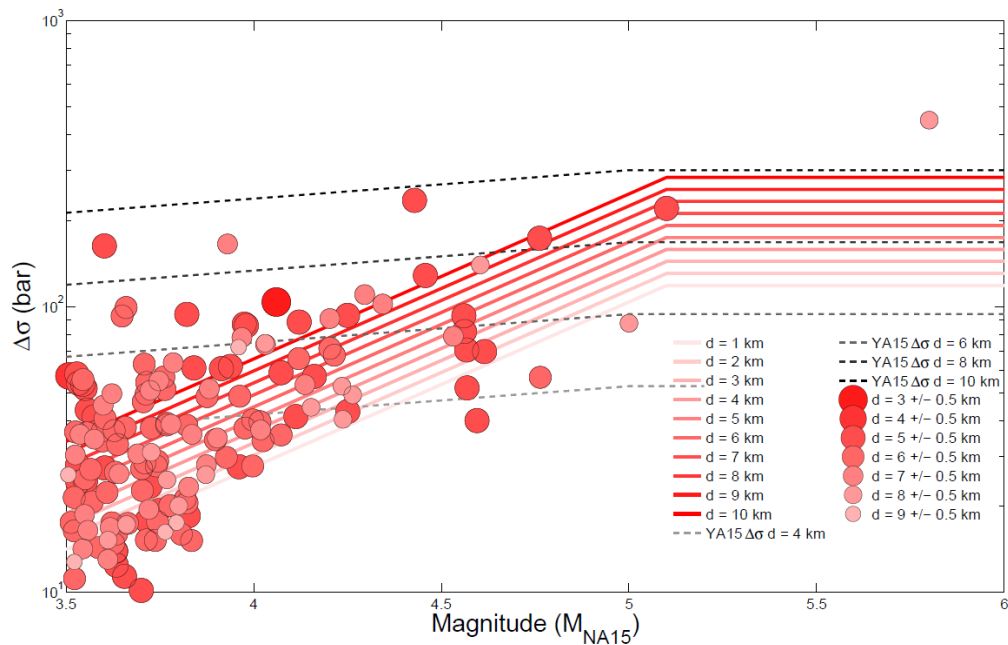


Figure 3.6 Stress parameters determined by inversion for each event (Figure 3.8) (circles) as a function of moment magnitude (M_{NA15}) and depth (larger circles denote greater depth). Solid lines show models that capture the observed trends in the Oklahoma data, in comparison to YA15 CENA model (dashed lines) for several values of focal depth.

limited depth range of the data. A multivariable regression is performed to develop a regional stress model as a function of magnitude and depth using relocated events only. Figure 3.12 shows the proposed stress parameter model for induced events in this region:

$$\ln(\Delta\sigma) = 5.65 + \min[0, 0.097(d - 10)] + \min[0, 1.329(\mathbf{M} - 5.1)] \quad (3.11)$$

It has been suggested that stress increases with focal depth, and that this is the primary reason why induced events typically have a lower stress parameter than do natural tectonic earthquakes (e.g. Yenier and Atkinson, 2015b; Atkinson and Assatourians, 2017). The depth trends observed in Oklahoma appear to be weak but are not well-resolved because all events are relatively shallow; by contrast, there is a strong magnitude scaling, resulting from large high-frequency spectral amplitudes for the largest Oklahoma events. It has also been suggested that events in Central North America may have lower stress than those in Eastern North America, due to differences in focal mechanism (Huang et al., 2017; Cramer, 2017).

The regional calibration factor (C) can be determined as the average residual mismatch between the observations and the model (after considering the stress parameter for each event, the site term for each station, and the regional geometric spreading and anelastic attenuation functions). As discussed in Yenier and Atkinson (2015a) the calibration factor reflects the average differences between the observations and the simulations, including any systematic factors that are not accurate or not included in the modeling approach. Examples of such factors include any residual regional site amplification effects relative to the assumed amplification model for B/C that was included in the Yenier and Atkinson (2015b) formulation, and any surface wave or other contributions to the motion that were not included in the Brune source model. Removing the resolved parameters from the inversion from the ground motion observations, Equation 3.9 becomes

$$\ln(Y_{ij}) - F_{M,i} - F_{Z,i,j} - \gamma_{AB}R_{ij} - F_{\Delta\sigma} - F_{S,j} = C_{OK} + \eta_i + \varepsilon_{ij} \quad (3.12)$$

where C_{OK} is the regional calibration factor for Oklahoma, η_i is the between-event error, and ε_{ij} is the within-event error. Following Abrahamson and Youngs (1992), we use a mixed effects regression of residuals to solve Equation 3.12. An iterative regression is

performed to maximize the likelihood of the model and estimate the regional calibration factor (C_{OK}). The residual error of the observations with respect to the model is separated into its between-event and within event components (η_i and ε_{ij}). The regional calibration factor for Oklahoma is shown in Figure 3.13 and is summarized in Table A3.3 along with the determined error components. A full list of model parameters, calibration factor, and error components at all frequencies are given in Table S3.3 of the electronic supplement. At frequencies < 1.2 Hz we observe a positive average residual of 0.43 ln units. This might be explained by inherent limitations of stochastic methods at low frequencies, which do not allow surface wave phases or coherent pulses to be properly modeled.

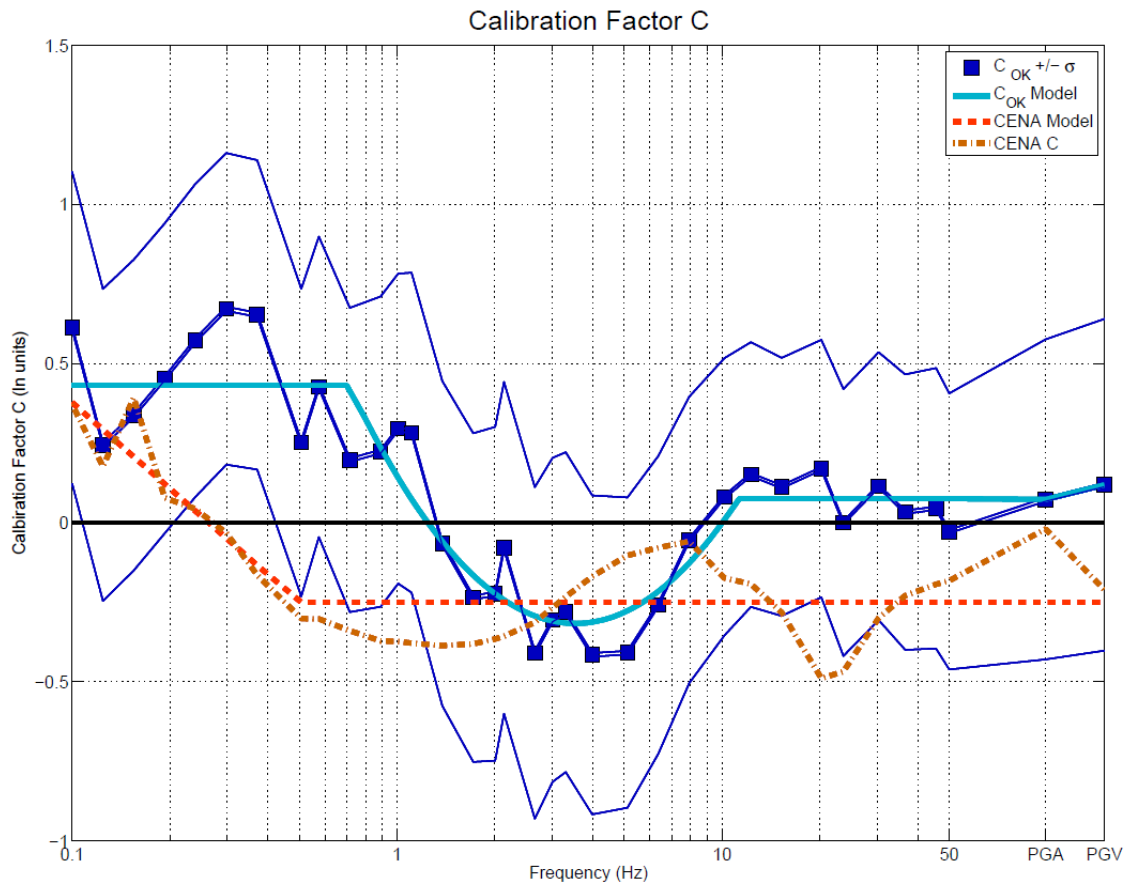


Figure 3.7: Calibration factor (C_{OK}) obtained from inversion (squares) and its standard deviation (jagged lines). The solid line shows suggested model function for C_{OK} , the Yenier and Atkinson (2015b) calibration factor for CENA is shown as a dot-dashed line, and its modeled form is shown as a dashed line.

The calibration factor dips to -0.5 ln units between 1.2 Hz and 10.0 Hz then recovers to a near-zero value at high frequencies. The calibration factor follows the average trends given by:

$$C_{OK} = \begin{cases} 0.45 & \text{for } f < 0.7 \text{ Hz} \\ 1.54(\log_{10}(f))^2 - 1.69(\log_{10}(f)) + 0.15 & \text{for } 0.7 \text{ Hz} \leq f < 11.3 \text{ Hz} \\ 0.08 & \text{for } f \geq 11.3 \text{ Hz} \end{cases} \quad (3.13)$$

The shape of the calibration function at intermediate frequencies reflect deviations from the regional site response model assumed for the reference B/C condition. The generic GMPE form upon which this study is based has embedded within it a prescribed average amplification function for B/C conditions, which was derived from an assumed model (Atkinson and Boore, 2006). Any differences between the average amplification factors for B/C sites in Oklahoma and those in the assumed embedded model will map into the calibration factor. As shown in Figure 3.14, we can interpret the inverse of the calibration factor as the amplification of the six reference sites (on average), relative to the assumed amplification function for B/C (Seyhan et al., 2014). By this logic, we may infer that the reference sites have an amplification that is slightly larger than that assumed by Yenier and Atkinson (2015b) for B/C sites, and more peaked at intermediate frequencies. An alternative explanation for the dip in the calibration constant at intermediate frequencies could be that the shape of the assumed Brune source model is not well-followed on average.

The final Oklahoma GMPE includes the assumed magnitude scaling, geometric spreading functions and anelastic attenuation terms, the derived model for the stress parameter, the site amplification terms, and the empirical calibration factor, and is described as:

$$\ln(Y_{ij}) = F_M + F_{\Delta\sigma,OK} + F_Z + F_\gamma + F_S + C_{OK} \quad (3.14)$$

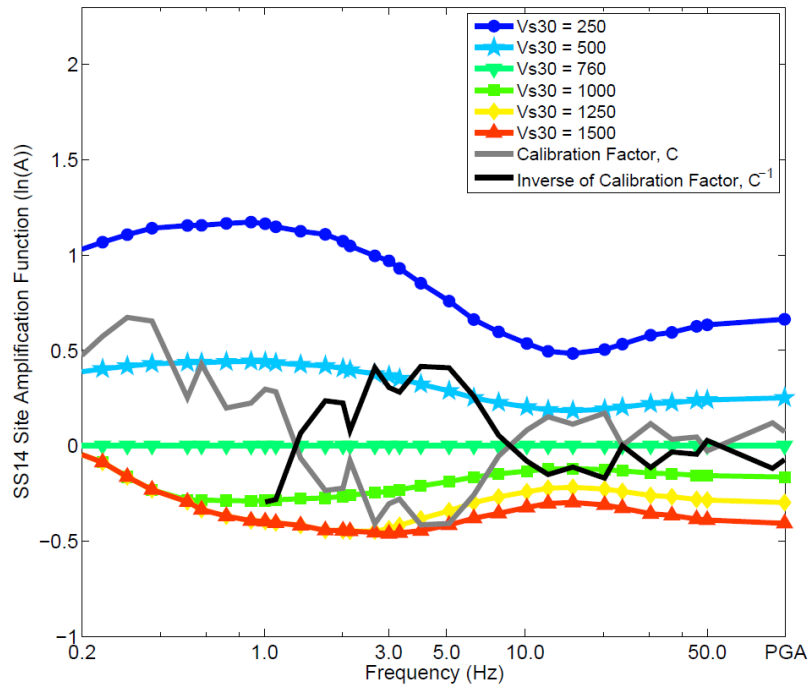


Figure 3.8 The Oklahoma calibration factor (gray line) and its inverse (black line), in comparison to the site amplification functions of Seyhan and Stewart (2014; SS14) for California, for a range of V_{s30} values (lines with symbols). It should be noted that the site amplification function is at a constant level for V_{s30} greater than 1500 m/s.

where the coefficients for all terms are summarized in Table A3.3 and fully listed in Table S3.3 of the electronic supplement. The error terms (η_i and ε_{ij}) are normally distributed in natural logarithmic units and have standard deviations of τ and ϕ respectively. The combined ground motion variability resulting from event-specific factors, such as the randomness in the source process, that have not been included in the predictive model can be expressed by the between-event variability, τ . Record specific factors such as the randomness in the site amplification for a given site class, or azimuthal directivity effects that are not considered are mapped into the within event variability, ϕ . The between-event and within-event variability have similar levels, though the between-event variability is generally lower; which is a common feature of empirical

GMPE derivation (Strasser et al., 2009). The total standard deviation (σ) of equation 3.14 can be described as

$$\sigma = \sqrt{\tau^2 + \varphi^2} \quad (3.15)$$

where the value of sigma is typically in the range of 0.57 to 0.69 natural logarithmic units. Figure 3.15 shows between event residuals as a function of depth binned by magnitude. In Figures 3.16 through 3.19 we plot the within-event residuals (Residual = $\ln(\text{PSA}_{\text{Observation}}) - \ln(\text{PSA}_{\text{Predicted}})$) for the horizontal-component (geometric mean) PSA at 1.01 Hz, 5.12 Hz, 10.2 Hz, and PGA as a function of hypocentral distance, binned by magnitude. There are no significant trends in the residuals in magnitude or distance for hypocentral distances greater than 10 km; at closer distances, there is a tendency towards slightly positive residuals at some frequencies, and slightly negative at others. Figure 3.20 demonstrates the final GMPE (for PSA at 5 Hz), overlaying site-corrected observations. As expected from the residual plots, observations fit well to the GMPE.

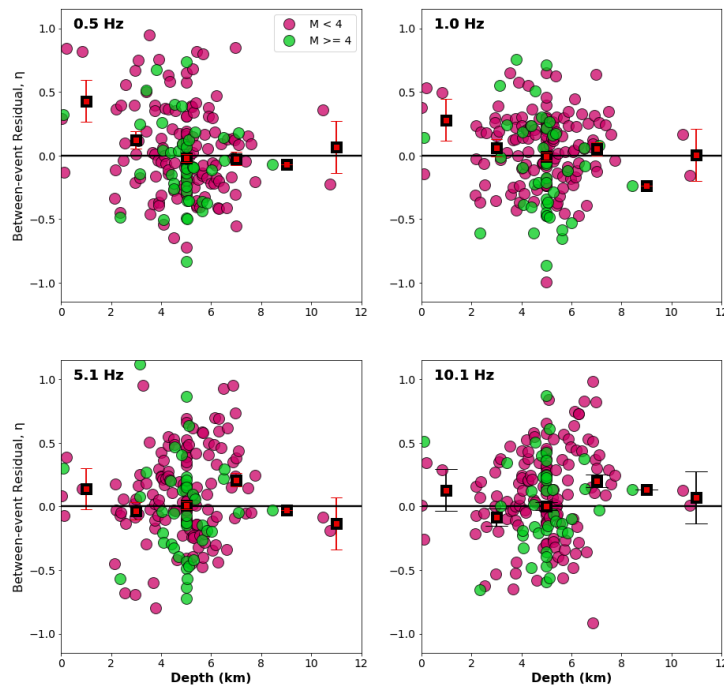


Figure 3.15: Between-event residuals η , where dark (pink) circles show $M < 4$, light circles (green) show $M \geq 4$, and squares show the depth bin mean $\pm \sigma$.

In Figure 3.21, we compare the GMPE for induced events in Oklahoma, at selected frequencies, to the CENA GMPE of Yenier and Atkinson (2015b) for earthquakes at shallow depths of 5, 6, and 8 km (the typical earthquake depths in Oklahoma), for events of M 4, 5, and 6, respectively. The GMPE of Atkinson (2015), which was derived from moderate events with an average depth of 9 km in California (NGA-West2 database), but postulated to apply for induced events in CENA, is also shown. The trilinear geometric spreading function used in this study results in higher predicted ground motions at larger hypocentral distances in comparison to the Yenier and Atkinson (2015b) or Atkinson (2015) model. At high frequencies ($f > 3$ Hz), the amplitudes for relatively small events ($M \sim 4$) in the GMPE from this study are similar to those of previous studies (e.g. Yenier and Atkinson, 2015b). At lower frequencies, Oklahoma amplitudes tend to be higher, likely reflecting amplification effects due to regional geology. For events of M 5 to 6, Oklahoma amplitudes tend to be larger than those in the Yenier and Atkinson (2015b) model, reflecting the differences in magnitude and depth dependence of the stress parameter.

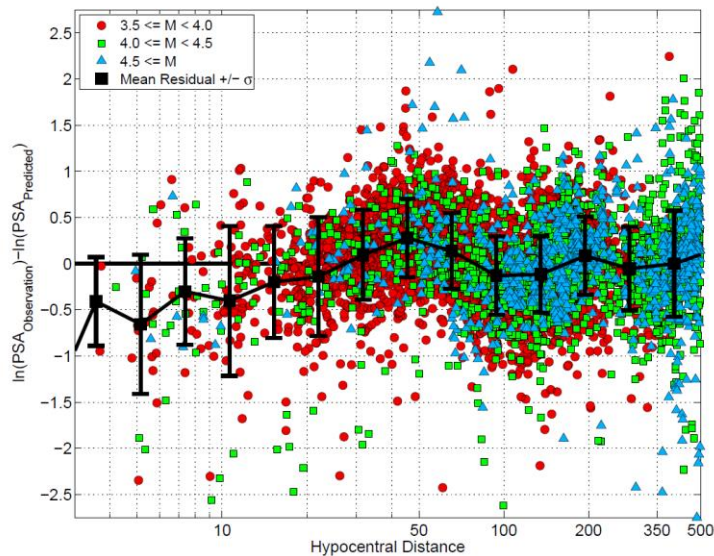


Figure 3.9 Within event residuals with respect to the final GMPE for PSA at 1.01 Hz. Black squares depict the mean residual and its standard deviation in logarithmically spaced distance bins.

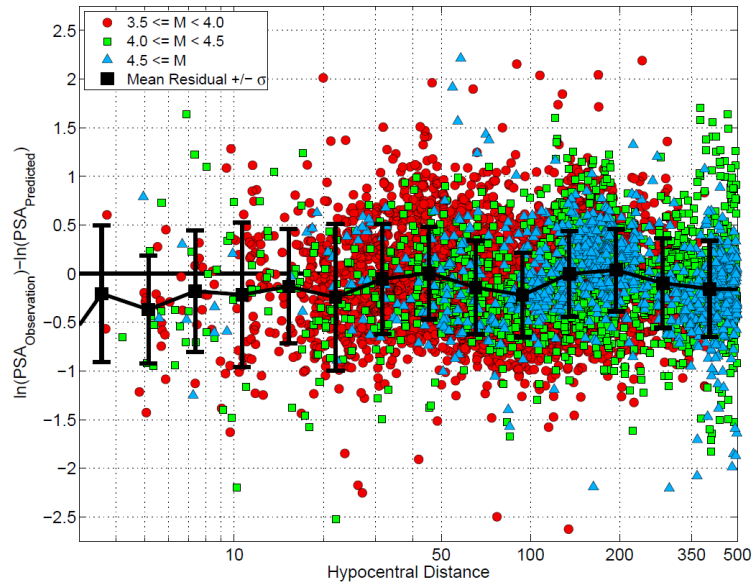


Figure 3.10: Within event residuals with respect to the final GMPE for PSA at 5.12 Hz. Black squares depict the mean residual and its standard deviation in logarithmically spaced distance bins.

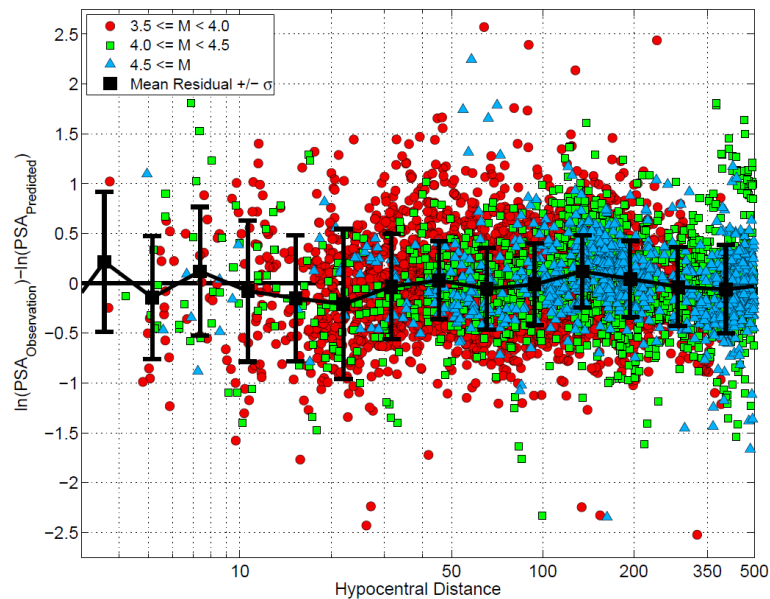


Figure 3.11: Within event residuals with respect to the final GMPE for PSA at 10.2 Hz. Black squares depict the mean residual and its standard deviation in logarithmically spaced distance bins.

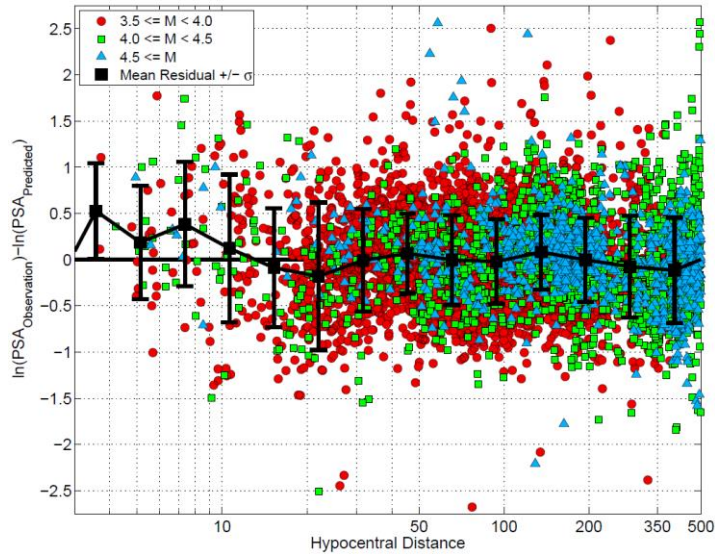


Figure 3.12: Within event residuals with respect to the final GMPE for PGA. Black squares depict the mean residual and its standard deviation in logarithmically spaced distance bins.

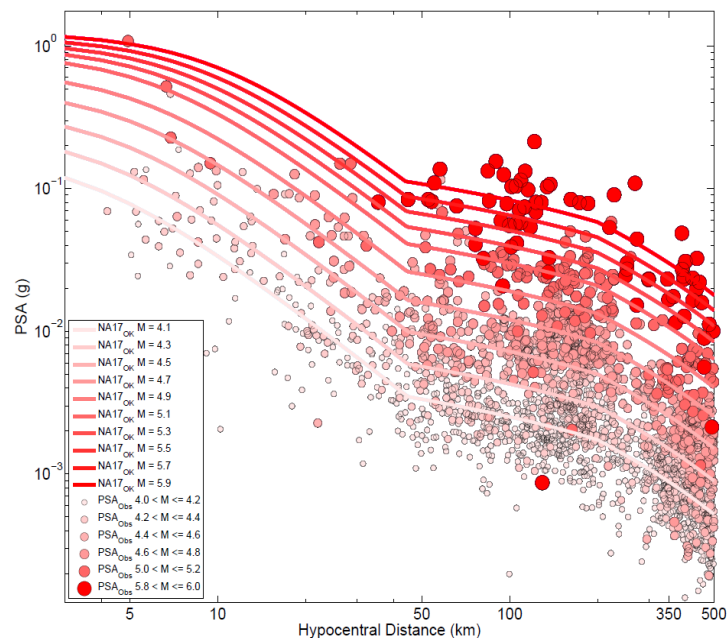


Figure 3.20: Final GMPE overlaying site corrected observations at 5.12 Hz. Lines depict the GMPE evaluated every 0.2 magnitude units from $M = 4.1$ to $M = 5.9$ at linearly-increasing depths ranging from 3 to 8 km, respectively. Circles vary in diameter where larger circles represent larger magnitude observations and smaller circles denote smaller magnitude event observations.

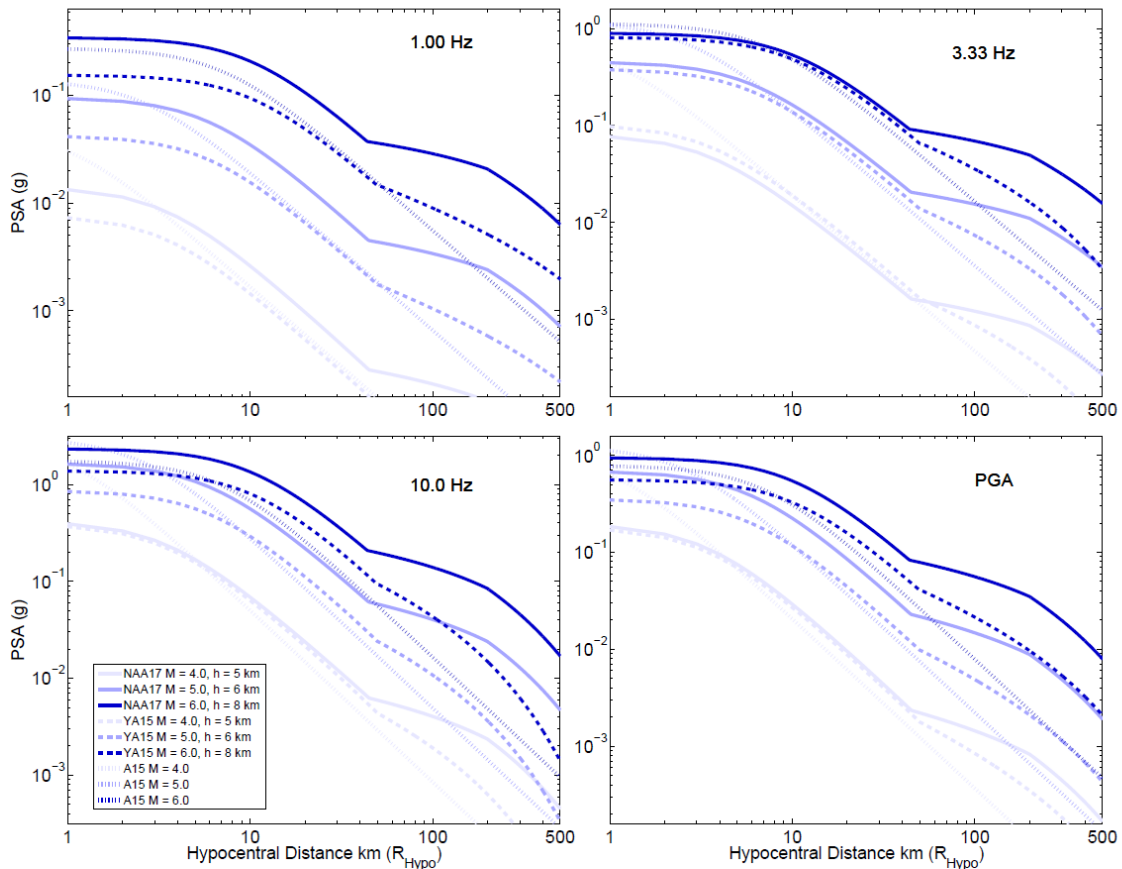


Figure 3.13 The GMPE for Oklahoma as determined in this study (solid lines) in comparison to the YA15 GMPE for CENA (dashed lines); both GMPEs are evaluated for focal depths of 5, 6, and 8 km for $M = 4, 5,$ and $6,$ respectively. The GMPE of Atkinson (2015), as determined from moderate California earthquakes with mean depth of 9 km, is also indicated (dotted lines), and is extrapolated for distances > 50 km. All models are for NEHERP B/C reference site conditions.

3.6 Conclusions

We derived a regionally-adjusted GMPE for induced events in Oklahoma (geometric mean of horizontal components), for a reference site condition of B/C. We used the generic GMPE framework of Yenier and Atkinson (2015b) to ensure stable scaling of motions over all magnitudes and distances. The generic GMPE was calibrated by determining an anelastic attenuation function, site amplification models, regional stress parameter model, and calibration factor from >7000 ground motion observations from

Oklahoma events of $M \geq 3.5$ at hypocentral distances from 2 to 500 km. The derived GMPE is useful for hazard assessments and ShakeMap applications and may also be useful for ground motion-based alerting systems and traffic light protocols.

3.7 Data and Resources

Shear wave velocities, V_{s30} , used to determine B/C reference stations from the EPRI Ground-Motion Model Review Project: Shear Wave Velocity Measurements at Seismic Recording Stations (2013a) was accessed from

<https://www.epri.com/#/pages/product/3002000719/> (accessed November 2016).

Surficial geology also used as a proxy method to select B/C reference stations were found in the USGS National Geologic Map Database at <https://mrdata.usgs.gov/geology/state/> (accessed November 2016). Statistics of seismicity rate increases in Oklahoma from the one-year seismic hazard forecast for the Central and Eastern United States from induced and natural earthquakes, Peterson et al 2016, USGS Open-File Report 2016-1035, from <https://pubs.er.usgs.gov/publication/70182572> (accessed November 2016). The facilities of Incorporated Research Institutes for Seismology (IRIS, www.iris.edu, last accessed Oct. 2017) Data Services, and specifically the IRIS Data Management Center, were used for access to waveforms, related metadata, and/or derived products used in this study. IRIS Data Services are funded through the Seismological Facilities for the Advancement of Geoscience and EarthScope (SAGE) Proposal of the National Science Foundation under Cooperative Agreement EAR-1261681. Ground motion data were downloaded from IRIS then were processed and compiled using an updated version of the ICORRECT algorithm, as described in Assatourians and Atkinson (2017). Careful consideration is being taken as we decide how to partition and organize the near 6.8 million record ground motion database in a useful and meaningful way. The database of processed ground motion observations, event/station metadata, and M estimates for each event will become fully available online in the near future.

3.8 Acknowledgements

This study was funded by the Natural Sciences and Engineering Research Council of Canada and TransAlta. Funding was also received from the U.S. Geological Survey

under Grant G16AP00107. We thank Behzad Hassani for his valuable input on the regression procedure. We thank our anonymous reviewers and Dr. Thomas Pratt for their constructive comments.

3.9 References

- Abrahamson, N. A., and R. R. Youngs. (1992). A stable algorithm for regression analysis using the random effects model, *Bull. Seismol. Soc. Am.* 82(1), 505–510.
- Ambraseys, N. N., & Douglas, J. (2004). Magnitude calibration of north Indian earthquakes. *Geophysical Journal International*, 159(1), 165-206. DOI: 10.1111/j.1365-246X.2004.02323.x
- Andrews, J. (1986). Objective determination of source parameters and similarity of earthquakes of different size, *Earthquake Source Mechanics*, American Geophysical Union, *Geophysical Monograph*, Vol. 37, 259-267.
- Assatourians, K., and Atkinson, G. M. (2010). Database of processed time series and response spectra for Canada: An example application to study of the 2005 MN 5.4 Riviere du Loup, Quebec earthquake, *Seismol. Res. Lett.* 81, no. 6, 1013–1031.
- Assatourians, K., and Atkinson, G. M. (2017). Are Ground-Motion Models Derived from Natural Events Applicable to the Estimation of Expected Motions for Induced Earthquakes? *Seism. Res. Lett.* DOI: 10.1785/0220160153.
- Atkinson, G. M. and Boore, D. M. (2006). Earthquake ground-motion prediction equations for eastern North America, *Bull. Seism. Soc. Am.* 85, 17-30.
- Atkinson, G. M., Hassani, B., Singh, A., Yenier, E. and Assatourians, K. (2015). Estimation of Moment Magnitude and Stress Parameter from ShakeMap Ground-Motion Parameters. *Bull. Seismol. Soc. Am.* 105(5), 2572-2588.
- Atkinson, G. M., and Morrison, M. (2009). Regional variability in ground motion amplitudes along the west coast of North America, *Bull. Seismol. Soc. Am.*, 99, 2393–2409.
- Atkinson, G. M., and Silva, W. (2000). Stochastic modeling of California ground motions. *Bull. Seismol. Soc. Am.* 90, 255-274.
- Boore, D. M. (2003). Simulation of ground motion using the stochastic method, *Pure and Applied Geophysics* 160, 635-675.
- Boore, D. M. (2009). Comparing stochastic point-source and finite-source ground motion simulations: SMSIM and EXSIM. *Bull. Seismol. Soc. Am.* 99, 3202-3216.

- Boore, D. M. (2010). Orientation-Independent, Nongeometric-Mean Measures of Seismic Intensity from Two Horizontal Components of Motion. *Bull. Seism. Soc. Am.* 100, 1830-1835.
- Boore, D. M., Campbell, K. W., and Atkinson, G. M. (2010). Determination of stress parameters for eight well-recorded earthquakes in eastern North America. *Bull. Seism. Soc. Am.* 100, 1632-1645.
- Brune, J. N. (1970). Tectonic stress and the spectra of seismic shear waves from earthquakes. *J. Geophys. Res.* 75(26), 4997-5009.
- Brune, J. N. (1971). Correction: Tectonic stress and the spectra of seismic shear waves, *J. Geophys. Res.* 76(20), 5002.
- Burger, R. W., P.G. Somerville, J.S. Barker, R.B. Herrmann, and D.V. Helmberger (1987). The effect of Crustal structure on strong ground motion attenuation relations in eastern North America. *Bull. Seism. Soc. Am.* 77, 420-439, 1987.
- Cramer, C. (2017). Brune Stress Parameter Estimates for the 2016 M_w Pawnee and Other Oklahoma Earthquakes. *Seismological Research Letters*, 88(4):1005-1016.
- Ellsworth, W. L. (2013). Injection-induced earthquakes. *Science*. 341(6142), 7. doi:10.1126/science.1225942
- Ghofrani, H. and Atkinson G. M. (2014). Site Condition Evaluation Using Horizontal-to-Vertical Response Spectral Ratios of Earthquakes in the NGA-West2 and Japanese Databases. *Soil Dynamics and Earthquake Engineering*.67, 30-43.
- Hassani, B., and Atkinson, G. M. (2015). Referenced empirical ground-motion model for Eastern North America, *Seismol. Res. Lett.* 86(2A), 477-491.
- Hassani, B. and Atkinson, G. M. (2016). Site-effects model for central and eastern North America based on peak frequency. *Bull. Seism. Soc. Am.*, 106, 2197-2213.
- Huang, Y., Ellsworth, W. L., and Beroza, G. C. (2017). Stress drops of induced and tectonic earthquakes in the central United States are indistinguishable. *Science Advances* 3(8), e1700772.
- McGuire, R. K. (2004). *Seismic Hazard and Risk Analysis*, Earthquake Engineering Research Institute. Aug 1, 2004.
- Nigam & Jennings (1969), Calculation of Response Spectra from Strong-Motion Earthquake Records, *Bulletin of the Seismological Society of America*. 59(2), 909-922.

- Novakovic & Atkinson (2015), Preliminary Evaluation of Ground Motions from Earthquakes in Alberta. *Seismol. Res. Lett.*, 86(4), 1086-1095.
- Petersen, et al. (2016). USGS Open-File Report 2016-1035, <https://pubs.er.usgs.gov/publication/70182572> (Last accessed November 2016).
- Schoenball, M., Ellsworth, W.L., (2017). Waveform relocated earthquake catalog for 4 Oklahoma and Southern Kansas illuminates the regional fault network. *Seismological Research Letters*, 88(5), 1252-1258.
- Seyhan, E. and Stewart, J. (2014). Semi-Empirical Nonlinear Site Amplification from NGA-West2 Data and Simulations. *Earthq. Spectra*. 30(3), 1241-1256.
- Strasser, F. O., Abrahamson, N. A., and Bommer, J. J., (2009), Sigma: Issues, Insights, and Challenges. *Seismological Research Letters* 80 (1): 40-56.
- Taves, M. A. (2013). Imaging of the crust and Moho beneath Oklahoma using receiver functions and Pn tomography; With emphasis on the Southern Oklahoma aulacogen. Texas Tech University, 2013. <https://ttu-ir.tdl.org/ttu-ir/bitstream/handle/2346/48853/TAVE-THESIS.pdf?sequence=1&isAllowed=y>, accessed March 15, 2018.
- Wald, D. J., Quitoriano V., Heaton T. H., Kanamori H., Scrivner C. W., Worden C. B. (1999). TriNet ShakeMaps: Rapid generation of peak ground motion and intensity maps for earthquakes in southern California. *Earthq. Spectra*. 15(3), 537-555.
- Yenier, E., and G. M. Atkinson (2014). Equivalent point-source modeling of moderate to large magnitude earthquakes and associated ground-motion saturation effects. *Bull. Seismol. Soc. Am.* 104, 1458-1478.
- Yenier, E., and G. M. Atkinson (2015a). An Equivalent Point-Source Model for Stochastic Simulation of Earthquake Ground Motions in California. *Bull. Seismol. Soc. Am.* 105(3), 1435-1455.
- Yenier, E., and G. M. Atkinson (2015b). Regionally-Adjustable Generic Ground-Motion Prediction Equation based on Equivalent Point-Source Simulations: Application to Central and Eastern North America. *Bull. Seismol. Soc. Am.* DOI: 10.1785/0120140332
- Yenier, E., Atkinson, G. M., Sumy, D. F. (2017), Ground Motions for Induced Earthquakes in Oklahoma, *Bull. Seismol. Soc. Am.* 107(1), 198-215

Chapter 4

4 Empirically-Calibrated Ground Motion Prediction Equation for Alberta

4.1 Introduction

Approximately 1000 seismic events believed to be related to oil and gas activity, in the moment magnitude (M) range of 1 to 4.3, were detected and located across Alberta, Canada, from September 2013 to September 2017. Understanding the ground motions produced by induced seismicity is a prerequisite for assessing and mitigating hazard. Ground-motion prediction equations (GMPEs) expressing peak ground motion and median response spectral amplitudes as functions of magnitude, distance and site condition, are useful for seismic hazard analysis (e.g. McGuire, 2004) and near-real-time ShakeMaps (e.g. Wald et al., 1999).

A region-specific GMPE for Alberta (median horizontal component) is developed using a compiled database of 880 ground motion observations including 37 events of moment magnitude 3 to 4.3, over the hypocentral distance (R_{hypo}) range from 2 to 600 km. We perform a generalized inversion to solve for regional source, attenuation and site responses following the method of Atkinson et al. (2015) within the context of an equivalent-point-source model. The resolved parameters include the regional geometric spreading and anelastic attenuation, source parameters for each event (magnitude scaling and stress parameter for a Brune point-source model), and site response terms for each station, referenced relative to the NEHRP (Natural Earthquakes Hazards Reduction Program) B/C site class boundary (time-averaged shear-wave velocity in the upper 30 m of 760 m/s). These parameters fully specify a regionally calibrated GMPE that can be used to describe median horizontal-component amplitudes across the region for hazard and ShakeMap applications, and to aid in the development of traffic light protocols and other risk-mitigation tools. Alberta ground motions are placed into context by comparing the resulting GMPE with one derived for Oklahoma induced seismicity by Novakovic et al. (2018, denoted as NAA18); NAA18 was calibrated using a larger ground-motion dataset than any previous GMPE study for induced events in North America.

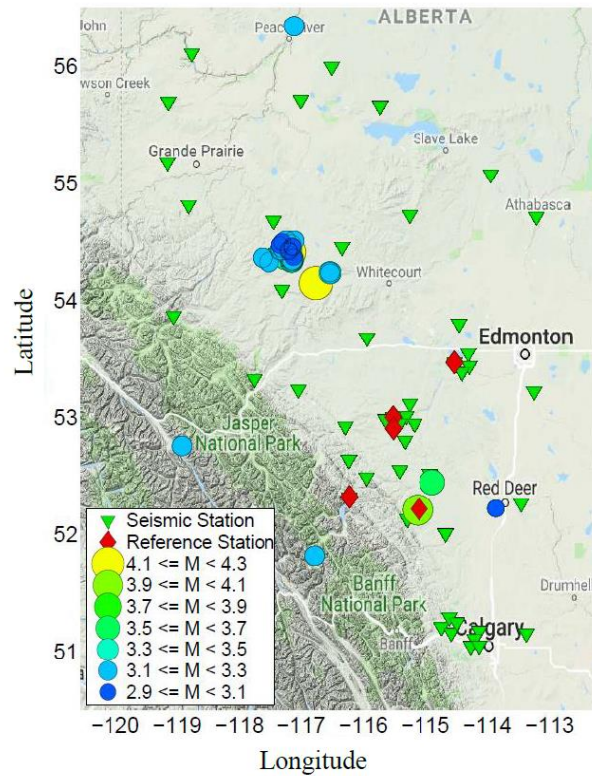


Figure 4.1: Earthquakes (circles) and stations (inverted triangles) used in this study. Stations chosen as B/C reference sites are highlighted (diamonds).

Further comparisons of GMPEs derived from waste-water injection and hydraulic-fracture induced seismic events with GMPEs determined from natural events in CENA and California are made.

4.2 Database

Publicly accessible networks across Alberta, British Columbia, Montana, and Washington (TD, CN, RV, MB, UW, US) were queried through IRIS (Incorporated Research Institute for Seismology) to obtain digital time series for thousands of events as recorded on over 400 three-component broadband seismograph and accelerometer stations. The Canadian Rockies and Alberta Network (CRANE, Gu et al, 2011), operated by the University of Alberta, has also contributed several months of continuous waveform data from 20 active stations in 2013-2014. Waveforms were processed and compiled to produce a ground motion database of 5%-damped pseudo spectral acceleration (PSA), peak ground acceleration (PGA), and peak ground velocity (PGV).

PGA and PGV are computed from the absolute maximum amplitude of the corresponding time series. PSAs are calculated from the corrected time series using the Nigam and Jennings (1969) algorithm, sampled at 30 log-spaced frequencies from 0.20 Hz to 50.0 Hz. Events of $M \geq 3$ at R_{hypo} from 2 km to 575 km are analyzed in this study and are shown in map view in Figure 4.1. Consistent with previous studies (e.g. Yenier and Atkinson, 2015b; NAA18), the GMPE is based on the geometric mean of the horizontal component ground-motion amplitudes. The geometric mean is very similar to the orientation-independent horizontal component measure used in the Next Generation Attenuation database (Boore, 2010), but is more practical to calculate for batch processing large numbers of ground motion records.

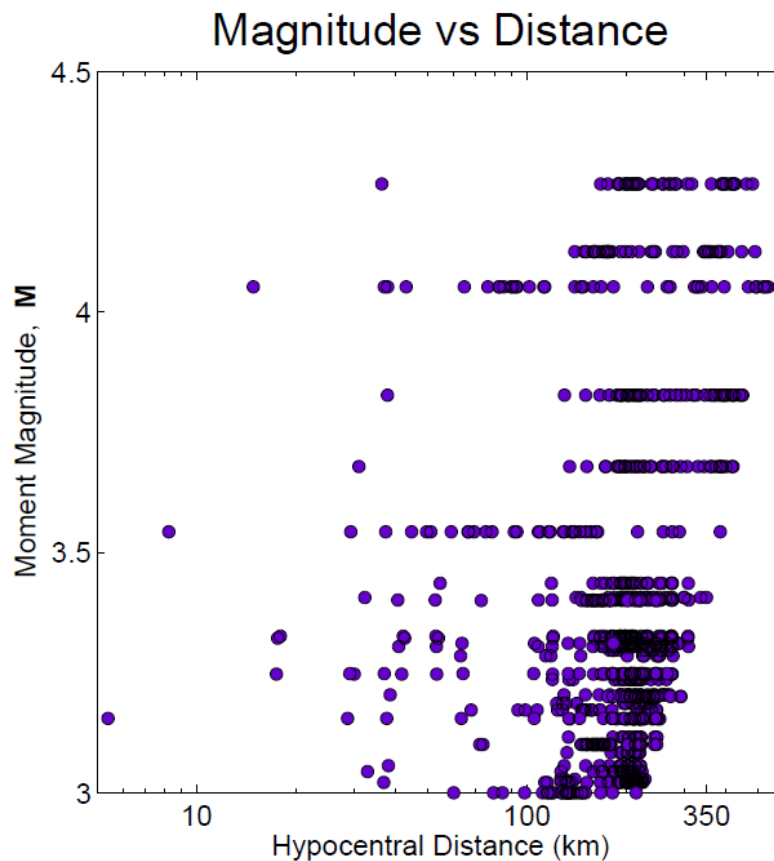


Figure 4.2: The magnitude-distance distribution of the database, containing 884 records from 37 earthquakes (M 3 – 4.3) recorded on 75 seismograph stations. We consider records within logarithmically spaced bins with a cut-off distance that increases from 200 km for $M = 3$ to 575 km for $M \geq 4$ events. The moment magnitude values (M) are determined as described in Figure 4.3.

Standard time-series analysis procedures were applied during the compilation and processing of the ground motion database using an updated version of the ICORRECT algorithm of Assatourians and Atkinson (2010). Records were windowed, glitches and trends were removed, the time series were filtered from 0.10 Hz to 50.5 Hz (4th order Butterworth filter) and corrected for instrument response. We select a signal window length of 300 seconds to ensure the P-wave, S-wave and strongest portions of the coda are captured across all magnitude and distance ranges. This choice in window length is typical of that used to compute response spectra for earthquakes in the range of $M = 3$ to 6 at regional distances (e.g. Assatourians and Atkinson, 2010; NAA18). We checked that there is no sensitivity in the compute PSA to the selected window length, provided that the entire signal is captured. Broadband seismograph records are differentiated in the frequency domain prior to conversion back to the time domain to generate acceleration time series. The digital time series of accelerometer records are already correctly scaled in acceleration and can be integrated to calculate velocity. No individual visual inspection of the seismograph records was performed during batch processing as it would be impractical to perform on the large database (~400,000 records in total). Low-frequency microseismic noise within the selected passband will inherently contribute, to some degree, to the spectral amplitudes, especially for small magnitudes at larger distances. However, it should be noted that the PSA amplitudes accurately reflect the corresponding oscillator response to the motions, as this ambient vibration is a real component of the signal. Through our record selection criteria, we have attempted to limit the impact of such noise contributions. Striking a balance between limiting noise contributions and preserving enough records for regression, we impose a cut-off distance of 200 km for M 3.0, with this cut-off distance growing steadily to 575 km for $M \geq 4$. Figure 4.2 shows the magnitude and distance distribution of the selected database. A total of 884 ground motions recorded at 75 seismic stations from 37 earthquakes of M 3 to 4.3 are selected for this study.

4.3 Estimation of Moment Magnitude

Moment magnitude (\mathbf{M}) is estimated for each event from the spectral amplitude of the low-frequency end of the spectrum using a slightly modified version of the method outlined in Novakovic and Atkinson (2015):

$$\mathbf{M} = \frac{\log_{10}(\text{PSA}_F) + \text{MC}_F + 1.3 \log_{10}(R_{hypo}) + \gamma_F R_{hypo}}{1.45} \quad (4.1)$$

where Equation (4.1) is evaluated using PSA_F at two frequencies: 1.00 and 3.33 Hz. The level of the equation is matched by the magnitude calibration factor MC_F , whilst the anelastic attenuation coefficient γ_F removes regional attenuation trends with distance. These parameters and their values are listed in Table A4.1. The magnitude estimate is based on the recorded PSA at the five closest stations (to minimize the impact of attenuation and noise) using the vertical-component amplitude (to minimize the effects of site response) (Novakovic and Atkinson, 2015).

The Novakovic and Atkinson (2015) algorithm is modified for this study by using an event-adjusted attenuation model to ensure that there will be no significant distance dependence in the residuals. The modified algorithm tests three alternative values for γ_F to consider low (e.g. Central and Eastern North America (CENA), γ_{Low}), high (e.g. California, γ_{High}) or moderate (γ_{Mod}) anelastic attenuation rates. Coefficients for CENA and California attenuation are given in Novakovic and Atkinson (2015); these are the values used for the low and high attenuation models, respectively, whilst the intermediate model is the geometric mean of the two values. We select the attenuation rate that minimizes the standard deviation of the residuals for each event. Initial values of \mathbf{M} are calculated from both 1.00 Hz and 3.33 Hz ground motions to balance the opposing considerations of noise and corner frequency. Specifically, it is necessary to use a frequency that is low enough to be below the corner frequency for the event magnitude so that we are measuring the low-frequency end of the spectrum. However, we also wish to minimize the contributions of noise, which become important at low frequencies for small events.

Moment magnitude for larger magnitude events in Alberta ($M > 3$) are best estimated by the 1.00 Hz PSA, whilst PSA at 3.33 Hz is a good choice for smaller events, $M < 3$. It should be noted that in NAA18, Oklahoma events of $M \geq 4$ are computed using PSA at 0.30 Hz, although the M estimates obtained from PSA at 1.0 Hz do not saturate until $M > 4.5$. The paucity of $M > 4$ events in Alberta made this refinement unnecessary; moreover, we noted that the M estimates we obtained from PSA at 1.0 Hz agree well with those from moment tensor solutions (e.g. Wang et al. 2015; 2017; Schultz et al., 2017). The best magnitude estimate is selected according to the magnitude range, as illustrated in Figure 4.3 (see also Novakovic and Atkinson, 2015; NAA18). M_F is the magnitude computed from PSA at frequency F . If both $M_{3.33 \text{ Hz}} < 3$ and $M_{1.00 \text{ Hz}} < 3$, then this is a small event and we accept $M_{3.33 \text{ Hz}}$ as the event magnitude. If not, we proceed sequentially to consider the lower-frequency estimates of magnitude. If $M_{3.33 \text{ Hz}} < 3$ and $M_{1.00 \text{ Hz}} \geq 3$, we take the mean of these two calculations as the event magnitude. If not, we check if both $M_{3.33 \text{ Hz}} \geq 3$, and $M_{1.00 \text{ Hz}} \geq 3$; if true, then this is a large event and we accept that $M_{1.00 \text{ Hz}}$ is the event magnitude.

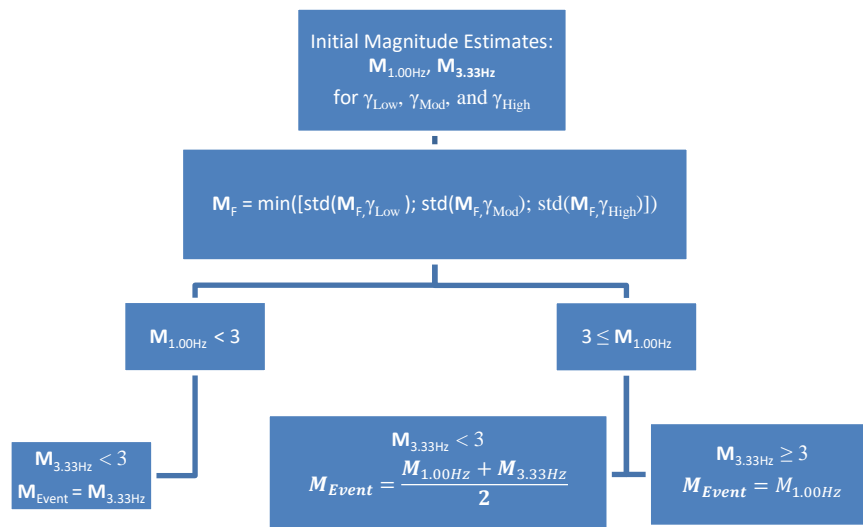


Figure 4.3. The decision tree to decide which frequency is used to estimate moment magnitude (M) of the event. We compute M based on PSA at 1.00 Hz and 3.33 Hz. The M estimate from 3.33 Hz PSA is used for events of $M < 3$, 1.00 Hz estimate for $M \geq 3$, and the mean of the two values for $M \sim 3$. For each event, the anelastic attenuation coefficient that minimizes the residuals is chosen, where three values are considered: low (CENA value), high (California value) or moderate (average of the two).

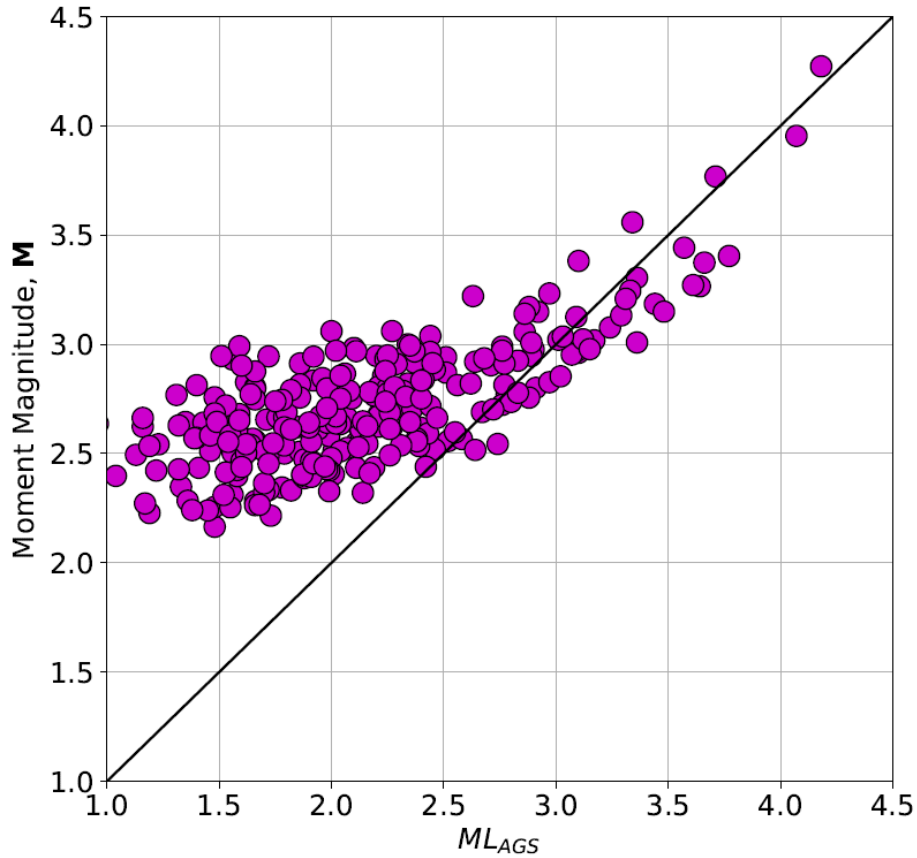


Figure 4.4. Comparison of moment magnitude estimates based on PSA with Alberta Geological Survey reported Local magnitudes (M_{LAGS}). The two scales agree quite well for $M > 2.6$; ground motion response amplitudes scale weakly with ML at lower magnitudes.

The resulting values of M are in good agreement with Alberta Geological Survey calculations of local magnitude in the region, for $ML > 2.6$, as shown in Figure 4.4 (Stern et al., 2018).

4.4 Ground Motion Model

GMPEs are described by the M , hypocentral distance (R_{hypo}), and a station-specific site response. We use a generalized inversion (Andrews, 1986) to solve for anelastic attenuation, site response and regional source parameters of the generic GMPE form:

$$\ln(Y) = F_E + F_K + F_Z + F_\gamma + F_s + C \quad (4.2)$$

where $\ln(Y)$ is the natural logarithm of PSA at a selected frequency. F_E , F_Z , F_γ , and F_s are the earthquake source term, geometric spreading model, anelastic attenuation function, and site response term, respectively. The empirical calibration factor C captures residual differences between simulations and empirical data. These model terms express the components of a stochastic equivalent point-source model (e.g. Boore, 2003) and are based on the generic GMPE of Yenier and Atkinson (2015b). The near-surface high-frequency attenuation function, F_κ , is adapted from Hassani and Atkinson (2018). Basic scaling of the model in magnitude, distance, and frequency content is constrained to follow seismological scaling principles, but the parameter values representing the Brune (1970, 1971) stress, attenuation and site responses are calibrated by regional observations. A summary of these components is given in the following; see Yenier and Atkinson (2015b) for more details.

Magnitude and stress parameter effects on ground motion amplitudes are described by the earthquake source function F_E , adopted from the reference model developed by Yenier and Atkinson (2015a), which was based on equivalent point-source simulations calibrated to the NGA-East and NGA-West 2 databases. The implicit assumption is that the general magnitude-scaling characteristics of ground motions are not region specific (e.g. Ambraseys and Douglas, 2004; Atkinson and Morrison, 2009); this form ensures that a model calibrated using data from moderate magnitudes will scale appropriately to larger magnitudes. The source function is given as:

$$F_E = F_M + F_{\Delta\sigma} \quad (4.3)$$

F_M represents the magnitude effect on ground motion amplitudes that would be observed at the source if there were no near-distance saturation effects for a specified reference stress ($\Delta\sigma=100$ bar), near-surface attenuation ($\kappa_0=0.025$ s), and site condition (B/C). The F_M term is a hinged quadratic function of \mathbf{M} :

$$F_M = \begin{cases} e_o + e_1(\mathbf{M} - M_H) + e_2(\mathbf{M} - M_H)^2 & \mathbf{M} \leq M_H \\ e_o + e_3(\mathbf{M} - M_H) & \mathbf{M} > M_H \end{cases} \quad (4.4)$$

where frequency dependent coefficients, e_0 to e_3 and the hinge magnitude M_H were determined by Yenier and Atkinson (2015b) using stochastic equivalent point-source simulations. The stress adjustment term $F_{\Delta\sigma}$ is needed when $\Delta\sigma$ is different than 100 bars and is defined as:

$$F_{\Delta\sigma} = e_{\Delta\sigma} \ln(\Delta\sigma/100) \quad (4.5)$$

where the rate of ground motion scaling with $\Delta\sigma$ is described by $e_{\Delta\sigma}$. Equation 4.5 provides the relationship between stress parameter and response spectral amplitudes allowing the determination of $\Delta\sigma$ from PSA observations. Its form is given by:

$$e_{\Delta\sigma} = \begin{cases} s_0 + s_1 M + s_2 M^2 + s_3 M^3 + s_4 M^4 & \Delta\sigma \leq 100 \text{ bar} \\ s_5 + s_6 M + s_7 M^2 + s_8 M^3 + s_9 M^4 & \Delta\sigma < 100 \text{ bar} \end{cases} \quad (4.6)$$

where s_0 to s_9 are frequency dependent coefficients.

A trade-off exists in ground-motion modeling between stress parameter and the near-surface high-frequency attenuation slope, kappa (κ_0) (Anderson and Hough, 1984). Yenier and Atkinson (2015) used a fixed kappa and site condition to constrain this trade-off. Hassani and Atkinson (2018) extended their model to allow variable site conditions and kappa combinations, by introducing a kappa term (F_κ) and site response term (F_S) in the response spectral domain (e.g. Equation 4.2). The kappa term is defined by the following polynomial (Hassani and Atkinson, 2018):

$$F_{\kappa_0} = \sum_{i=0}^4 e_{\kappa_0,i} [\log_{10}(\kappa_0)]^i \quad (4.7)$$

where $e_{\kappa_0,i}$ are magnitude-dependent coefficients. Because the kappa term is 0 for the reference value of $\kappa_0 = 0.001$ s, it is required that

$$e_{\kappa_0,0} = 3e_{\kappa_0,1} - 9e_{\kappa_0,2} + 27e_{\kappa_0,3} - 81e_{\kappa_0,4}. \quad (4.8)$$

The magnitude-dependent coefficients for each of the $i = 1-4$ of the F_{κ_0} functional form can then be expressed as

$$e_{\kappa_0,i} = \sum_{j=0}^3 P_{i,j} [\log_{10}(\mathbf{M})]^j \quad (4.9)$$

and stress-parameter-dependent coefficients of $e_{\kappa_0,i}$, $P_{i,j}$ can be written as

$$P_{i,j} = \sum_{n=0}^2 d_{i,j,n} [\log_{10}(\Delta\sigma)]^n \quad (4.10)$$

in which $d_{i,j,n}$ are the coefficients of $P_{i,j}$ for each oscillator frequency, $i= 1-4$, $j = 0-3$, and $n = 0-2$. The Yenier and Atkinson (2015b) model implicitly applies to $\kappa_0 = 0.025$ s, so we chose to reference the kappa term (F_{κ}) from equation 4.2 to this value as:

$$F_{\kappa} = F_{\kappa_{AB}} - F_{\kappa_{0.025}} \quad (4.11)$$

where $F_{\kappa_{AB}}$ is the F_{κ_0} function evaluated for the kappa term determined for Alberta, and $F_{\kappa_{0.025}}$ is the F_{κ_0} function evaluated for the reference kappa of 0.025s. The kappa function is evaluated for the frequencies which coefficients are provided in Hassani and Atkinson (2018), then interpolated to the frequencies used in this study for both the regional kappa term determined for Alberta and the reference kappa term.

A trilinear geometric spreading functional form is adopted instead of the bilinear form used in Yenier and Atkinson (2015a, b) and Yenier et al. (2017) in order to accommodate a flat transition zone from direct-wave to surface-wave spreading. Strong influences of Moho bounce effects (Burger et al., 1987) observed in this region are better reflected in the trilinear form. Generally, the Mohorivicic discontinuity is ~ 35 km deep in the northern Western Canadian Sedimentary Basin and dips to depths of ~ 50 km under the Rocky Mountains that borders BC and Alberta, reaching depths of as much as 58 km towards the south of the province (e.g. Gu et al, 2011; Bouzidi et al, 2002). Moho depth variations across the region can explain the broad range over which these bounce effects are observed; these effects will be seen clearly in the subsequent analysis and figures. F_Z is a function of R_{hypo} , \mathbf{M} , and transition distances R_t :

$$\mathbf{F}_Z = \ln(Z) + (b_3 + b_4 \mathbf{M}) \ln\left(\frac{R}{R_{ref}}\right) \quad (4.12)$$

$$R = \sqrt{R_{hypo}^2 + h_{eff}^2},$$

$$h_{eff} = 10^{(-0.405 + 0.235\mathbf{M})},$$

$$R_{ref} = \sqrt{1^2 + h_{eff}^2}$$

$$\mathbf{Z} = \begin{cases} R^{-1.3} & \text{for } R \leq R_{t_1} \\ R_{t_1}^{-1.3} \left(\frac{R}{R_{t_1}}\right)^{1.3} & \text{for } R_{t_1} < R \leq R_{t_2} \\ R_{t_1}^{-1.3} \left(\frac{R_{t_2}}{R_{t_1}}\right)^{1.3} \left(\frac{R}{R_{t_2}}\right)^{-0.5} & \text{for } R_{t_2} < R \end{cases}$$

We assume R_{hypo} is equal to the closest distance to the fault rupture for the small to moderate events of this study. To account for close-distance saturation effects due to finite-fault effects, we introduce the magnitude-dependent pseudo-depth term, h_{eff} . An implicit assumption is that finite-fault effects in all regions will influence near-distance saturation effects in a similar way; further discussion of the saturation term is given by Yenier and Atkinson (2014). The coefficients b_3 and b_4 account for the change in apparent attenuation that occurs when ground motions are modeled in the response spectral domain rather than the Fourier domain (Yenier and Atkinson, 2015a).

We adopt a frequency-independent geometric spreading model allowing frequency-dependent effects to be carried by the anelastic attenuation coefficient; this is consistent with nearly all previous stochastic models of ground motion (e.g. Yenier and Atkinson, 2015a/b; Boore, 2003; Atkinson and Boore, 2016; NAA18). To define the shape of the trilinear form, we first assume that the anelastic attenuation and stress parameter models derived in NAA18 are valid in Alberta and remove the magnitude scaling and anelastic attenuation functions. Residual ground motion trends are plotted against R_{hypo} at each frequency. Model parameters are chosen that broadly match the shape across all frequencies, suggesting that a trilinear geometric spreading function with transition

distances of 90 km and 160 km and slopes of -1.3, 1.3, and -0.5 is appropriate for the region. Yenier (2017) developed a local magnitude relation for the Western Canadian Sedimentary Basin (WCSB) that introduced a trilinear distance correction model to correct for the decay in Wood-Anderson amplitudes, which features a steep transition zone that agrees well with that found in this study. Figure 4.5 depicts the adopted trilinear model shape in comparison to PSA values that have been normalized in amplitude (except for the geometric spreading effects) by removing the magnitude scaling and anelastic attenuation terms. Figure 4.5 suggests that the adopted geometric spreading model, though not perfect at all frequencies, provides a reasonable balance between modeling the most important decay trends whilst maintaining simplicity.

With the geometric spreading model constrained, all remaining coefficients can be

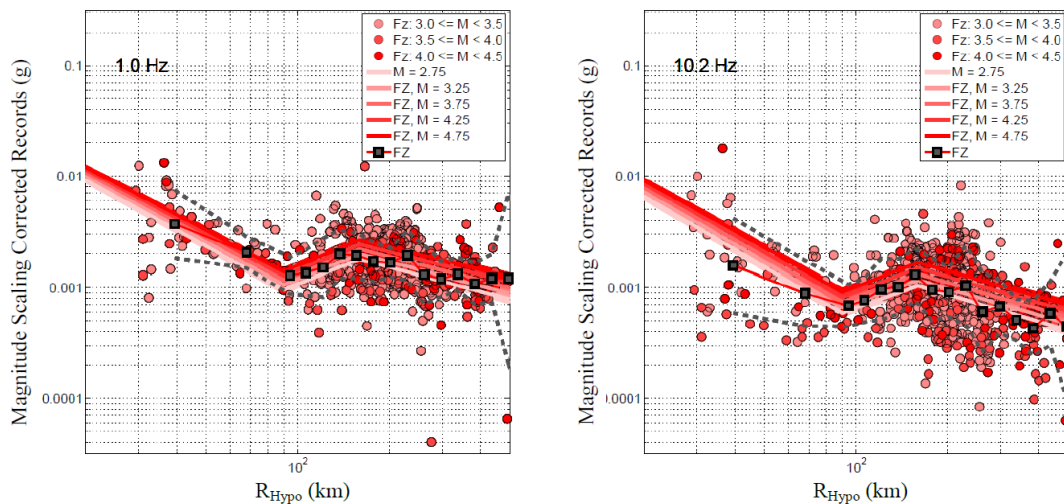


Figure 4.5. Observed normalized amplitudes (circles) after correction for magnitude dependence (F_M , Equation 4.4), Oklahoma stress parameter model and anelastic attenuation (Equations 4.5 & 4.13); squares show median normalized amplitudes in distance bins. Solid lines show the adopted trilinear geometric spreading function (which has magnitude dependence as in YA15), for a range of magnitudes, assuming a 100-bar stress parameter; only the shape is important, as the level is determined by inversion. A constant is added to all ground motions to adjust the level of the geometric spreading function for better visualization. Large scatter, shown by the standard deviation (black dashed lines), at near distances reflects variability in source amplitudes.

determined by inversion, as in Atkinson et al. (2015). We determine the regional anelastic attenuation function F_γ in the inversion process:

$$F_\gamma = \gamma R_{\text{hypo}} \quad (4.13)$$

where γ is a frequency-dependent anelastic attenuation coefficient. Yenier and Atkinson (2015b) determined γ values for CENA and for California using the Next Generation Attenuation (NGA) East and NGA-West 2 databases, respectively. NAA18 determined the anelastic attenuation coefficient for Oklahoma, finding it to be stronger than typically observed in CENA for low frequencies, but weaker than comparable values in California. At frequencies greater than 2.00 Hz, Oklahoma anelastic attenuation appears to be weak even in comparison to values in CENA. In this study, we determine the anelastic coefficient from the Alberta database in the inversion, frequency by frequency, and compare with attenuation rates from other studies (Novakovic and Atkinson, 2015; Atkinson et al., 2014).

Station terms F_s are expressed relative to a reference NEHRP site condition.

Seismograph stations thought to be located on sites with time-averaged shear-wave velocities in the top 30 m (V_{s30}) of ~ 760 m/s are chosen as reference sites, with respect to which all other site responses will be determined. Farrugia et al. (2017) suggest that generally the site condition in Alberta is C-D, based on a combination of H/V ratio analysis and results from site-specific studies. H/V ratios are used as an initial guide to selection of sites likely to be suitable reference sites as shown in the electronic supplement of Farrugia et al. (2017). We select five reference sites, which are post-hole installations thought to be coupled near bedrock and have well-behaved horizontal to vertical component ratios that are broadly similar to each other and consistent with those expected for near B/C sites based on other studies (e.g. Ghofrani and Atkinson, 2014). Moreover, we restrict our reference station selection to the stiffest sites available, as determined by Farrugia et al. (2017) using surface ambient noise vibration. The inversion constraint applied is that the average site amplification over these selected reference stations at each frequency is zero. This constraint will calibrate the GMPE to be applicable for an average B/C site condition, provided that the reference sites represent

typical responses for B/C sites. All site terms are thus relative to the average site amplification for the reference sites, by definition. Any differences between the actual amplification of the five sites (on average) and that assumed for B/C sites in the underlying generic GMPE of Yenier and Atkinson (2015b), will be cast into the calibration constant (C) by the inversion. A summary table of the model coefficients is provided in Table A4.2. A full table, including the evaluated GMPE, are given in Table S4.1.

4.5 Application to Induced Events in Alberta

The record set was further filtered to ensure that each analyzed event is recorded on at least five stations, and that each station records at least 5 events to allow for robust determination of source, site, and event terms. The database for the inversion of Equation 4.2 contains 884 records from 37 events of $M \geq 3.0$ events at 75 stations, as shown in Figure 4.2. We take the geometric mean of the two horizontal-component PSA values in units of g , for 30 logarithmically spaced frequencies from 0.20 Hz to 50.0 Hz, PGA, and PGV.

To facilitate inversion, the fixed geometric spreading function and magnitude scaling terms from Equation 4.2 are subtracted from the observed ground motion values:

$$\ln(Y_{ij}) - F_{M,i} - F_{Z,i,j} = E_i + F_{S,j} + \gamma R_{\text{hypo } ij} \quad (4.14)$$

where Y_{ij} is the ground-motion parameter for event i and station j . $F_{M,i}$ and $F_{Z,i,j}$, are the magnitude scaling term and geometric spreading term for event i and station j , as calculated given the known M and distance $R_{\text{hypo } ij}$. Note that the stress parameter function ($F_{\Delta\sigma}$), near-surface high-frequency attenuation parameter (F_{κ}) and the empirical calibration factor (C) are implicitly included in the event term, E_i . $F_{S,j}$ is the site amplification term relative to the reference B/C site condition at station j . γ is the regional anelastic attenuation term.

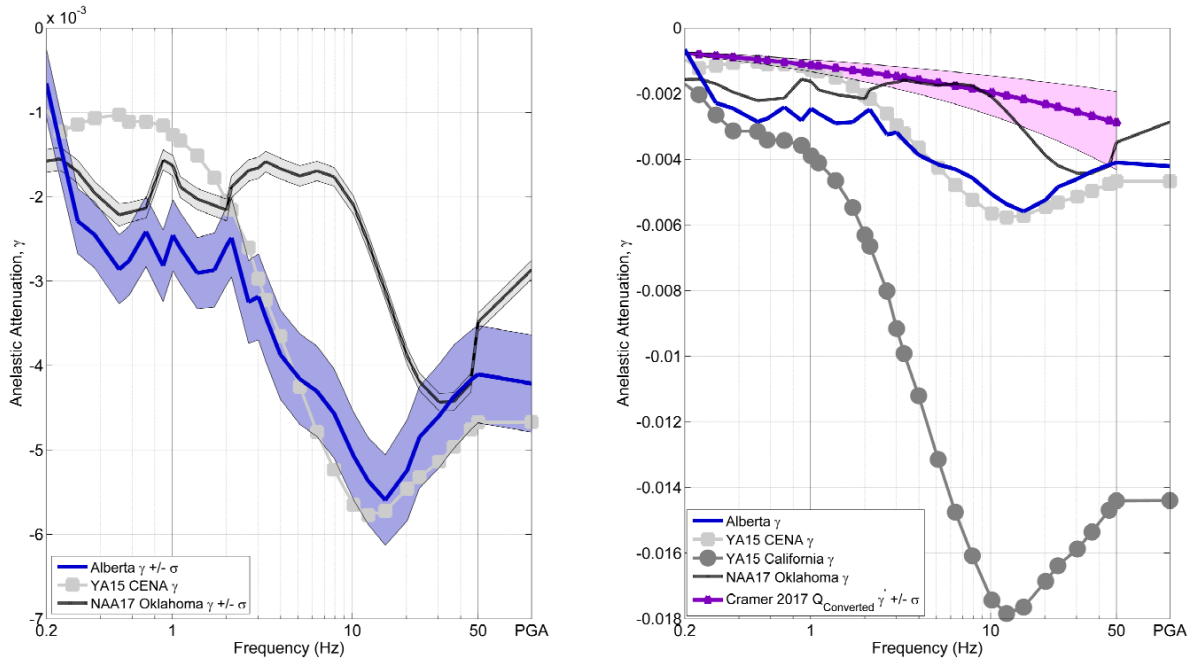


Figure 4.6: Regional anelastic attenuation function obtained from the inversion (Alberta), in comparison to previous results of Novakovic et al. (2018) for Oklahoma, Cramer (2017) Q-converted anelastic attenuation for Oklahoma, Yenier and Atkinson (2015b) for California and Central and Eastern North America.

The unknown terms in Equation 4.14 are obtained for each ground-motion frequency using the generalized inversion scheme of Andrews (1986). Figure 4.6 shows the resulting anelastic attenuation term for Alberta as a function of frequency with its standard deviation, as well as the anelastic attenuation determined for Oklahoma from Novakovic et al. (2018), the CENA and California models from Yenier and Atkinson (2015b), and the Q-converted anelastic attenuation for Oklahoma from Cramer (2017). Generally, we observe similar attenuation to that for CENA at frequencies greater than 8.00 Hz, with slightly stronger (moderate) attenuation for frequencies less than 5.00 Hz. At frequencies from 2.00 Hz to 20.0 Hz, anelastic attenuation in Alberta is stronger than that observed in Oklahoma (Cramer, 2017; Novakovic et al., 2018).

The site amplification term ($F_{s,j}$) is obtained for each of the 75 stations, relative to the assumed reference site condition of B/C, as represented by the average over the five selected reference sites. The selected reference stations are all post-hole seismometers

that provide well behaved horizontal-to-vertical component ratios and B/C like responses. We note that these site amplification terms can be subtracted from the observations to level all records to the same reference site condition. The site amplification terms for each station (in \ln units) are given in Table S4.2, available in the electronic supplement. Figure 4.7 shows the site amplification functions for the reference stations. Although the inversion is constrained by defining that the average site response over the five reference stations is zero (in \ln units), the mean of all station terms is not expected to be zero, because most sites are softer than B/C. Figure 4.8 plots a sample of typical site response functions for non-reference stations. As expected, the peak amplifications for many sites are significant, in some cases exceeding a factor of five at specific frequencies. Figure 4.9 plots all site response functions retrieved from the inversion along with their mean and standard deviation. The mean response across all stations increases steadily from a factor of 1 at 0.20 Hz to a factor of 2 at 10.0 Hz. This average response is consistent with our understanding that the sites range from NEHRP class C to E (e.g. Farrugia et al., 2017).

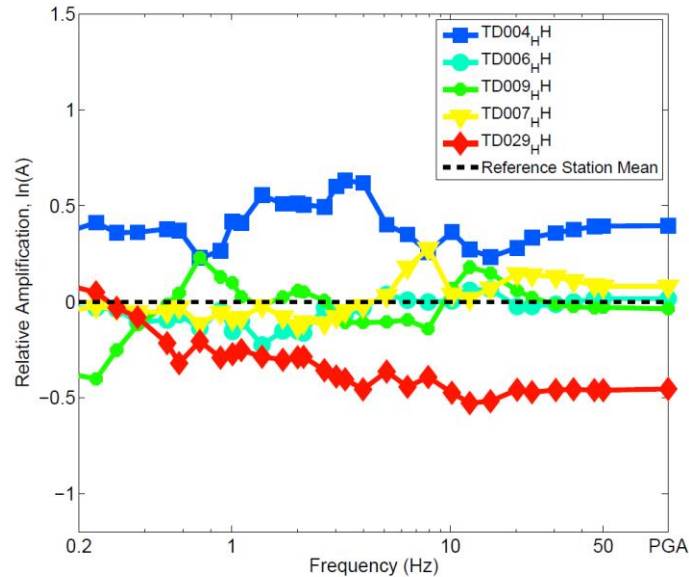


Figure 4.7: Site amplification (\ln units) for the assigned reference B/C stations as obtained from the inversion. The average over the five reference stations is 0 by definition.

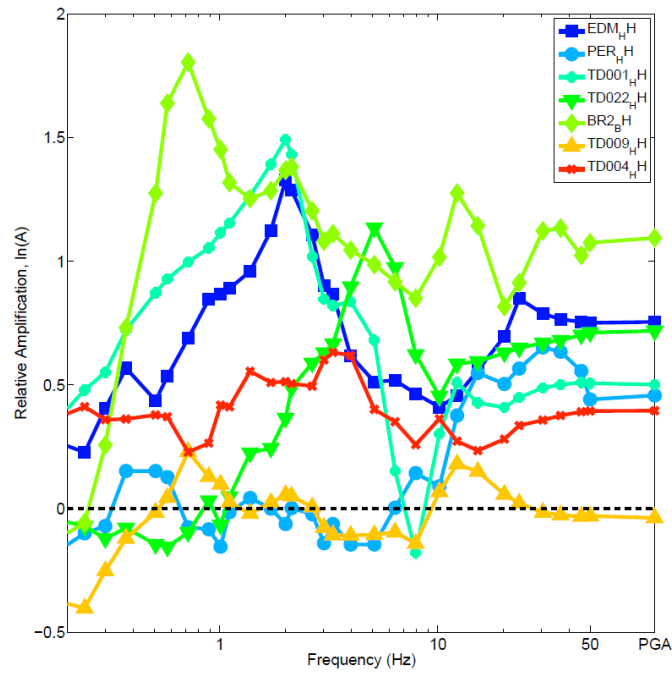


Figure 4.8: Typical site amplification (ln units) for non-reference stations

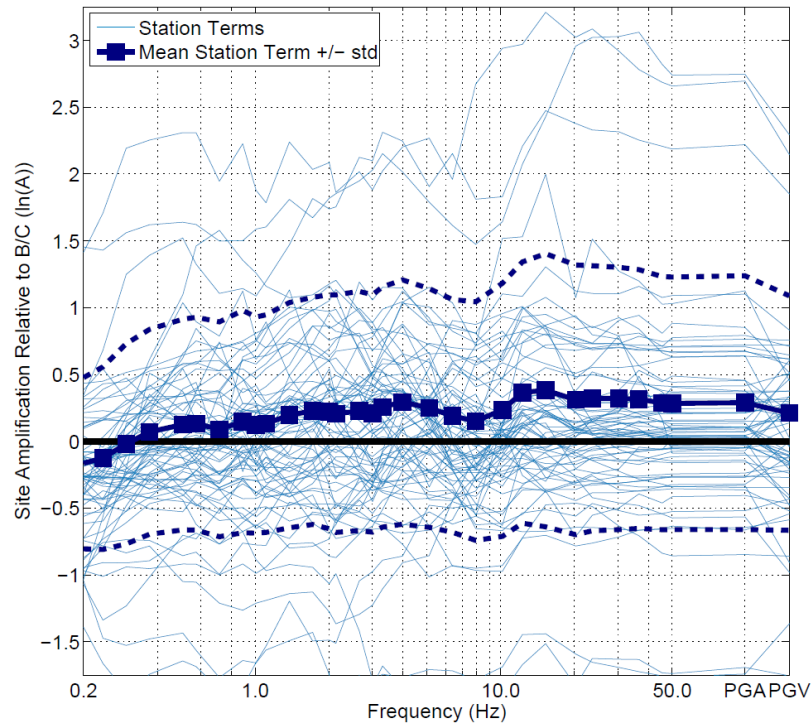


Figure 4.9: All station terms. The lines depict the site response relative to B/C condition for all stations used in the study in natural log units. Squares depict the mean site term for each frequency with their standard deviation in dashed lines.

The event term (E_i) determined by the inversion implicitly includes the event-specific stress adjustment factor for each event, average near-surface site effects for the reference sites, and the regional calibration factor. Boore et al. (2010) showed that a common approach of determining the stress parameter by matching amplitudes at high frequencies for a known moment magnitude can lead to strong non-uniqueness in $\Delta\sigma$ values, due to the tradeoff between the earthquake source and amplitude decay parameters. Yenier and Atkinson (2015b) chose to solve this problem by basing the stress parameter value on the corner frequency (spectral shape), and by using a calibration constant to reconcile the overall spectral amplitude levels relative to those expected for the specified seismic moment. In this study, we follow the approach taken in Novakovic et al. (2018) that is similar to that of Yenier and Atkinson (2015b), but results in a more stable determination of the stress parameter for cases where the source spectrum does not nicely follow the ideal Brune-model spectral shape. In Novakovic et al. (2018), determination of the stress parameter is based on the event's average high-frequency spectral level, as represented by PSA at 10 Hz, relative to that expected based on the seismic moment, accounting for any offset in amplitude level at the moment-end of the spectrum. For event terms in Alberta, we observed that high-frequency level tends to be best expressed in the frequency range from 6.00 to 8.00 Hz (Note: this can be seen in Figures 4.11-4.13). We used the event term as evaluated at 6.30 Hz to represent the high-frequency level for each event. We use the attenuation function from the inversion to correct observations to the reference distance of 20 km, taking the average of attenuation-corrected spectra over all stations for each event. The average event spectrum at 20 km is used to first find the offset of the long-period PSD (pseudo spectral displacement) level at 1.00 Hz from that expected for the given moment for the event, in \ln units (ΔLF), for an ideal 100-bar Brune model spectrum, as defined by Yenier and Atkinson (2015b). The offset given by ΔLF is removed from the average event spectrum, so that it now matches the level for an ideal Brune spectrum of that moment magnitude, at low frequencies. The amount by which the 10-Hz PSA value of this amplitude-corrected spectrum differs from that expected for a 100-bar Brune-model spectrum is taken as a measure of the stress parameter. Higher values of stress result in larger values of 6.30-Hz PSA, relative to the 100-bar model, whereas lower stress results in lower 6.30-Hz PSA values. Note this is

similar to the shape-based approach of Yenier and Atkinson (2015b) but focuses on the high-frequency spectral level relative to the low-frequency level, instead of focusing on the corner frequency.

For ease of application in implementing this approach, the generic GMPE of Yenier and Atkinson (2015b) was evaluated at 20 km for multiple combinations of magnitude and stress parameter, then is used to define the relationship between 6.30 Hz PSA and stress parameter:

$$\log_{10}(\Delta\sigma) = 2.024 + 1.52(\log_{10}(PSA_{6.3\text{Hz},\text{event}}) - (\log_{10}(PSA_{6.3\text{Hz},100\text{bar}}) + \Delta LF)) * \max(1, 1.3 \left(\frac{3.5}{M}\right)) \quad (4.15)$$

where $PSA_{6.30\text{ Hz},\text{event}}$ is the average 6.3 Hz PSA value for the event, adjusting for site and path effects to the reference distance of 20 km, and $PSA_{6.30\text{ Hz},100\text{bar}}$ is the corresponding 6.30 Hz PSA that is predicted for a Brune stress parameter of 100-bar at 20 km. This parameterization makes it easy to back-calculate the stress parameter from the 6.30 Hz value of the event spectrum at 20 km. The basic idea is that we are using the high-frequency spectral level to infer the corner frequency, instead of using the corner frequency to infer the high frequency level (as was done in Yenier and Atkinson, 2015b). This approach was found to be more stable by Novakovic et al. (2018), leading to a lower standard deviation of determined stress parameters.

Stress parameter values for all study events are given in Appendix Table A4.2 of the electronic supplement. The stress parameter increases with magnitude for small events and the values fall within the range that would be expected (Yenier & Atkinson, 2015b; NAA18). A wide range of stress parameter values, typically from 10 to 200 bars, are observed for events of $M > 3$. It has been suggested that stress increases with focal depth, and that this is the primary reason why induced events typically have a lower stress parameter than do natural tectonic earthquakes (e.g. Yenier and Atkinson, 2015b; Atkinson and Assatourians, 2017; Novakovic et al. 2018). Catalog depths for the events (Table A4.2) fall predominantly in the range from 1 to 10 km, however the errors in depth calculations are often larger than the measurement itself, precluding any

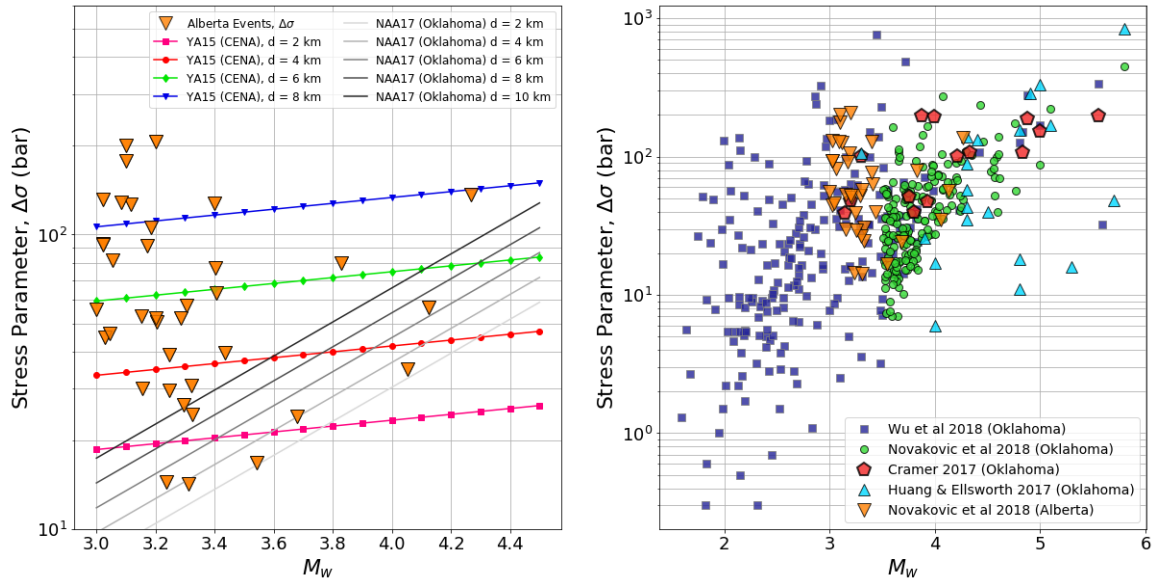


Figure 4.10: (Left) stress parameters determined by inversion for each event as a function of M (triangles). Solid lines show the stress parameter model for Oklahoma evaluated over a range of depths. Lines with symbols depict YA15 stress parameter models for CENA over a range of depths. (Right) Composition of stress parameter computations in this study with suspected induced events in Oklahoma from other studies.

meaningful interpretation of depth effects within the source terms. In Figure 4.10, stress parameters are plotted as a function of magnitude against models for CENA and Oklahoma and compared to values determined for suspected induced events in other studies (Cramer, 2017; Huang & Ellsworth, 2017; Wu et al., 2018; Novakovic et al., 2018). Stress parameters determined for hydraulic fracture induced events in Alberta lie within the range of stress drop values for waste water injection induced events in Oklahoma, as determined through other techniques (Fourier spectral fitting and empirical Greens functions). Goertz-Allmann et al. (2011) computed stress drops for 1000 events induced by geothermal water injection in a deep borehole in Basel, Switzerland. Stress drops typically range from 2 to 200 bar, and on average fall within 20 to 50 bar between $M_{0.5}$ -3.0 respectively. These values are consistent with what Wu et al. (2018) observed for injection induced events in Oklahoma for events $M < 3.0$.

On average the stress parameter from Alberta events follow the YA15 CENA models events having a depth of about 6 km. For this depth the stress dependence on magnitude is given by YA15 as:

$$\ln(\Delta\sigma) = 4.544 + \min[0, 0.229(\mathbf{M} - 5.0)]. \quad (4.16)$$

We determine the best near-surface attenuation parameter (κ_0) for Alberta through an iterative grid-search process. For each event we evaluate the magnitude scaling term; remove the reference κ term by subtracting the F_κ function evaluated at 0.025 s ($F_{\kappa_{0.025}}$); then evaluate the stress parameter function for a suite of logarithmically-spaced stress parameter values; and evaluate the κ function for linearly-spaced kappa terms, using:

$$E_{pred_{i,j}} = F_M + F_{\Delta\sigma,i} + F_{\kappa_j} - F_{\kappa_{0.025}} \quad (4.17)$$

By comparing the spectrum predicted by the event term $E_{pred_{i,j}}$ for each stress-kappa pair against the value determined for the event by the inversion, for frequencies from 0.90 Hz to 24.0 Hz, we determine the best fit stress-kappa pair for each event, as well as all pairs that fit above the 97.5th, 95th and 90th percentiles. This allows us to observe the acceptable range of stress-kappa pairs for each event and evaluate the trade-off between these two parameters. These two terms have a proportional relationship such that if one parameter is increased, the other follows. This is demonstrated in Figures 4.11-4.13. We next fix the stress parameter values for each event to match the model given by Equation 4.16 and grid search for the best mean kappa term. For the stress parameter values given in Equation 4.16, the corresponding κ_0 that best matches the observed event term to the model generally lies between 0.05 s and 0.07 s, as shown in Figure 4.14. Based on these analyses, we select a mean value of 0.06 s as the average regional kappa term for soil sites in Alberta.

There is a classic non-uniqueness issue in the resolution of $\Delta\sigma$ and κ . Our mean kappa of 0.06 is dependent on the assumed model of Equation (4.16) for the stress parameter. The stress parameter is ultimately a shape term that aims to bridge the offset between spectral amplitudes at low frequencies with those at high frequencies; however, the value of kappa also plays a critical role in this regard, as does any frequency-dependence in the

calibration factor. It is important to recognize that different self-consistent parameter sets exist (i.e. different combination of stress, kappa, and calibration factor) that would also satisfy the observational constraints and result in similar final GMPEs. As observed in Figures 11-13, there is a wide range of $\kappa - \Delta\sigma$ pairs that will provide a similar goodness of fit for each event. We attempted to provide some constraint on the problem by assuming the stress model of Yenier and Atkinson (2015b) as a basis for the kappa determination. However, if we were to circle back and re-compute the stress parameter values for each event after applying a kappa adjustment term for $\kappa = 0.06\text{s}$ to the Yenier and Atkinson source spectra, prior to taking the HF-LF measure, we would obtain higher corresponding stresses-and a more negative calibration constant. We performed this exercise, finding that it brings the stress parameter values up to those of the Yenier and Atkinson (2015b) stress parameter model for CENA evaluated at a focal depth of 8 km, and also results in a lower (more negative) calibration factor at high frequencies by about 0.13 natural logarithmic units; the resulting overall GMPE does not change significantly.

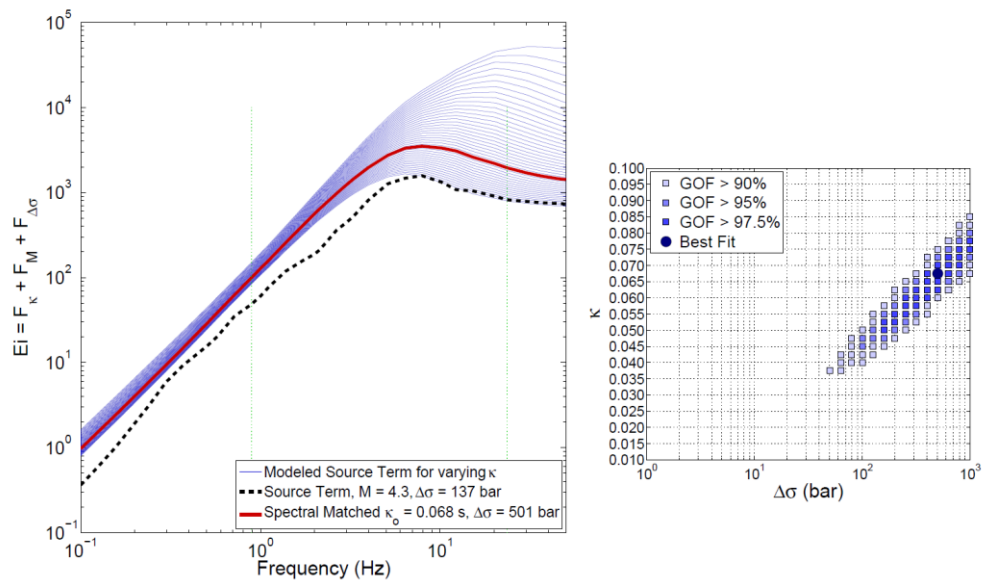


Figure 4.11: (Left) the dashed line shows the event source term; thin solid lines show the evaluated source term for linearly spaced κ values and best fit stress parameter value pair; thick solid line depicts best spectral matched κ for an events modeled stress parameter value. (Right) shows goodness of κ - $\Delta\sigma$ pair fits in the 90th, 95th and 97.5th percentiles.

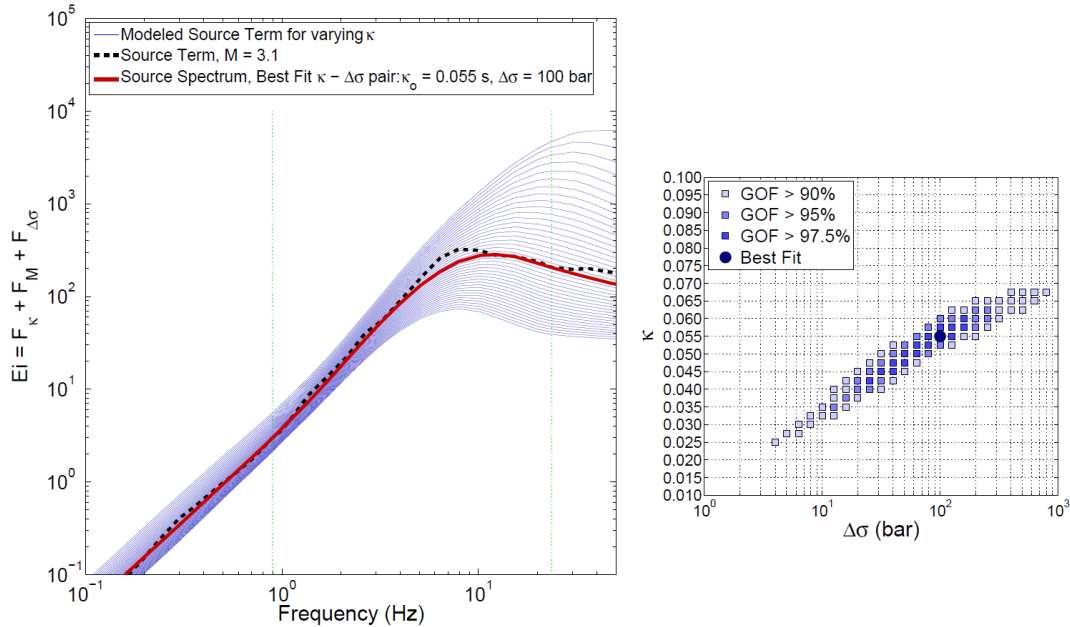


Figure 4.7: (Left) the dashed line shows the event source term; thin solid lines show the evaluated source term for linearly spaced κ values and best fit stress parameter value pair; thick solid line depicts best spectral matched κ for an events modeled stress parameter value. (Right) shows goodness of κ - $\Delta\sigma$ pair fits in the 90th, 95th and 97.5th percentiles.

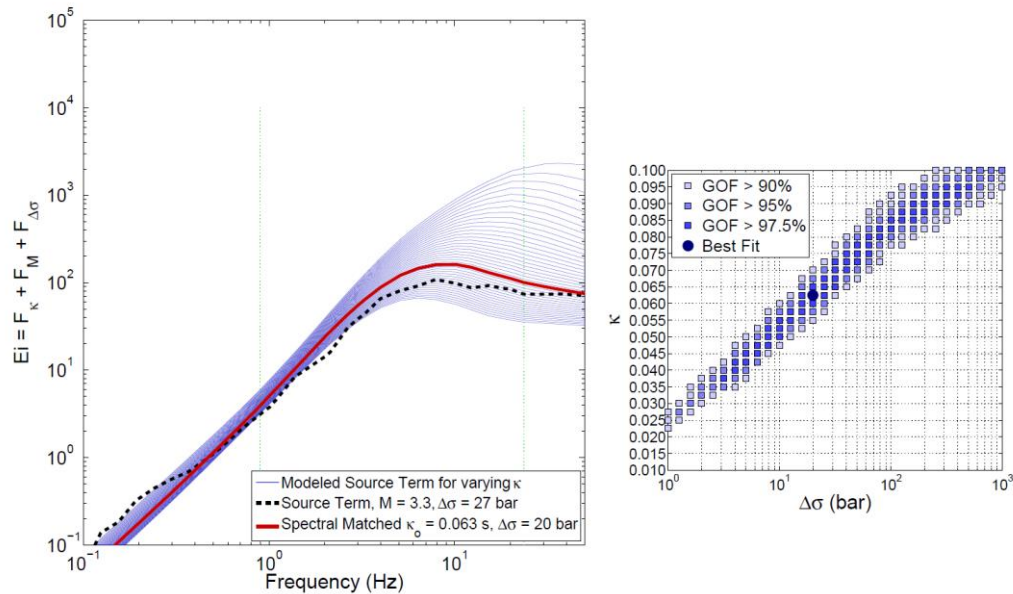


Figure 4.13: I(Left) the dashed line shows the event source term; thin solid lines show the evaluated source term for linearly spaced κ values and best fit stress parameter value pair; thick solid line depicts best spectral matched κ for an events modeled stress parameter value. (Right) shows goodness of κ - $\Delta\sigma$ pair fits in the 90th, 95th and 97.5th percentiles.

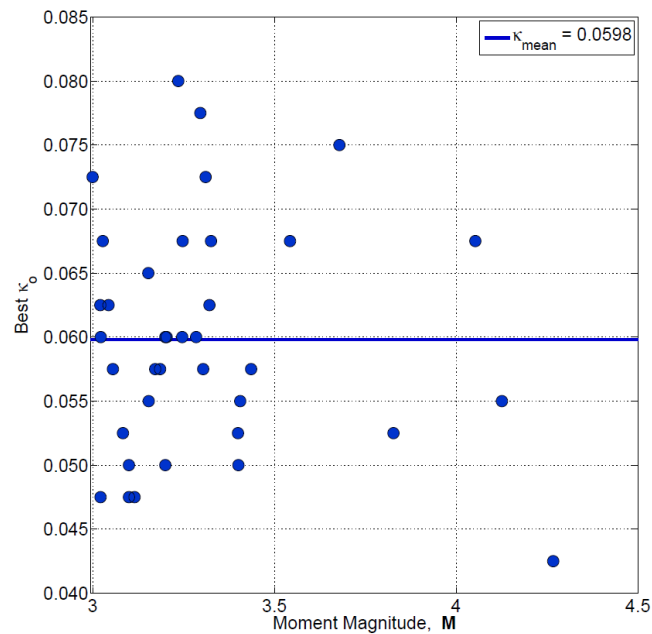


Figure 4.8: Kappa value that minimizes the residuals between the observed event term and predicted source term when the stress parameter is assigned based on Eqn (4.16). We chose not to implement a higher stress model, as we believe that the Yenier and Atkinson (2015b) stress parameter model is better constrained than what we can determine from these data. Moreover, it is known that the events are typically shallow, and the selected stress model should reflect this.

The regional calibration factor (C) is determined as the residual mismatch between the observations and the model (after considering the modeled stress parameter for each event, the site term for each station, and the regional kappa, geometric spreading and anelastic attenuation functions). As discussed in Yenier and Atkinson (2015a), the calibration factor reflects the average differences between the observations and the simulations, including any systematic factors that are not accurate or not included in the modeling approach. Examples of such factors include any residual regional site amplification effects relative to the assumed amplification model for B/C that was included in the Yenier and Atkinson (2015b) formulation, and any surface wave or other contributions to the motion that were not included in the Brune source model. Removing

the resolved parameters from the inversion from the ground motion observations, Equation 4.2 becomes

$$\ln(Y_{ij}) - F_{M,i} - F_{Z,ij} - \gamma_{AB}R_{ij} - F_{\Delta\sigma} - F_{S,j} - F_{\kappa_0} = C_{AB} + \eta_i + \varepsilon_{ij} \quad (4.18)$$

where C_{AB} is the regional calibration factor for Alberta, η_i is the between-event error, and ε_{ij} is the within-event error. Following Abrahamson and Youngs (1992), we use a mixed effects regression of residuals to solve Equation 4.18. An iterative regression is performed to maximize the likelihood of the model and estimate the regional calibration factor (C_{AB}). The residual error of the observations with respect to the model is separated into its between-event and within event components (η_i and ε_{ij}). The regional calibration factor for Alberta is shown in Figure 4.15 and is summarized in Appendix Table A4.2 along with the determined error components. A full list of model parameters, calibration factor and error components at all frequencies is given in Table S4.1 of the electronic supplement. At frequencies < 0.30 Hz we observe a positive residual of up to 0.5 ln units at 0.20 Hz. This is explained by microseismic contributions and inherent limitations of stochastic methods at low frequencies, which do not allow surface wave phases or coherent pulses to be properly modeled. We suggest using a constant value of 0 at $f < 0.2$ Hz to prevent mapping the micro seismic peak at low frequencies to larger magnitudes. The calibration factor dips steadily from 0 to -0.5 ln units between 0.2 Hz to 2.23 Hz where it remains relatively constant to 50.0 Hz. A suggested calibration factor model for Alberta is given by:

$$C_{AB} = \begin{cases} 0 & \text{for } f < 0.3 \text{ Hz} \\ -0.69 \log_{10}(f) - 0.36 & \text{for } 0.2 \text{ Hz} \leq f < 1.59 \text{ Hz} \\ -0.50 & \text{for } f \geq 1.59 \text{ Hz} \\ -0.39 & \text{for PGV} \\ -0.36 & \text{for PGA} \end{cases} \quad (4.19)$$

The shape of the calibration function at intermediate frequencies might reflect deviations from the regional site response model assumed for the reference B/C condition. The generic GMPE form upon which this study is based has embedded within it a prescribed average crustal amplification function for B/C conditions, which was derived from an assumed model (Atkinson and Boore, 2006).

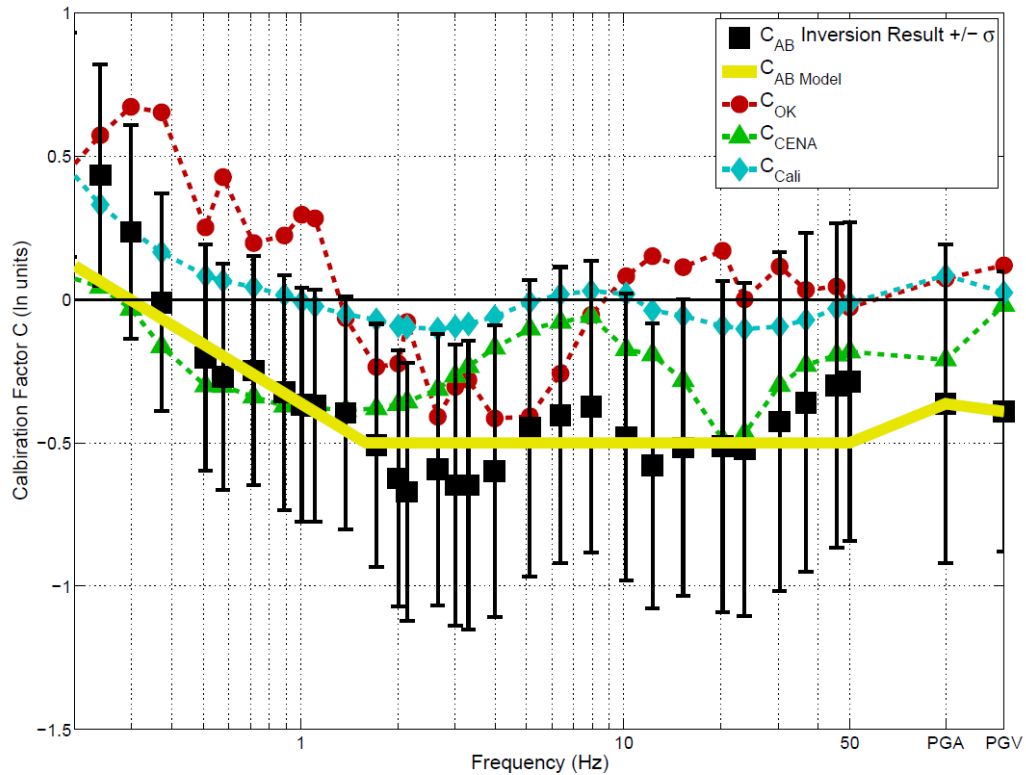


Figure 4.9: Calibration factor (C_{AB}) obtained from inversion (squares) and its standard deviation (error bars). Heavy line shows suggested model function for C_{AB} . Corresponding calibration factors for other regions are shown for comparison (lines with symbols; circles=Oklahoma; triangle=CENA; diamond=California).

Any differences between the average amplification factors for selected B/C reference sites in Alberta and those in the assumed embedded model will map into the calibration factor. As shown in Figure 4.16, we may interpret the inverse of the calibration factor as the amplification of the reference sites (on average), relative to the assumed amplification function for B/C. By this logic, we may infer that the reference sites might have an amplification that is larger than that assumed by Yenier and Atkinson (2015b) for B/C sites, and more peaked at intermediate frequencies. We also note that Alberta ground motions present relatively low amplitudes at high frequencies, which could reflect deviations from the assumed crustal amplification model used in the base model simulations of Yenier and Atkinson (2015b).

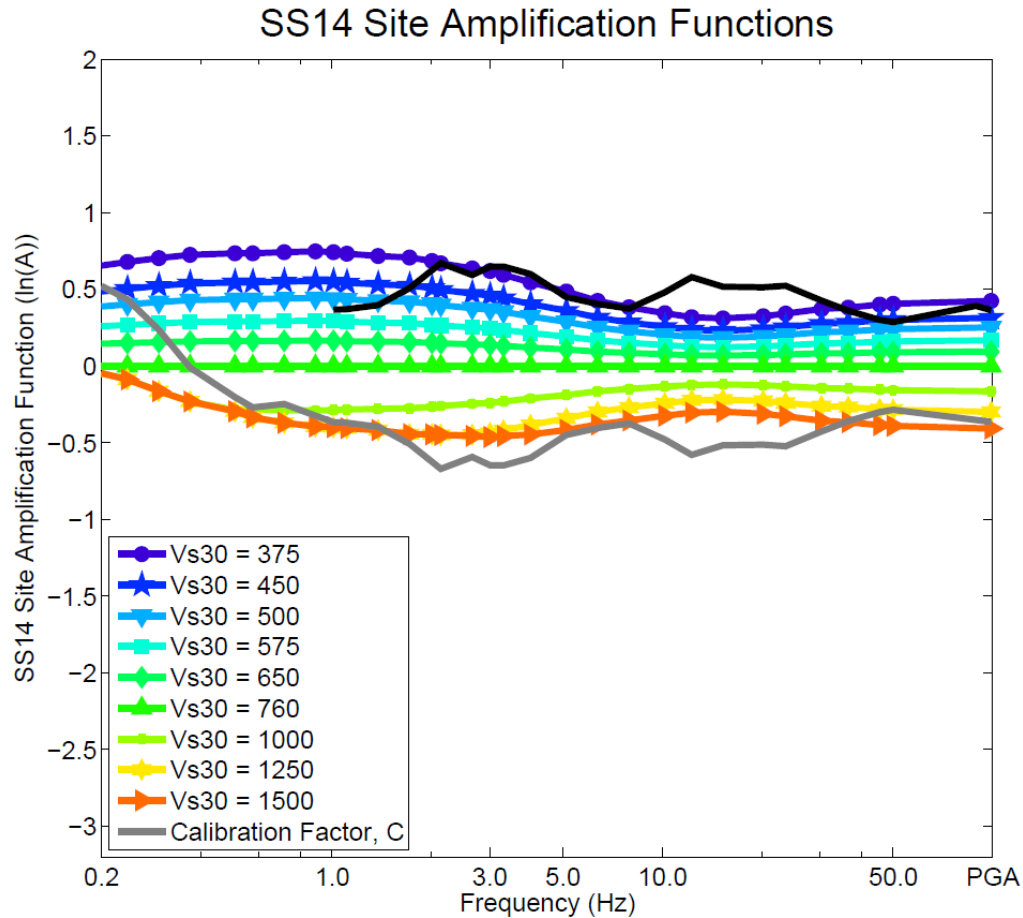


Figure 4.10: The Alberta calibration factor (light line) and its inverse (black line), in comparison to the site amplification functions of Seyhan and Stewart (2014; SS14) for California, for a range of V_{s30} values (lines with symbols).

The trilinear geometric spreading function developed in this study agrees with that developed for an improved local magnitude equation from a private ground motion database in the Western Canadian Sedimentary Basin (Yenier, 2017). The differences in geometric spreading functions from the bilinear equations previously used in magnitude relationships in the region suggests an updated study should be undertaken to adjust the moment magnitude estimation equations to incorporate these attenuation effects. Alternatively, moment magnitudes could be estimated from stations within 50 km to minimize the effects of attenuation.

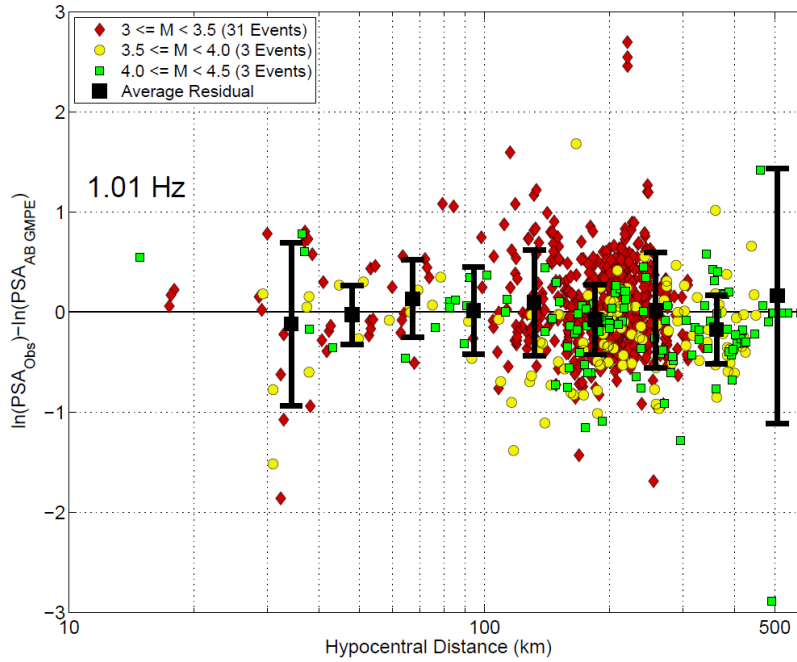


Figure 4.11. Within event residuals with respect to the final GMPE for PSA at 1.01 Hz. Black squares and error bars depict the mean residual and its standard deviation in logarithmically spaced distance bins.

The final GMPE for Alberta includes the assumed magnitude scaling and geometric spreading functions, the derived model for the anelastic attenuation terms, stress parameter, site amplification terms, and the empirical calibration factor, and is described as:

$$\ln(Y_{ij}) = F_M + F_{\Delta\sigma,AB} + F_Z + F_\gamma + F_S + F_{k_0} + C_{AB} \quad (4.20)$$

where the coefficients for all terms are summarized in Appendix Table A4.3 and fully listed in Table S4.1 of the electronic supplement. The electronic supplement also provides a spreadsheet for evaluating the function. In Figures 4.17 and 4.18 we plot the within-event residuals ($\varepsilon = \ln(\text{observed}) - \ln(\text{predicted})$) for the horizontal-component (geometric mean) PSA at 1.01 Hz and 10.17 Hz. There are no significant trends in the residuals in magnitude or distance, for hypocentral distances greater than 50 km; at closer distances, there is a tendency towards slightly positive residuals at some frequencies, and slightly negative at others. In figure 4.19 the between event residuals (η) are plotted as a

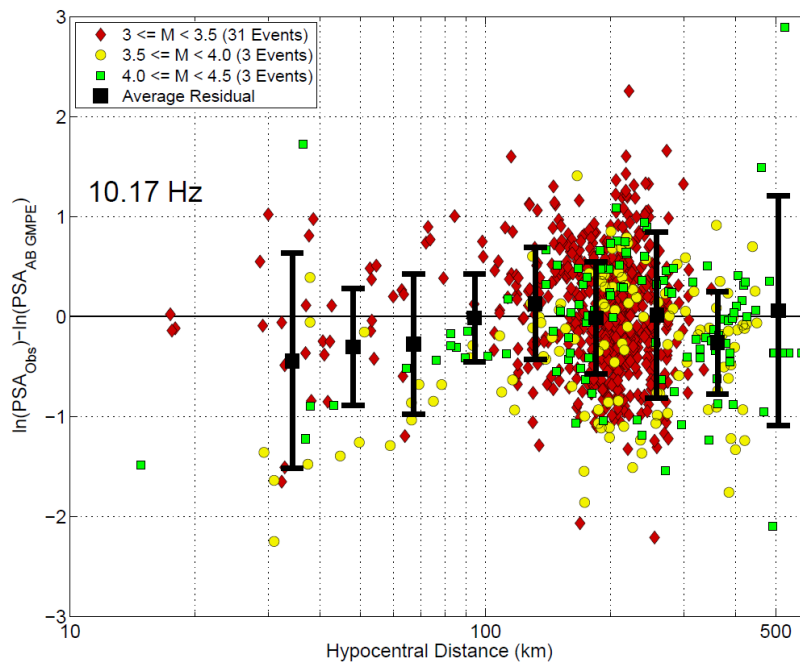


Figure 4.12. Within event residuals with respect to the final GMPE for PSA at 10.17 Hz. Black squares and error bars depict the mean residual and its standard deviation in logarithmically spaced distance bins.

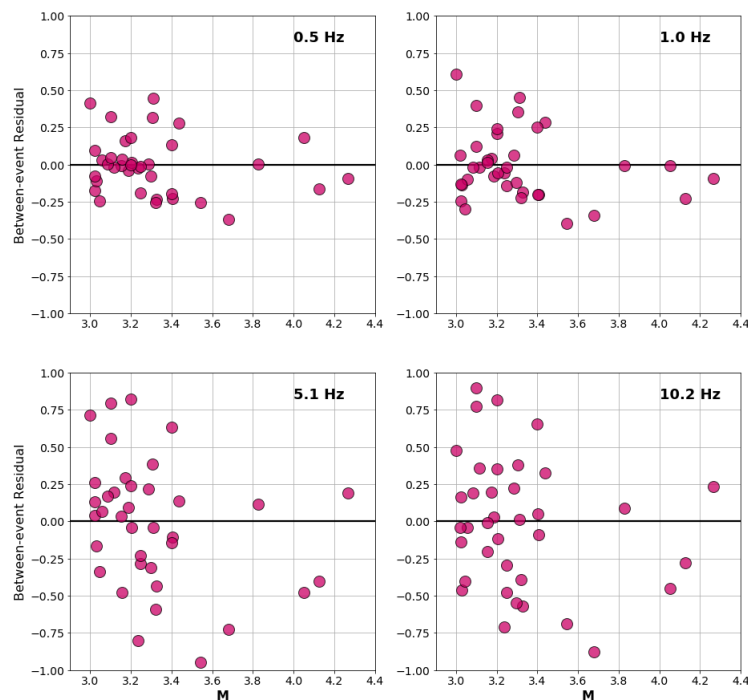


Figure 4.19: Between-event residuals as a function of moment magnitude at 0.5 Hz, 1.0 Hz, 5.1 Hz and 10.2 Hz.

function of magnitude and do not display any meaningful trend with magnitude, though, there is a tendency towards greater variability at high frequencies. Figure 4.20 shows the between-event residual as a function of stress parameter. At high frequency ground motion is controlled by the stress parameter. The adopted stress parameter model under predicted stress for some study events in the ranges of M 3-3.2 and over predicted for some events of M 3.2-3.4. As a result, we observe a strong trend in the between-event variability as a function of stress parameter, which is expected due to the limitations of predictive power in the adopted stress parameter model.

Figure 4.21 demonstrates the final GMPE (for PSA at 1.0 Hz), overlaying site-corrected observations. As expected from the residual plots, observations follow the GMPE well. In Figure 4.22, we compare the GMPE for induced events in Alberta, at selected frequencies, to: the Oklahoma GMPE of NAA18 evaluated at the mean focal depth of induced events in Oklahoma of 5 km; the CENA GMPE of Yenier and Atkinson (2015b) for earthquakes at depths of 2 and 5 km, for events of M 3 and M 5, respectively; and the GMPE of Atkinson (2015), which was derived from moderate events with an average depth of 9 km in California (NGA-West2 database), but postulated to apply for induced events, is also shown.

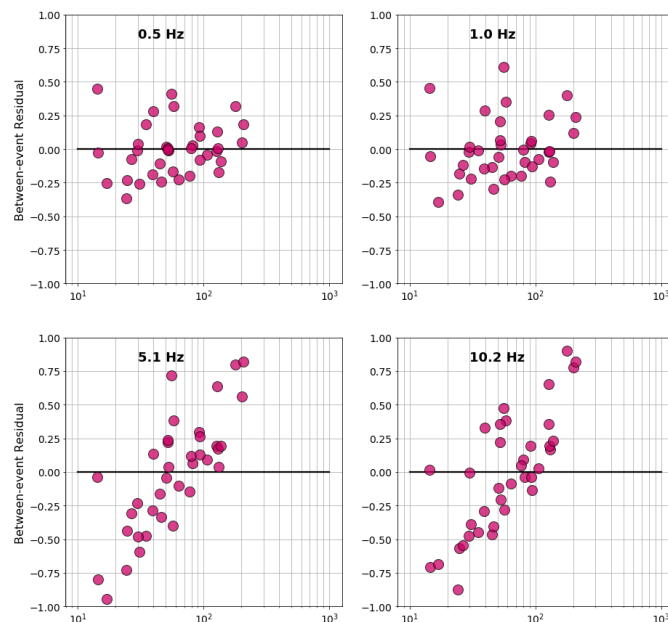


Figure 4.20: Between-event residuals as a function of stress parameter (bar) at 0.5 Hz, 1.00 Hz, 5.0 Hz and 10.0 Hz.

For low-to-intermediate frequencies the tri-linear geometric spreading function generally traces the level of YA15 and Atkinson (2015) where the GMPE predicts slightly lower amplitudes near the first transition and slightly higher near the second transition zone. At higher frequencies the GMPE derived for Alberta is generally low for near to intermediate distances (<150 km) and matches the level at far distances when compared to YA15 and Atkinson (2015). Alberta ground motion amplitudes are generally lower than those observed in Oklahoma, especially at high frequencies (> 10 Hz). Differences of amplitude in the Alberta and Oklahoma GMPEs reflect the differences in stress parameter models. Alberta events appear to follow the CENA model of YA15 evaluated at 6 km depth, whereas in Oklahoma the derived model (involving both depth and magnitude) features higher stress parameters. This could reflect generally greater depths for induced events in Oklahoma, or some other differences attributable to source processes. Differences in average regional crustal amplification may also contribute to the difference in observations as these will map into the source terms.

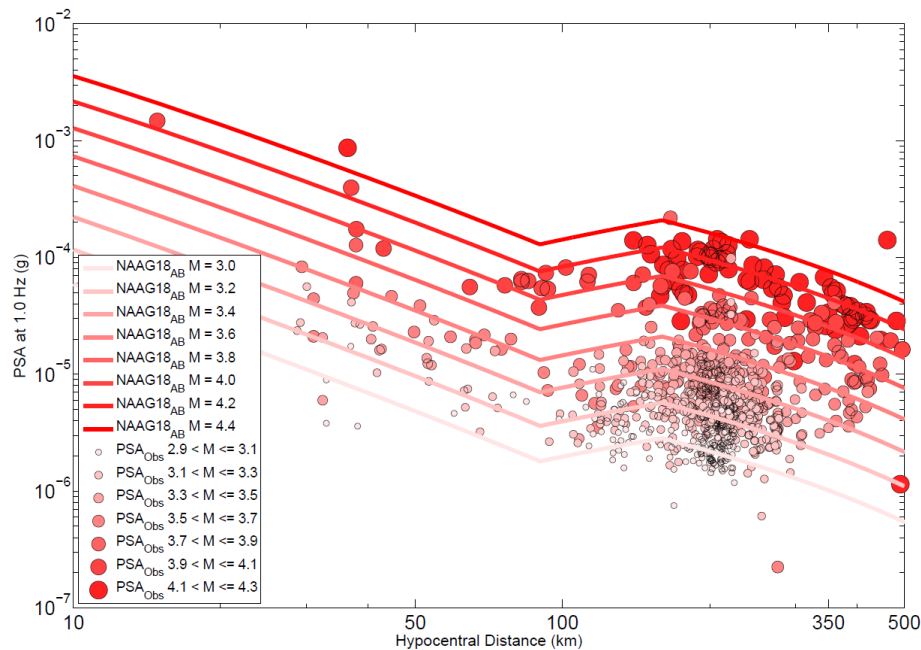


Figure 4.21 Final GMPE overlaying site corrected observations at 1.0 Hz. Lines depict the GMPE evaluated every 0.2 magnitude units from $M = 2.9$ to $M = 4.5$. Circles vary in diameter where larger circles represent higher magnitude observations and smaller circles denote lower magnitude event observations.

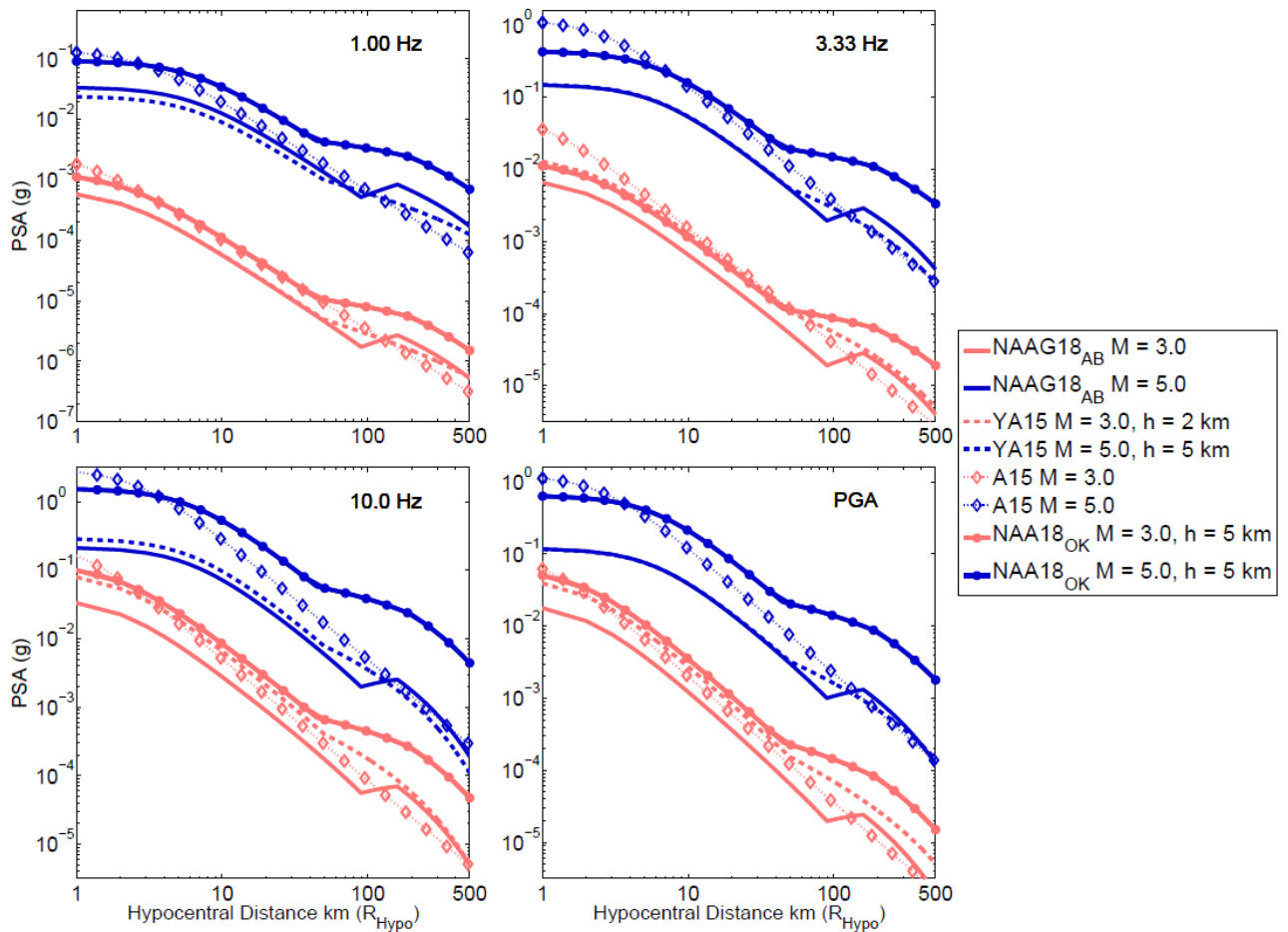


Figure 4.22. The GMPE for Alberta as determined in this study (solid lines) in comparison to the NAA18 GMPE for Oklahoma (circles) is evaluated at the typical focal depth for events in Oklahoma of 5 km. YA15 GMPE for CENA (dashed lines) is evaluated for focal depths of 6 and 8 km for M_4 and M_6 respectively. The GMPE of Atkinson (2015), as determined from moderate California earthquakes with mean depth of 9 km, is also indicated (dotted lines), for distances < 50 km. All models are for NEHRP B/C reference site conditions.

4.6 Conclusion

A regionally-adjusted GMPE for induced events in Alberta is developed that describes the geometric mean of horizontal component PSA, PGV, and PGA ground motions for a

reference condition of B/C. The generic GMPE framework of Yenier and Atkinson (2015b) is used to ensure stable scaling of motions over all magnitudes and distances. We calibrate the generic GMPE by determining site amplification models, anelastic attenuation function, regional stress parameter model, regional near surface high frequency attenuation term (adapted from Hassani and Atkinson 2018), and calibration factor from > 880 ground-motion observations from Alberta events of $M \geq 3$ at hypocentral distances from 20 to 575 km. The derived GMPE is useful for ShakeMap applications, hazard assessments and may also be useful for ground-motion-based alerting systems and traffic light protocols.

4.7 Data and Resources

Events were detected and located for TransAlta by Nanometrics. Ground motion data were downloaded from the Incorporated Research Institutes for Seismology (www.iris.edu, last accessed Oct. 2017), processed, and compiled using an updated version of the ICORRECT algorithm, as described in Assatourians and Atkinson (2017). A ground motion database paper composed of processed ground motion observations, event/station metadata and M estimates for each event will become available online in the near future.

4.8 Acknowledgements

This study was funded by the Natural Sciences and Engineering Research Council of Canada and TransAlta. We thank Joseph Farrugia for his valuable input and interpretation of site classifications. We thank Emrah Yenier for his suggestions which strengthened the manuscript. We thank our reviewers for their constructive feedback.

4.9 References

- Abrahamson, N. A., and R. R. Youngs (1992). A stable Algorithm for regression analysis using the random effects model, *Bull. Seismol. Soc. Am.* 82(1), 505–510.
- Ambraseys, N. N., and Douglas, J. (2004). Magnitude calibration of north Indian earthquakes. *Geophysical Journal International*, 159(1), 165-206. DOI: 10.1111/j.1365-246X.2004.02323.x

- Anderson, J. G., and Hough S. E. (1984). A model for the shape of the Fourier amplitude spectrum of acceleration at high frequencies, *Bull. Seismol. Soc. Am.* 74, 1969 – 1993.
- Andrews, J. (1986). Objective determination of source parameters and similarity of earthquakes of different size, *Earthquake Source Mechanics*, American Geophysical Union, *Geophysical Monograph*, 37, 259-267.
- Assatourians, K., and Atkinson, G. M. (2010). Database of processed time series and response spectra for Canada: An example application to study of the 2005 MN 5.4 Riviere du Loup, Quebec earthquake, *Seismol. Res. Lett.* 81(6), 1013–1031.
- Assatourians, K., and Atkinson, G. M. (2017). Are Ground-Motion Models Derived from Natural Events Applicable to the Estimation of Expected Motions for Induced Earthquakes? *Seism. Res. Lett.* DOI: 10.1785/0220160153.
- Atkinson, G. M. and Boore D. M. (2006). Earthquake ground-motion prediction equations for eastern North America, *Bull. Seism. Soc. Am.* 85, 17-30.
- Atkinson, G. M., Greig, W., and Yenier, E. (2014). Estimation of Moment Magnitude (M) for Small Events ($M < 4$) on Local Networks. *Seismological Research Letters*, **85**, 1116-1124.
- Atkinson, G. M., Hassani, B., Singh, A., Yenier, E. and Assatourians, K. (2015). Estimation of Moment Magnitude and Stress Parameter from ShakeMap Ground-Motion Parameters. *Bull. Seismol. Soc. Am.* 105(5), 2572-2588.
- Atkinson, G. M., and Morrison, M. (2009). Regional variability in ground motion amplitudes along the west coast of North America, *Bull. Seismol. Soc. Am.*, 99, 2393–2409.
- Boore, D. M. (2003). Simulation of ground motion using the stochastic method, *Pure and Applied Geophysics* **160**, 635-675.
- Boore, D. M. (2010). Orientation-Independent, Nongeometric-Mean Measures of Seismic Intensity from Two Horizontal Components of Motion. *Bull. Seismol. Soc. Am.* **100**, 1830-1835.
- Boore, D. M., Campbell, K. W., and Atkinson, G. M. (2010). Determination of stress parameters for eight well-recorded earthquakes in eastern North America. *Bull. Seismol. Soc. Am.* 100, 1632-1645.
- Bouzidi Y., Schmitt D. R., Burwash R. A., Kanasewich E. R. (2002). Variations in Crustal Thickness in Alberta from Depth-Migrated Seismic Reflection Profiles, *Can. J. Earth. Sci.*, 39, 311-350.

- Brune, J. N. (1970). Tectonic stress and the spectra of seismic shear waves from earthquakes. *J. Geophys. Res.* 75(26), 4997-5009.
- Brune, J. N. (1971). Correction: Tectonic stress and the spectra of seismic shear waves, *J. Geophys. Res.* 76(20), 5002.
- Burger, R. W., Somerville, P. G., Barker, J. S., Herrmann, R.B., and Helmberger, D.V. (1987). The effect of Crustal structure on strong ground motion attenuation relations in eastern North America. *Bull. Seismol. Soc. Am.* 77, 420-439, 1987.
- Cramer, C. (2017). Brune Stress Parameter Estimates for the 2016 M_w Pawnee and Other Oklahoma Earthquakes. *Seismological Research Letters*, 88(4):1005-1016.
- Cramer, C. (2017). Gulf Coast Regional Q and Boundaries from USArray Data. *Bull. Seismol. Soc. Am.* 108(1), 437-449
- Ellsworth, W. L. (2013). Injection-induced earthquakes. *Science*. 341 (6142): 7.
DOI:10.1126/science.1225942
- Farrugia, J. J., Atkinson, G. M., Molnar, S. (2017). Validation of 1D Earthquake Site Characterization Methods with Observed Earthquake Site Amplification in Alberta, Canada. *Bull. Seismol. Soc. Am.* 108 (1): 291-308.
- Fereidoni A., Atkinson G.M. (2017), Discriminating Earthquakes from Quarry Blasts Based on ShakeMap Ground-Motion Parameters, *Bull. Seismol. Soc. Am.*, DOI:10.1785/0120160308.
- Ghofrani H. and Atkinson G. M. (2014). Site Condition Evaluation Using Horizontal-to-Vertical Response Spectral Ratios of Earthquakes in the NGA-West2 and Japanese Databases. *Soil Dynamics and Earthquake Engineering*. 67, 30-43.
- Goertz-Allmann, B. P., Goertz, A., Wiemer, S. (2011). Stress drop variations of induced earthquakes at the Basel geothermal site. *Geophysical Research Letters*, 38, L09308, doi:10.1029/2011GL047498
- Gu Y., Okeler A., Shen L., Contenti S. (2011). The Canadian Rockies and Alberta Network (CRANE): New Constraints on the Rockies and Western Canadian Sedimentary Basin. *Seismological Research Letters* 82(4), 575-588.
- Hassani, B., and Atkinson, G. M. (2015). Referenced empirical ground-motion model for Eastern North America. *Seismological Research Letters* 86(2A), 477-491.
- Hassani, B. and Atkinson, G. M. (2016). Site-effects model for central and eastern North America based on peak frequency. *Bull. Seism. Soc. Am.*, **106**, 2197-2213.

- Hassani, B., and Atkinson G. M. (2018). Adjustable Generic Ground-Motion Prediction Equation Based on Equivalent Point-Source Simulations: Accounting for Kappa Effects. *Bull. Seismol. Soc. Am.* 108(2), 913-928.
- Huang, Y., Ellsworth, W. L., and Beroza, G. C. (2017). Stress drops of induced and tectonic earthquakes in the central United States are indistinguishable. *Science Advances* 3(8), e1700772.
- McGuire, R. K. (2004). *Seismic Hazard and Risk Analysis*, Earthquake Engineering Research Institute. Aug 1, 2004.
- Nigam, N. C. and Jennings, P. C. (1969). Calculation of Response Spectra from Strong-Motion Earthquake Records, *Bull. Seismol. Soc. Am.* 59(2), 909-922.
- Novakovic M., Atkinson G. M. (2015). Preliminary Evaluation of Ground Motions from Earthquakes in Alberta. *Seismol. Res. Lett.*, 86(4), 1086-1095.
- Novakovic M., Atkinson G. M., Assatourians K. (2018). Empirically Calibrated Ground-Motion Prediction Equation for Oklahoma. *Bull. Seismol. Soc. Am.* DOI: 10.1785/0120170331
- Schultz, R., Wang, R., Gu, Y., Haug, K., Atkinson, G.M. (2017) A Seismological Overview of the Induced Earthquakes in the Duvernay Play Near Fox Creek, Alberta. *Journal of Geophysical Research: Solid Earth*, 122(1), 492-505.
- Seyhan, E. and Stewart, J. (2014). Semi-Empirical Nonlinear Site Amplification from NGA-West2 Data and Simulations. *Earthquake Spectra*, 30(3), 1241-1256.
- Stern, V. H., Schultz, R. J., Shen, L., Gu, Y. J. and Eaton, D. W. (2018): Alberta earthquake catalogue, version 6.0 (GIS data, point features); Alberta Energy Regulator, AER/AGS Digital Dataset 2013-0017.
- Wald D. J., Quitoriano V., Heaton T. H., Kanamori H., Scrivner C. W., Worden C. B. (1999). TriNet ShakeMaps: Rapid generation of peak ground motion and intensity maps for earthquakes in southern California. *Earthq. Spectra*. 15(3), 537-555.
- Wang, R., Gu., Y, Schultz, R., Kim A., Atkinson, G. M. (2015), Source Analysis of a Potential Hydraulic-Fracturing-Induced Earthquake Near Fox Creek, Alberta. *Geophysical Research Letters*, DOI: 10.1002/2015GL066917.
- Wang, R., Gu, Y. J., Schultz, R., Zhang, M., and Kim, A. (2017). Source characteristics and geological implications of the January 2016 induced earthquake swarm near Crooked Lake, Alberta. *Geophysical Journal International*, 210(2), 979-988.
- Wu, Q., Chapman, M., Chen, X. (2018). Stress-Drop Variations of Induced Earthquakes in Oklahoma. *Bull. Seismol. Soc. Am.* 108 (3A), 1107-1123.

- Yenier, E., and Atkinson, G. M. (2014). Equivalent point-source modeling of moderate to large magnitude earthquakes and associated ground-motion saturation effects. *Bull. Seismol. Soc. Am.* 104, 1458-1478.
- Yenier, E., and Atkinson, G. M. (2015a). An Equivalent Point-Source Model for Stochastic Simulation of Earthquake Ground Motions in California. *Bull. Seismol. Soc. Am.* 105(3), 1435-1455.
- Yenier, E., and Atkinson, G. M. (2015b). Regionally-Adjustable Generic Ground-Motion Prediction Equation based on Equivalent Point-Source Simulations: Application to Central and Eastern North America. *Bull. Seismol. Soc. Am.* DOI: 10.1785/0120140332
- Yenier, E., Atkinson G. M., Sumy D. F. (2017). Ground Motions for Induced Earthquakes in Oklahoma, *Bull. Seismol. Soc. Am.* 107(1), 198-215
- Yenier, E. (2017). A Local Magnitude Relation for Earthquakes in the Western Canadian Sedimentary Basin, *Bull. Seismol. Soc. Am.* DOI: 10.1785/0120160275

Chapter 5

5 Conclusions and Future Studies

5.1 Summary, Discussion and Conclusions

In this thesis we characterized ground motions from induced earthquakes in Oklahoma, USA and Alberta, Canada.

In Chapter 2 we estimate the moment magnitude of events in Alberta using the PSA-based algorithm of Atkinson et al. (2014). We found that the attenuation and amplitude calibration parameters for WNA provide a consistent agreement with local magnitude calculations for events $M > 2.6$. The deviation of moment magnitude and local magnitude for $M < 2.6$ was initially postulated as a noise effect, and a noise correction was suggested. Since that study was conducted, the relationship between local magnitude and moment magnitude has become better understood, and it is now believed that this correction factor should be discarded (Ross et al., 2016; Yenier, 2017). The Wood-Anderson filter that is applied to seismograms in determining local magnitude can explain the observed deviation (Bakun, 1984; Hanks and Boore, 1984). Amplitudes of larger events are artificially lowered more than those of smaller events as the Wood-Anderson filter has a corner frequency of roughly 1.00 Hz. There exists a discontinuity between M estimated from PSA at 1.00 Hz and M estimated at 3.33 Hz, that can be bridged by taking the mean of these two values if each parameter lies on opposite sides of $M=3$. Ground motions are compared to a reference model of Atkinson (2015) and are found to be generally consistent with those for similar-size events in California in terms of overall amplitude level and attenuation. We observed features in this comparison that were unresolvable with the sparse available data, which will require further investigation with additional ground-motion records. Ground motion scaling characteristics of Alberta events are generally consistent with expectations based on both empirical (Atkinson, 2015) and point-source simulation models (Yenier and Atkinson, 2015a). We observe a significant site response on the horizontal component in the 2 to 5 Hz frequency range,

which is relatively consistent among all stations. This suggests a relatively common site response model could be appropriate for all stations in Western Alberta.

In Chapter 3, we derived a regionally-adjusted GMPE for induced events in Oklahoma (geometric mean of horizontal components), for a reference condition of B/C. We used the generic GMPE framework of Yenier and Atkinson (2015b) to ensure stable scaling of motions over all magnitudes and distances. Observations of ground motion amplification at regional distances due to the summation of direct rays and the first post critically refracted waves off of the Mohorivicic discontinuity dictated the need for the development of a tri-linear geometric spread model. Yenier and Atkinson (2015b) base the stress parameter value on the corner frequency by matching the attenuation-corrected spectral shape to that of an ideal Brune spectra. On average the Oklahoma source spectra do not nicely follow the ideal Brune-model spectral shape, so an alternative approach was considered in this study that bases the determination of the stress parameter on the event's mean high-frequency spectral level (10 Hz level) relative to that expected based on the low-frequency level (1 Hz level). This approach was found to result in more stable determination of the stress parameter. The generic GMPE was calibrated by determining an anelastic attenuation function, site amplification models, regional stress parameter model, and calibration factor. The derived GMPE presents higher ground motions at high frequencies than those observed in CENA (for the same magnitude and distance), which reflect differences in magnitude and depth dependence of the stress parameter. At low frequencies the amplitudes in Oklahoma tend to be higher than those for corresponding events in CENA, suggesting differences in the crustal amplification effects due to regional geology. The derived GMPE is useful for hazard assessments and ShakeMap applications and may also be useful for ground-motion-based alerting systems and traffic light protocols.

In Chapter 4, we empirically calibrated the regionally adjustable GMPE (Yenier and Atkinson, 2015b) for induced events in Alberta. Similar to Oklahoma, we observed strong influences of Mohorivicic bounce effects and model ground motion attenuation at regional distances with a trilinear geometric spreading function. We discovered that the spectral shape of attenuation corrected event spectra has significantly lower amplitudes at

high frequency than those expected for an ideal Brune source. We attribute this to a combination of differing crustal amplification in the region as well as differing near-surface attenuation effects (commonly expressed as the kappa effect, κ_0) relative to those assumed in the simulations of the reference model. Yenier and Atkinson (2015b) assumed a kappa value of 0.025 s in the simulations upon which their model was based. Hassani and Atkinson (2018) showed how this model could be adjusted for alternative values of kappa. We adapt the functional form of the kappa effect from Hassani and Atkinson (2018) and develop a referenced kappa adjustment factor. We perform grid search analysis to determine that the best choice in kappa for Alberta is 0.06 s, as a regional average for the seismographic recording sites. If the source scaling of the events can be constrained, this would reduce the trade-offs between stress and kappa, and allow a less-ambiguous definition of the ground-motion model parameters. Overall, the ground motions for B/C site conditions for induced events in Alberta are of similar amplitude at low frequencies to those predicted by the GMPEs of Yenier and Atkinson (2015b) and Atkinson et al (2015), for events of M 3 to 4.5. Alberta motions present lower amplitudes at high frequencies than those observed in Oklahoma but are fairly consistent with the model of Yenier and Atkinson (2015b) for very shallow events in CENA.

Through the process of these studies we concluded that it is not entirely straight forward to calibrate the generic GMPE to a regional database in a unique and unambiguous way.

5.2 Recommendations for Future Studies

Based on the requirement of a trilinear geometric spreading function in Chapter 4, the moment magnitude estimation equation should be revisited to incorporate the updated function shape. Re-evaluation of the frequency-dependent magnitude calibration factor should be adjusted in agreement with available moment tensor solutions in the region. This would facilitate routine, rapid and accurate estimation of moment magnitude for all events in CENA of $M > 2.5$, and would be helpful for real-time hazard assessment, alerting and traffic-light applications.

In our generic ground-motion model, disparities between assumed seismological models and the true physical characteristics are cast into a frequency-dependent calibration

factor. The fact that this calibration factor is not close to zero at all frequencies suggests the need for additional in-depth studies to refine the underlying geological and geophysical model parameters. One such parameter is the crustal amplification model, which to date has been based on a gradient model. The crustal structure in areas containing sedimentary basins might be better expressed as a ‘layer cake’ model. The effects of alternative crustal amplifications based on more realistic earth models should be explored in further studies. The interplay between amplification effects through the crustal structure and near-surface velocity profile, and near-surface damping (as expressed by kappa) also requires further study. It appears that such effects may be quite different in the Western Canadian Sedimentary Basin in comparison to those in Oklahoma or in CENA. Finally, the scaling of source attributes for induced events relative to those of natural earthquakes is a fruitful area for further detailed investigations.

5.3 References

- Atkinson, G. M. (2015). Ground-Motion Prediction Equation for Small-to-Moderate Events at Short Hypocentral Distances, with Application to Induced-Seismicity Hazards. *Bull. Seismol. Soc. Am.* 105. 10.1785/0120140142.
- Atkinson, G. M., Greig, W., and Yenier, E. (2014). Estimation of Moment Magnitude (M) for Small Events ($M < 4$) on Local Networks. *Seismol. Res. Lett.*, **85**, 1116-1124.
- Bakun, W.H. (1984). Seismic Moments, Local Magnitudes, and Coda-duration Prospects. *Bull. Seismol. Soc. Am.* 74, 439-458.
- Hanks, T.C. and Boore, D.M. (1984). Moment-magnitude Relations in Theory and Practice. *J. Geophys. Res.*, 89, 6229-6235.
- Hassani B., and Atkinson G. M. (2018). Adjustable Generic Ground-Motion Prediction Equation Based on Equivalent Point-Source Simulations: Accounting for Kappa Effects. *Bull. Seismol. Soc. Am.* 108(2), 913-928.
- Ross, Z.E., and Ben-Zion, Y. (2016). Towards Reliable Automated Estimates of Earthquake Source Parameters from Body Wave Spectra. *J. Geophys. Res.*, 121, doi:10.1002/2016JB013003.
- Yenier, E., and Atkinson, G. M. (2015a). An Equivalent Point-Source Model for Stochastic Simulation of Earthquake Ground Motions in California. *Bull. Seismol. Soc. Am.* 105(3), 1435-1455.

Yenier, E., and Atkinson, G. M. (2015b). Regionally-Adjustable Generic Ground-Motion Prediction Equation based on Equivalent Point-Source Simulations: Application to Central and Eastern North America. *Bull. Seismol. Soc. Am.* DOI: 10.1785/0120140332

Yenier, E. (2017). A Local Magnitude Relation for Earthquakes in the Western Canada Sedimentary Basin. *Bull. Seismol. Soc. Am.* 107. 10.1785/0120160275.

Appendices

Table A3.1: Tabulation of magnitude estimation model parameters where MC_F is the calibration factor for each frequency that aims to match the level that has been modified from Novakovic and Atkinson (2015) for Oklahoma. $\gamma_{F, low}$ (Eastern), $\gamma_{F, mod}$ (moderate), and $\gamma_{F, high}$ (Western) are the anelastic attenuation coefficients designed to remove distance dependent trends.

	3.33 Hz	1.00 Hz	0.30 Hz
MC_F	-3.3	-4.5	-5.45
$\gamma_{F, low}$	0.0015	0.0007	0.0011
$\gamma_{F, mod}$	0.0033	0.0021	0.0017
$\gamma_{F, high}$	0.0050	0.0035	0.0027

Table A3.2: Summary table of stress parameter values from inversion for events of $M \geq 4.2$ in Oklahoma.

Event Number	Date (mm/dd/yyyy)	Time (hh:mm:ss) UTC	Longitude	Latitude	Depth (km)	Magnitude, M	Stress Parameter, $\Delta\sigma$ (bar)
7	2/28/2011	05:00:50	-92.344	35.265	3.8	4.2	64.0
12	11/5/2011	07:12:45	-96.781	35.538	3.4	4.6	99.0
13	11/8/2011	02:46:57	-96.786	35.518	4.81	4.6	103.6
16	12/7/2013	18:08:06	-97.383	35.609	6.5	4.2	90.8
17	12/7/2013	18:10:25	-97.386	35.607	8.44	4.3	110.2
36	6/16/2014	10:47:36	-97.397	35.593	5	4.2	71.5
46	7/29/2014	02:46:36	-98.045	36.756	5.29	4.2	93.2
48	8/19/2014	12:41:36	-97.468	35.773	4.51	4.2	57.0
57	10/2/2014	18:01:24	-97.955	37.245	5	4.5	78.7
58	10/2/2014	18:02:55	-97.967	37.233	5	4.2	44.4
64	11/12/2014	21:37:11	-97.602	36.648	5.37	4.6	52.0
65	11/12/2014	21:40:01	-97.621	37.271	4.03	4.8	56.6
100	4/4/2015	13:21:17	-97.572	36.118	5.05	4.2	67.6
117	6/5/2015	23:12:41	-97.968	37.219	5.11	4.2	40.3
118	6/5/2015	23:12:47	-97.921	37.265	2.35	4.3	49.1
133	7/20/2015	20:19:04	-98.257	36.843	4.08	4.6	92.9

138	7/27/2015	18:08:39	-98.791	36.472	5	4.4	235.2
139	7/27/2015	18:12:15	-97.572	35.989	5	4.5	128.5
146	9/16/2015	02:30:02	-96.795	35.978	4.02	4.2	52.6
151	10/10/2015	09:20:43	-97.931	36.719	5.63	4.6	139.9
161	11/20/2015	22:40:40	-97.828	36.948	5	4.3	102.1
164	11/23/2015	21:17:47	-98.276	36.838	5.03	4.6	39.9
166	11/30/2015	09:49:13	-98.056	36.751	5.63	4.8	173.4
171	1/1/2016	11:39:40	-97.406	35.669	5.83	4.3	42.9
172	1/7/2016	04:27:28	-98.741	36.486	7.09	4.6	70.5
173	1/7/2016	04:27:58	-98.725	36.496	4.06	4.6	69.6
182	2/13/2016	17:06:04	-98.72	36.46	4.54	4.6	81.8
183	2/13/2016	17:07:06	-98.726	36.485	8.27	5.1	220.5
185	9/3/2016	12:02:44	-96.931	36.431	4.5	5.8	448.9
186	11/7/2016	01:44:24	-96.803	35.991	4.4	5.0	87.5

Table A3.3: Summary of Oklahoma model coefficients and the anelastic attenuation function γ_{OK} and γ_{CENA} , calibration factor C_{OK} and $C_{e,CENA}$, within event variability η , and in-between event variability ε as determined by the inversion.

f (Hz)	0.19	0.3	0.51	1.01	2	3.3	5.12	10.17	15.26	20.21	50	PGV	PGA
M_h	6.8927	6.7271	6.6563	6.4642	6.2509	5.8482	5.4307	5.4332	5.625	5.3764	5.9006	5.9	5.85
e_0	-0.0689	0.4494	1.2828	2.0102	2.5469	2.6187	2.5414	2.7636	2.889	2.5728	2.3793	5.9604	2.2156
e_1	1.9793	1.9171	1.7362	1.3242	0.8848	0.8513	0.818	0.7155	0.7003	0.7181	0.6997	1.03	0.6859
e_2	-0.061	-0.084	-0.134	-0.2472	-0.3483	-0.3634	-0.3859	-0.2604	-0.1696	-0.1604	-0.1067	-0.1651	-0.1393
e_3	1.5919	1.4521	1.1836	0.9798	0.9178	0.8798	0.8423	0.7935	0.7602	0.7536	0.7489	1.0789	0.7656
b_3	-0.5823	-0.5278	-0.4321	-0.2957	-0.2078	-0.2146	-0.2908	-0.3807	-0.4634	-0.5115	-0.6376	-0.5785	-0.6187
b_4	0.0793	0.0702	0.053	0.0273	0.0085	0.0059	0.0143	0.0252	0.0361	0.043	0.0625	0.0574	0.0603
s_0	-6.1625	-7.6498	-6.5491	1.116	3.9137	-0.2401	-2.8318	-4.0209	-2.3368	-0.9678	-1.1697	-2.2458	-2.1315
s_1	4.8839	6.3092	5.697	-0.5002	-3.2548	-0.1858	1.8381	3.0878	2.0173	0.9945	1.2816	1.9508	1.937
s_2	-1.3179	-1.8048	-1.7236	0.0514	0.9791	0.1799	-0.3622	-0.761	-0.5053	-0.2209	-0.3364	-0.5181	-0.504
s_3	0.149	0.2188	0.2222	0.0085	-0.1185	-0.0293	0.0321	0.0833	0.0563	0.0217	0.0394	0.0614	0.0582
s_4	-0.0059	-0.0095	-0.0102	-0.001	0.0051	0.0014	-0.0011	-0.0034	-0.0023	-0.0008	-0.0017	-0.0027	-0.0025
s_5	-1.2368	-3.5814	-6.0007	-4.3861	0.8735	2.1854	0.7143	-2.5045	-3.8552	-4.1732	-1.2719	-1.7584	-1.4442
s_6	0.7939	2.7948	4.984	3.9802	-0.4705	-1.9496	-1.0055	1.6147	2.8013	3.2534	1.2532	1.3793	1.2353
s_7	-0.1084	-0.7224	-1.4353	-1.2537	0.0707	0.6164	0.4204	-0.3024	-0.6513	-0.8208	-0.3167	-0.3256	-0.2851
s_8	-0.0028	0.0771	0.1753	0.1685	0.0044	-0.075	-0.0591	0.0246	0.0673	0.0917	0.0362	0.035	0.0302
s_9	0.0009	-0.0028	-0.0076	-0.008	-0.0008	0.0032	0.0028	-0.0007	-0.0026	-0.0038	-0.0015	-0.0014	-0.0012
γ_{CENA}	-0.0009	-0.0011	-0.001	-0.0013	-0.002	-0.0032	-0.0043	-0.0057	-0.0057	-0.0055	-0.0047	-0.0047	-0.0028
$C_{e,CENA}$	0.0783	-0.0325	-0.3011	-0.3734	-0.3654	-0.233	-0.1027	-0.1737	-0.2819	-0.4892	-0.1823	-0.0196	-0.21
γ_{OK}	-0.0017	-0.0022	-0.0021	-0.0020	-0.0017	-0.0018	-0.0018	-0.0031	-0.0044	-0.0026	-0.0010	-0.0026	-0.0017
C_{ok} (ln units)	0.4537	0.6724	0.2519	0.2959	-0.2234	-0.2809	-0.4081	0.0813	0.1704	-0.0273	0.1191	0.0733	0.4537
η (ln units)	0.4948	0.4972	0.4908	0.4931	0.5309	0.5089	0.4936	0.4412	0.4096	0.4394	0.5278	0.5090	0.4948
ε (ln units)	0.4676	0.4787	0.4271	0.3786	0.4118	0.4430	0.4457	0.4547	0.4114	0.4131	0.4300	0.4226	0.4676

Table A4.1: Tabulation of Magnitude Estimation Model Parameters. MC_F is the magnitude calibration factor for each frequency. $\gamma_{F, low}$ (Eastern), $\gamma_{F, mod}$ (moderate), and $\gamma_{F, high}$ (Western) are the anelastic attenuation coefficients.

	3.33 Hz	1.00 Hz
MC_F	-3.3	-4.5
$\gamma_{F, low}$	0.0015	0.0007
$\gamma_{F, mod}$	0.0033	0.0021
$\gamma_{F, high}$	0.0050	0.0035

Table A4.2: Summary of Alberta model coefficients, the anelastic attenuation function γ_{AB} , calibration factor C_{AB} , within event variability η , and in-between event variability ϵ as determined by the inversion.

f (Hz)	0.19	0.3	0.51	1.01	2	3.3	5.12	10.17	15.26	20.21	50	PGV	PGA
Mh	6.8927	6.7271	6.6563	6.4642	6.2509	5.8482	5.4307	5.4332	5.625	5.3764	5.9006	5.9	5.85
e0	-0.0689	0.4494	1.2828	2.0102	2.5469	2.6187	2.5414	2.7636	2.889	2.5728	2.3793	5.9604	2.2156
e1	1.9793	1.9171	1.7362	1.3242	0.8848	0.8513	0.818	0.7155	0.7003	0.7181	0.6997	1.03	0.6859
e2	-0.061	-0.084	-0.134	-0.2472	-0.3483	-0.3634	-0.3859	-0.2604	-0.1696	-0.1604	-0.1067	-0.1651	-0.1393
e3	1.5919	1.4521	1.1836	0.9798	0.9178	0.8798	0.8423	0.7935	0.7602	0.7536	0.7489	1.0789	0.7656
b3	-0.5823	-0.5278	-0.4321	-0.2957	-0.2078	-0.2146	-0.2908	-0.3807	-0.4634	-0.5115	-0.6376	-0.5785	-0.6187
b4	0.0793	0.0702	0.053	0.0273	0.0085	0.0059	0.0143	0.0252	0.0361	0.043	0.0625	0.0574	0.0603
s0	-6.1625	-7.6498	-6.5491	1.116	3.9137	-0.2401	-2.8318	-4.0209	-2.3368	-0.9678	-1.1697	-2.2458	-2.1315
s1	4.8839	6.3092	5.697	-0.5002	-3.2548	-0.1858	1.8381	3.0878	2.0173	0.9945	1.2816	1.9508	1.937
s2	-1.3179	-1.8048	-1.7236	0.0514	0.9791	0.1799	-0.3622	-0.761	-0.5053	-0.2209	-0.3364	-0.5181	-0.504
s3	0.149	0.2188	0.2222	0.0085	-0.1185	-0.0293	0.0321	0.0833	0.0563	0.0217	0.0394	0.0614	0.0582
s4	-0.0059	-0.0095	-0.0102	-0.001	0.0051	0.0014	-0.0011	-0.0034	-0.0023	-0.0008	-0.0017	-0.0027	-0.0025
s5	-1.2368	-3.5814	-6.0007	-4.3861	0.8735	2.1854	0.7143	-2.5045	-3.8552	-4.1732	-1.2719	-1.7584	-1.4442
s6	0.7939	2.7948	4.984	3.9802	-0.4705	-1.9496	-1.0055	1.6147	2.8013	3.2534	1.2532	1.3793	1.2353
s7	-0.1084	-0.7224	-1.4353	-1.2537	0.0707	0.6164	0.4204	-0.3024	-0.6513	-0.8208	-0.3167	-0.3256	-0.2851
s8	-0.0028	0.0771	0.1753	0.1685	0.0044	-0.075	-0.0591	0.0246	0.0673	0.0917	0.0362	0.035	0.0302
s9	0.0009	-0.0028	-0.0076	-0.008	-0.0008	0.0032	0.0028	-0.0007	-0.0026	-0.0038	-0.0015	-0.0014	-0.0012
γ_{CENA}	-0.0009	-0.0011	-0.001	-0.0013	-0.002	-0.0032	-0.0043	-0.0057	-0.0057	-0.0055	-0.0047	-0.0047	-0.0028
Ce, CENA	0.0783	-0.0325	-0.3011	-0.3734	-0.3654	-0.233	-0.1027	-0.1737	-0.2819	-0.4892	-0.1823	-0.0196	-0.21
γ_{AB}	-5.03E-04	-2.29E-03	-2.86E-03	-2.46E-03	-2.58E-03	-3.43E-03	-4.16E-03	-5.07E-03	-5.59E-03	-5.24E-03	-4.10E-03	-3.04E-03	-4.21E-03
C_{AB} (ln units)	0.54	0.24	-0.20	-0.37	-0.62	-0.65	-0.45	-0.48	-0.52	-0.51	-0.29	-0.39	-0.36
C_{AB} model(ln units)	0.00	0.00	-0.16	-0.36	-0.50	-0.50	-0.50	-0.50	-0.50	-0.50	-0.50	-0.39	-0.36
η (ln units)	0.495	0.497	0.491	0.493	0.531	0.509	0.494	0.441	0.411	0.410	0.439	0.528	0.509
ϵ (ln units)	0.468	0.479	0.427	0.379	0.412	0.443	0.446	0.455	0.425	0.411	0.413	0.430	0.423

Table A4.3: Table of stress parameter values from inversion for all events in Alberta.

Event ID	YYYY-MM-DD	hh:mm:ss	Latitude	Longitude	Depth (km)	Moment Magnitude, M_{NA18}	Stress Parameter, $\Delta\sigma$ (bar)
1	2013-12-01	15:09:29	54.45	-117.40	0.0	3.2	105.8
2	2013-12-03	06:27:56	54.50	-117.40	1.7	3.0	131.3
3	2013-12-04	03:13:20	54.47	-117.44	0.9	3.0	44.9
4	2014-01-25	03:59:45	54.51	-117.21	0.1	3.2	14.5
5	2014-02-13	14:36:42	51.82	-116.88	0.1	3.2	91.5
6	2014-05-14	09:46:11	54.51	-117.34	0.2	3.2	52.9
7	2014-08-09	15:28:51	52.21	-115.22	8.3	4.1	34.9
8	2015-01-07	04:50:47	54.43	-117.30	12.9	3.2	50.7
9	2015-01-07	05:28:46	54.43	-117.30	12.1	3.1	82.0
10	2015-01-14	16:06:25	54.37	-117.35	6.6	3.7	24.2
11	2015-01-15	19:18:29	54.38	-117.46	1.6	3.4	63.4
12	2015-01-23	06:49:20	54.43	-117.31	2.1	3.8	79.9
13	2015-02-10	07:39:42	54.37	-117.22	3.5	3.0	46.3
14	2015-06-02	14:34:51	52.45	-114.99	0.2	3.5	16.8
15	2015-06-13	23:57:54	54.15	-116.86	14.2	4.1	56.6
16	2015-08-19	00:02:45	54.48	-117.26	16.5	3.1	127.0
17	2015-08-22	04:46:11	54.45	-117.23	10.3	3.0	93.1
18	2015-09-04	13:23:24	54.46	-117.24	8.5	3.1	129.1
19	2016-01-12	18:27:23	54.41	-117.29	1.0	4.3	137.1
20	2016-04-23	11:03:41	54.42	-117.29	9.7	3.0	92.6
21	2016-08-16	06:30:56	56.34	-117.21	0.0	3.3	52.1
22	2016-11-25	05:31:25	54.36	-117.24	7.0	3.4	77.1
23	2016-11-25	21:24:01	54.35	-117.24	3.2	3.3	57.7
24	2016-11-29	10:15:25	54.34	-117.26	1.8	3.4	39.6
25	2016-12-05	14:27:24	54.34	-117.24	2.3	3.3	24.6
26	2016-12-06	01:05:06	54.35	-117.24	3.5	3.2	39.2
27	2016-12-07	10:11:38	54.33	-117.25	1.4	3.3	30.8
28	2017-02-24	09:22:44	52.76	-119.02	0.1	3.3	26.5
29	2017-06-25	22:56:33	54.42	-117.42	3.4	3.3	14.3
30	2017-06-28	19:00:51	54.42	-117.43	6.4	3.2	29.6
31	2017-08-03	00:57:30	54.43	-117.42	6.5	3.2	30.0
32	2017-12-05	00:01:22	54.23	-116.63	3.5	3.1	177.8
33	2017-12-07	00:28:29	54.24	-116.64	5.0	3.1	200.6
34	2017-12-16	00:29:07	54.24	-116.64	3.0	3.4	127.8
35	2018-03-09	00:48:08	52.22	-113.96	3.7	3.0	55.8
36	2018-06-27	00:23:20	54.36	-117.72	7.0	3.2	52.0
37	2018-07-11	00:38:18	54.33	-117.62	7.0	3.2	207.1

Curriculum Vitae

Name: Mark Novakovic

Post-secondary Education and Degrees: The University of Western Ontario
London, Ontario, Canada
2014-present Ph.D. Engineering Seismology

University of Alberta
Edmonton, Alberta, Canada
2008-2013 B.Sc. with Specialization Geophysics

Honors and Awards: Queen Elizabeth II Graduate Scholarship in Science and Technology
2016-2017

Western University Earth science Travel Grant
2015, 2017

Western Graduate Research Scholarship
2014-2018

University of Alberta Academic Excellence Scholarship
2009

Related Work Experience Post-Doctoral Engineering Seismologist
Nanometrics
2018 -- Present

Teaching Assistant
The University of Western Ontario
2014 – 2017

Rocky Physics Research Professional
The University of Alberta
2013-2014

Teaching Assistant
The University of Alberta
2013-2014

Publications:

Novakovic M., Atkinson G. M., Assatourians K. (2018). Empirically Calibrated Ground-Motion Prediction Equation for Alberta. Bull. Seismol. Soc. Am. (submitted, in review)

Novakovic M., Atkinson G. M., Assatourians K. (2018). Empirically Calibrated Ground-Motion Prediction Equation for Oklahoma. Bull. Seismol. Soc. Am. DOI: 10.1785/0120170331

Schultz R., Stern V., **Novakovic M.**, Atkinson G. M., Gu Y., (2015). Hydraulic Fracturing and the Crooked Lake Sequences: Insights Gleaned from Regional Seismic Networks. Geophysical Research Letters, DOI: 10.1002/2015GL063455.

Novakovic M., Atkinson G. M. (2015). Preliminary Evaluation of Ground Motions from Earthquakes in Alberta. Seismol. Res. Lett. 86(4), 1086-1095.

Conference Proceedings:

Banff Induced Seismicity Workshop 2018, **Novakovic M.**, Atkinson G. M., Assatourians K., Gu Y., Empirical Ground Motion Characterization of Induced Seismicity in Alberta and Oklahoma.

CGU Niagara Falls 2018, **Novakovic M.**, Atkinson G. M., Assatourians K., Gu Y., Empirical Ground Motion Characterization of Induced Seismicity in Alberta and Oklahoma.

CGU Niagara Falls 2018 Conference **Session Chair** Induced Seismicity in Canada and the USA: Lessons Learned and Recommendations for Partnerships and Potential Directions.

AGU New Orleans 2017 Conference **Oral Session Chair** Seismological Contributions: Earthquake Ground Motions and Engineering Seismology.

AGU New Orleans 2017, **Novakovic M.**, Atkinson G. M., Assatourians K., Empirical Ground Motion Characterization of Induced Seismicity in Alberta and Oklahoma, Poster Presentation.

SSA Denver 2017, **Novakovic M.**, Atkinson G. M., Assatourians K., Empirical Characterization of Source, Site and Attenuation Parameters from Ground Motion Observations for Induced Seismicity in Oklahoma, Poster presentation.

- SSA Reno 2016, Kropivnitskaya Y. Y., Tiampo K., Validation and Calibration of Predictive Relationships between Earthquake Intensity and Tweets Rate for Improving Real-Time Estimation Intensity, **Presenter** SRL issue 87:2B, Pg. 551.
- AGU San Francisco 2015, **Novakovic M.**, Atkinson G. M., Estimation of Source and Attenuation parameters from Ground Motion Observations for Induced Seismicity in Alberta, Poster S43B-2798.
- Geoconvention Induced Seismicity Workshop Calgary 2015, **Novakovic, M.**, Source and Attenuation Parameters for Induced Seismicity in the Crooked Lake Region of Alberta. Oral Presentation.
- Canadian Geophysical Union Joint Assembly, Montreal 2015, **Novakovic M.**, Atkinson G. M., Source and Attenuation Parameters for Induced seismicity in the Crooked Lake Region of Alberta. Oral presentation.
- Canadian Geophysical Union Joint Assembly, Banff 2014, **Novakovic, M.**, Atkinson G. M., Cheadle B., Investigation of Observed Seismicity in the Crooked Lake Region of Alberta. Oral Presentation.